Exploring Remanent Magnetization in Dzyaloshinskii-Moriya Interaction Driven Weak Ferromagnets

A thesis

submitted in partial fulfillment of the requirements of the degree of

DOCTOR OF PHILOSOPHY

by:

NAMRATA PATTANAYAK

Registration ID. 20133281

Department of Physics

INDIAN INSTITUTE OF SCIENCE EDUCATION AND RESEARCH

PUNE - 411008, INDIA

January, 2020

Dedicated

with love & affection

to the most amazing person I know:

Prof. Ashok Das

University of Rochester, USA

Certificate

Certified that the work incorporated in the thesis entitled ***Exploring remanent magnetization in Dzyaloshinskii-Moriya interaction driven weak ferromagnets and piezomagnets***, submitted by NAMRATA PATTANAYAK, was carried out by the candidate under my supervision and direction. I recommend that it may be accepted as fulfilling the dissertation requirement of the Ph. D degree.

Date:
Place: Pune

(Dr. Ashna Bajpai)
Thesis Supervisor

Declaration

I, hereby, declare that the research work presented in the thesis entitled ***"Exploring Remanent Magnetization in Dzyaloshinskii-Moriya Interaction Driven Weak Ferromagnets"*** was carried out by me in the department of Physics, *Indian Institute of Science Education and Research, Pune*, for the degree of ***Doctor of Philosophy***. The thesis contains authentic records of my own work and understanding where others' ideas have also been included. I have adequately cited and referenced the original sources and have not misrepresented or fabricated or falsified any idea/data/fact/source in this thesis. I also declare that any part or whole of this thesis work has not been submitted earlier to this or any other institutions or university for the assessment or for the award of any other academic degree. I understand that violation of the above will be cause for disciplinary action by the Institute and can also evoke penal action from the sources which have thus not been properly cited or from whom proper permission has not been taken when needed.

Date: (Namrata Pattanayak)
Place: Pune ID:20133281

List of Publications

1. **Namrata Pattanayak**, Arpan Bhattacharyya, A. K. Nigam, Sang-Wook Cheong, and Ashna Bajpai, "Quasistatic remanence in Dzyaloshinskii-Moriya interaction driven weak ferromagnets and piezomagnets", ***Phys. Rev. B 96, 104422 (2017)***.
2. **Namrata Pattanayak**, Arpan Bhattacharyya, Shruti Chakravarty and Ashna Bajpai, "Weak ferromagnetism and time-stable remanence in hematite: effect of shape, size and morphology", ***Journal of Physics: Condensed Matter, 31, 365802, (2019)***.
3. **Namrata Pattanayak**, Jitender Kumar, Partha Pratim Patra G. V. Pavan Kumar and Ashna Bajpai, "Dielectric and Raman Spectroscopy in Hematite crystallites across the Morin transition", ***arXiv:1904.07299***.
4. **Namrata Pattanayak**, Sunil Nair and Ashna Bajpai, "Revealing microscopic evidence for the presence of *time-stable* remanence in rhombohedral carbonates", ***Manuscript under preparation***.

List of Oral/Poster presentation

1. **Namrata Pattanayak**, and Ashna Bajpai, "Quasistatic remanence in hexagonal crystallites of α- Fe_2O_3: size effects", ***International Workshop on Advanced Materials (IWAM-2017), Berhampur, India***.
2. **Namrata Pattanayak**, Arpan Bhattacharyya, and Ashna Bajpai, "Ultraslow magnetization relaxation in rhombohedral structured weak ferromagnets and piezomagnets", ***9th Joint European Magnetic Symposia (JEMS-2018), Mainz, Germany***.
3. **Namrata Pattanayak** and Ashna Bajpai,"Quasistatic remanence in rhombohedral weak ferromagnets and piezomagnets", ***International Conference on Magnetic Materials and Application (ICMAGMA-2018), NISER, India***.

Acknowledgments

First and foremost, it is a pleasure for me to express my deepest gratitude to my supervisor, Dr. Ashna Bajpai for her constant guidance and encouragement throughout the course of my Ph.D journey. My research work would have been a lot more difficult without her help and academic support.

I would like to extend my sincere thanks to the research advisory committee (RAC) members, Dr. Sunil Nair and Dr. Mukul Kabir for their insightful comments and suggestions. I am specially thankful to Dr. Mukul Kabir for teaching me condensed matter physics. I am also thankful to Dr. Surjeet singh for his insightful discussions and motivation at times when needed.

I would like to acknowledge Dr. Sunil Nair, Shruti Chakravarty, Charu Garg, Soumendra Nath Panja and Prof. Arun K. Nigam, TIFR, for the magnetization measurements. I am thankful to Dr. Pavan Kumar and Dr. Partha Pratim Patra for the Raman spectroscopy measurement. I am also thankful to Dr. Surjeet Singh and Prachi Telang for the specific heat measurement. Many thanks to Arpan Bhattacharyaa and Gouranga Manna for their help in synchrotron XRD measurements at KEK, Japan.

I would also like to acknowledge the Infosys foundation and Department of Physics, IISER, Pune for supporting my travels towards attending the international conferences.

I am grateful to our technical staff members Nilesh Dumbre, Anil Prathamshetti, Parveen Nasa, Prashant Kale, Sudhir Lone, Yathis T Shakarappa and Santosh Khilare for their technical assistance in various stages during the Ph.D. work. Mny thanks to all the administrative staff members and specially Prabhakar, Kalpesh, Dhanashree, Tushar, Nayana, Sayalee, Priyadarshini and Prabhas for their support in administrative matters.

I am also thankful to the security, librarian, electrician and the housekeeping staff for their help throughout my stay at IISER, Pune.

My heartfelt gratitude to Prof. Swapan Pati, my uncle, for his blessings, support, motivation and encouragement.

I would like to thank my Lab mates Aakanksha, Nitesh and Bharat for their suggestions and help at times needed. The CCD time with Aakanksha has always been mind relaxing. I am also thankful to all my well wishers, all my friends specially Gunjan, Rabindranath, Chetan, Avirup and the members of the Physics department $\hbar$, IISER, Pune.

I will never forget the tea time with Dr. Jitender and Dr. Shruti in my life. Dr. Shruti is more like my elder sister and friend and I will always appreciate her presence in all my good and bad times. I am in short of adjectives to thank Dhananjay, my special friend, for his support in all bad times. Special thanks to Dr. Padmalochan Panda for all his support during the Ph.D. days.

I am thankful to Almighty God, my beloved parents and my brother Jinu for their encouragement, unconditional love and blessings to overcome many barriers to reach the milestone of Doctor of Philosophy.

No thanks can be enough to acknowledge the endless encouragement, care and support I have from the person whom I admire the most, Prof. Ashok Das. Without him it would have been impossible for me to reach this stage.

Thank you all for your love, patience and support to make the journey a little easier.

Synopsis

The phenomenon of weak ferromagnetism, observed in some otherwise antiferromagnets (AFMs) such as in α-Fe_2O_3, $MnCO_3$, $CoCO_3$, is associated with a spin canting mechanism related to the well-known Dzyaloshinskii-Moriya Interaction (DMI). The weak ferromagnetism in some of these AFMs is also concurrent with another functionality, namely, piezomagnetism, a magnetic counter part of the piezoelectric effect. However, unlike weak ferromagnetism, the phenomenon of piezomagnetism is a relatively less explored phenomenon. This thesis presents remanent magnetization measurements using SQUID magnetometry in some of the classic DMI driven weak ferromagnets (WFMs)/piezomagnets (PzMs) including α-Fe_2O_3, $MnCO_3$, $CoCO_3$ and $NiCO_3$. In addition to this, remanence in ultra small nano particles of $FeCO_3$, a compound which is not a symmetry allowed WFM, has also been investigated. A core finding of the present thesis is that all the classic DMI driven compounds exhibit two distinct time scales in the magnetization relaxation measurements, one of which is short and, therefore, leads to a quick decay while the other is ultraslow leading to observation of a *time-stable* remanence, which can also be termed as *quasi-static* remanence. The *time-stable* part of the remanence also varies with the strength of the magnetic field in a counter intuitive way. These unique features of remanence are consistently observed in DMI driven WFMs, irrespective of shape, size and morphology. Our study also includes a single crystal of α-Fe_2O_3. We have divided the entire thesis into 7 chapters and 2 appendices.

Chapter 1 gives a brief introduction to various models of exchange interactions which gives rise to different types of long range magnetic ordering such as ferromagnetism, antiferromagnetism. The phenomenon of weak ferromagnetism, as observed in some otherwise AFMs, symmetry requirements associated with Dzyaloshinskii Moriya Interaction as well as the phenomenon of piezomagnetism are introduced in this chapter. Remanent magnetization and its importance in identifying and exploring complex magnetic phases such as spin glasses and superparamagnets, which are known to exhibit slow magnetization relaxation phenomenon, is highlighted. The motivation and the objective behind experimental investigation of remanent magnetization in symmetry allowed weak ferromagnets and piezomagnets is outlined towards the end of chapter 1.

Chapter 2 includes the details of sample synthesis and various techniques employed to characterize the samples. We have synthesized $MnCO_3$, $NiCO_3$, $CoCO_3$, $FeCO_3$ and α-Fe_2O_3 in the form of powders consisting of regular shaped crystallites using the hydrothermal technique. Here α-Fe_2O_3 has also been synthesized in five different morphologies by variations in the synthesis parameters of the hydrothermal technique. In this chapter we describe the hydrothermal technique and outline synthesis parameters for each sample. These samples are characterized using techniques such as X-Ray diffraction (XRD), temperature variation of synchrotron XRD along with Rietveld profile refinement and Scanning electron Microscopy (SEM). Neutron diffraction in remanent state has been performed on one representative sample and this technique is briefly described in this chapter. α- Fe_2O_3 in different morphologies has also been explored through dielectric and Raman spectroscopy across the WFM to AFM transition and both these techniques are also discussed in chapter 2.

In chapter 3, we present magnetization and remanent magnetization measurements conducted as a function of temperature in different magnetic fields in $MnCO_3$, $NiCO_3$, $CoCO_3$ and $FeCO_3$. Out of these four carbonates, the first three are symmetry allowed WFMs. These data bring out the counter-intuitive magnetic field dependence of remanence. In addition, an ultra-slow magnetization relaxation phenomenon is observed in all these carbonates, which reveals *quasi-static* nature of the remanence. The presence of these unique features of remanence appear to be connected to the DMI driven spin canting phenomenon. This chapter also presents our study of the remanent magnetization in another member of this family, $FeCO_3$, which is not a symmetry allowed WFM but reported to be a PzM. Remanence measurement in this compound is certainly interesting in particular with nanoscaling.

Chapter 4 includes remanent magnetization investigation in α-Fe_2O_3 which has a low temperature pure AFM phase and room temperature WFM phase. Considering the room temperature weak ferromagnetic property, remanent magnetization is explored in α-Fe_2O_3 with special interest to nanoscaling. Corroborated by synchrotron measurements, the study provides crucial insights to optimize the magnitude of *time-stable* remanence in α-Fe_2O_3. In establishing the generality of the unique features of remanence, the chapter also discusses remanent magnetization study on a single crystal of α-Fe_2O_3.

Chapter 5 includes the scaling behaviour of remanent magnetization in $MnCO_3$, $CoCO_3$, $NiCO_3$. Qualitative and quantitative comparison of the observed *time-stable* remanences in these symmetry allowed WFM, in conjuncture with their Néel temperature is put forward. In this chapter we present a plausible mechanism behind the observation of ultra-slow magnetization dynamics in these canted systems. Finally this chapter concludes with a microscopic evidence for ultra-slow relaxation/*time-stable* remanence in one representative WFM sample. This is achieved by performing a neutron diffraction (ND) study in the presence of magnetic field, followed by ND in remanent state in $CoCO_3$.

In chapter 6 we have explored the AFM to WFM transition in α-Fe_2O_3 through dielectric and Raman spectroscopy. These studies performed on various shapes, sizes and morphologies bring out the presence of spin phonon coupling reflected as the anomaly in the dielectric constant around the AFM to WFM transition in α-Fe_2O_3.

Chapter 7 gives the overall conclusion of this thesis and discusses the future scopes and aspects related to this field.

Appendix 1 discusses the derivation of the ground state spin configurations and the direction of the net magnetic moment in α-Fe_2O_3 from the thermodynamic potential of Dzyaloshinskii.

Appendix 2 contains the basic characterization and synthesis details of the samples which have not been investigated in the present work, but are interesting from the weak ferromagnetic and piezomagnetic points of view.

Contents

Page

List of Figures

List of Tables

Chapter 1

Introduction

In this work, we have primarily explored remanent magnetization in canted antiferromagnets or weak ferromagnets (WFM), driven by Dzyloshinskii Moriya Interactions. In the following, we discuss the relevant basic concepts related to long range magnetic order such as routine FM and AFM and WFM , with special emphasis on symmetry consideration involved in DMI driven WFM. We also discuss the relevance of remanent magnetization measurements in identifying magnetic ordering in complex magnetic systems such as spin glass etc.

1.1 Exchange interactions and Magnetism

The basic element in the study of magnetism is the magnetic dipole moment associated with the spin and the orbital motion of an electron in an atom. As we know, an electron has a spin angular momentum in addition to its orbital angular momentum which are quantum mechanical in nature. Classically, one may try to visualize the spin and the orbital angular momentum of the electron as if it is rotating around the nucleus in an orbit similar to the motion of a planet in an orbit around the sun. This orbital motion of the electron gives rise to the orbital magnetic dipole moment μ_{orb}. On top of that, the electron may be thought of as spinning around its own axis, similar to the rotation of the earth around its axis, which gives rise to the spin magnetic dipole moment μ_{spin}.

This is shown pictorially in Fig. 6.1. Each atom acts like a tiny magnet due to the vector sum of the μ_{orb} and μ_{spin} of electrons constituting the atom. A solid is a collection of a large number of such tiny magnets which interact in different ways to give rise to exotic magnetic properties in a material.

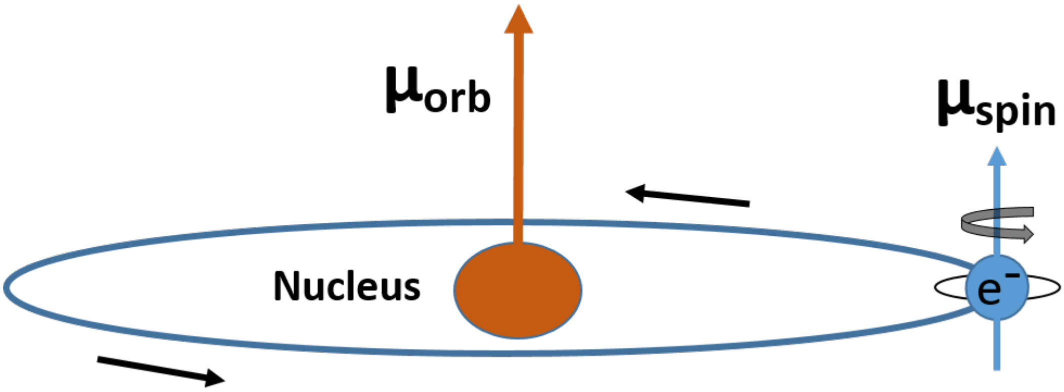

Figure 1.1 – Schematic illustration of the spin and orbital angular momentum of an electron rotating around the nucleus.

While discussing magnetism in solids one has to deal with the quantum mechanical exchange interaction which is at the heart of all long range magnetic ordering. The spin-orbit coupling allows the spin of an electron to talk to the orbitals or the lattice. The lock-in mechanism of the spins with the lattice is the very basis of the origin of easy and hard axis, the so called magnetocrystalline anisotropy. Finally the response of a magnetic moment to the external magnetic field, namely, the Zeeman interaction plays a fundamental role in aligning the magnetic moments in a magnetic material. In particular, to align a magnetic material from the easy direction to the hard direction the Zeeman interaction has to compete with the spin-orbit coupling which determines the magnetocrystalline anisotropy. The interplay between the exchange interaction, spin-orbit coupling and the Zeeman interaction forms the basis of magnetism research. In the following, we will discuss different models of exchange interactions through which magnetic moments in a solid talk to each other and produce long range magnetic ordering.

1.1.1 Heisenberg exchange interactions

The concept of a quantum mechanical exchange force between two electrons was first introduced in 1926 by Werner Heisenberg [1, 2]. The exchange interaction between two neighbouring spins S_i and S_j of the atoms i and j can be defined by the well known Heisenberg Hamiltonian as:

$$H_{ex} = -\sum_{ij} J_{ij}\ S_i.S_j, \tag{1.1}$$

where $J_{ij} = J_{ji}$ is the symmetric exchange integral between the ith and jth spins, the sign of which represents the type of magnetic interaction. For instance, when J_{ij} is positive, the exchange energy, H_{ex}, is minimum when two spins are parallel. This gives rise to ferromagnetic ordering or ferromagnetism(↑↑). On the other hand, when J_{ij} is negative, H_{ex} is minimum when both spins are antiparallel. This gives rise to antiferromagnetism (↑↓).

The exchange integral J_{ij} is basically related to the orbital overlapping between the atoms and hence falls off rapidly with the increase of distance between two magnetic spins S_i and S_j situated at the i^{th} and j^{th} sites [3]. The quantum mechanical exchange interaction is, therefore, short range. However, it is responsible for all long range magnetic ordering.

The Heisenberg exchange interaction deals with interatomic exchange through the direct overlap of neighbouring orbitals. However cases where direct orbital overlapping is insufficient, such as in rare-earth elements or in transition metal oxides and flourides an indirect exchnage interaction is known to explain long range magnetic ordering in these systems [4, 5]. These mechanisms are briefly discussed in the next section.

1.1.2 Super exchange interactions

The magnetism in some ionic solids, such as MnO, MnF_2, is largely governed by the super exchange interaction [6, 7]. Magnetic cations in such compounds are always separated by a non-magnetic anions. The Heisenberg exchange interaction then proceeds through the hopping of electrons from one magnetic cation to the next magnetic cation through the intermediary anion. Therefore, the interaction is indirect and is also known as semicovalent exchange according to Goodenough. The magnetic ground state is determined by the balance of energy associated with the hopping of same spin electron between different atomic sites (-t) and onsite Coulomb repulsion energy (U) of electrons with opposite spins when present at the same site. The hopping energy favours delocalization of electrons through which the electrons save their kinetic energy. This delocalization or hopping of electrons is only allowed when two magnetic cation sites have opposite spins thereby leading to antiferromagnetism. However, whether a superexchange interaction will lead to an antiferromagnetic or a ferromagnetic ground state is determined by a set of rules formulated by Goodenough and Kamarori [8, 9]. In a simplistic way, the exchange interaction is strong and antiferromagnetic when the angle between cation-anion-cation orbital overlapping lies close to 180°. The interaction is weak and leads to ferromagnetism when the angle is close to 90°. Schematics of the typical AFM superexchange and FM superexchange paths are shown in Fig. 1.2.

1.1.3 Double exchange interaction

Usually most of the magnetic oxides are antiferromagnetic in nature due to the strong super exchange interaction. However, it is also possible to have ferromagnetic oxides when the magnetic cations, involved in the interaction, possess mixed valency. The exchange mechanism, in such oxide compounds, is similar to superexchange, but requires mixed valence cations. The prototypical ferromagnetic oxide is Sr doped LaMnO3 compound in

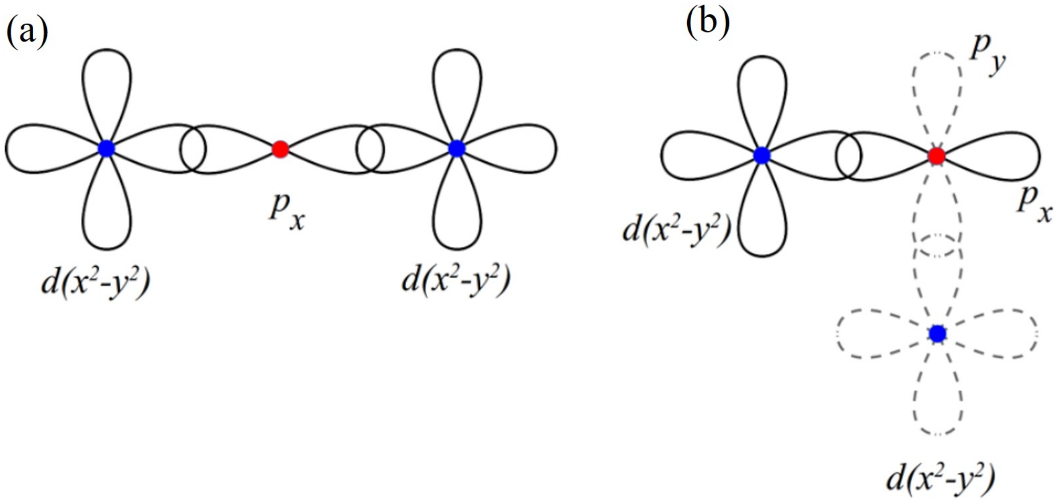

Figure 1.2 – Schematic illustration of (a) AFM, (b) FM superexchange paths

which Mn atom exists both in +3 and +4 oxidation states. The electron hopping between different Mn atoms is allowed only when two neighbouring Mn atoms of different valency align ferromagnetically.

1.1.4 RKKY exchange interaction

In case of metals filled with conduction electrons the exchange interaction is expected to be mediated by the conduction electrons. For example, the exchange interaction between localized 4f moments in rare-earth systems is mediated by the itinerant electrons of 5d and 6s orbitals [10, 11]. In this type of indirect exchange, a spin polarization of conduction electrons or itinerant electrons is caused by a localized moment and these spin polarized conduction electrons interact with a neighbouring localized moment situated at a distance r away. The interaction is popularly known as RKKY interaction after the discoverers Ruderman, Kittel, Kasuya and Yosida. The interaction is also known as itinerant exchange due to the involvement of itinerant electrons as intermediary. The exchange integral in the RKKY interaction takes the form:

$$J_{RKKY}(r) \propto \frac{Cos(2K_F r)}{r^3}. \tag{1.2}$$

The interaction is, therefore, oscillatory and can be ferromagnetic or antiferromagnetic depending on the separation 'r' between the localized moments. The presence of both ferro and antiferro ordering leads to a incommensurate helical magnetic structure often observed in rare-earth elements [5, 12–14].

1.1.5 Complex magnetic ordering

The RKKY interaction is also responsible for the origin of canonical spin glass magnetism observed in some diluted magnetic system such as CuMn [15]. Only a few percent of Mn atoms are present in CuMn and each Mn atom in the compound acts like a localized moment. The interaction between different Mn sites is mediated by the conduction electrons of the Cu atom. The competing ferromagnetic and antiferromagnetic interactions, due to the RKKY interaction between different Mn atoms, leads to frustration in the system. Frustration in the system is responsible for a large number of possible magnetic ground states but there is not a single well defined and preferred ground state among them. At high temperature the magnetic moments usually fluctuate. As the temperature goes down, spin clusters begin to form due to the local magnetic ordering. As the temperature goes further down, at the freezing point T_f of the sample, the correlated clusters get stuck in one of the many possible ground states. Frustration can also arise in systems due to the underlying lattice geometry [16, 17]. Some typical lattice geometries, which lead to complex magnetic ordering, are the triangular lattice geometry or the Kagome lattice geometry as shown in Fig. 1.4 (i, j).

1.1.6 Dzyaloshinskii - Moriya Interaction

Magnetic exchange interactions can also be quite complex and may not always gives rise to ferromagnetic or antiferromagnetic ordering. The spins of some magnetic systems, instead of being collinear (either ferromagnetic or antiferromagnetic), remain canted. The exchange Hamiltonian in such magnetic systems, in addition to the isotropic terms, contains a term which is antisymmetric under the interchange of the two spins. This antisymmetric exchange interaction is popularly known as the Dzyaloshinskii-Moriya interaction (DMI) after the Russian scientist I. E. Dzyaloshinskii and the Japanese scientist Toru Moriya [18, 19]. The interaction Hamiltonian can be written as:

$$H_{DM} = D_{ij}.(S_i \times S_j), \tag{1.3}$$

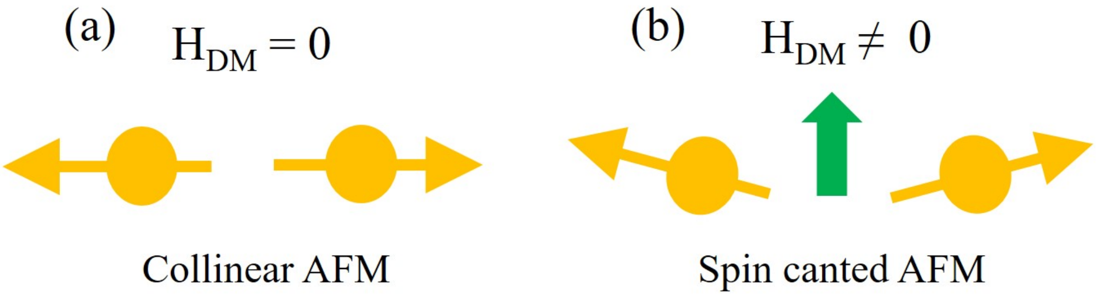

Figure 1.3 – Schematic representation of canted anti ferromagnetic structure as a result of Dzyaloshinskii-Moriya antisymmetric exchange interaction in an otherwise antiferromagnet.

with $D_{ij} = -D_{ji}$. The form of this antisymmetric D-M exchange is such that energy is minimized when the spins S_i and S_j are at right angle to each other in a plane perpendicular to the vector D_{ij}. The interaction, therefore, favours slight canting of the spins and hence forms the basis of all chiral magnetic structures such as skyrmion. However, the conditions under which this interaction can exist in a material are largely determined by the symmetry considerations. For example, let there be a center of inversion between the line joining two spins S_i and S_j. Since the cross product of the spins S_i and S_j changes sign under inversion, the Hamiltonian H_{DM} will only be invariant when $D_{ij} = 0$. Therefore, the DM interaction requires a broken inversion symmetry to exist. Similar set of arguments formulated by Moriya leads to a set of rules that decides the direction of the vector D_{ij} and the direction of canting when present in a system. Without going into details we can conclude that the presence of strong spin-orbit coupling and broken inversion symmetry in a system are the basic requirements for a non vanishing DMI and when such an interaction is present in an antiferromagnetic material, it leads to the phenomenon of weak ferromagnetism [18, 19]. The canted spin structure that leads to weak ferromagnetism in otherwise antiferromagnets is shown schematically in Fig. 1.3. Some prototypical weak ferromagnets where the interaction was first realized are α-Fe_2O_3, $CoCO_3$, $MnCO_3$. A schematic illustration of different types of magnetic ordering are summarized in Fig. 1.4.

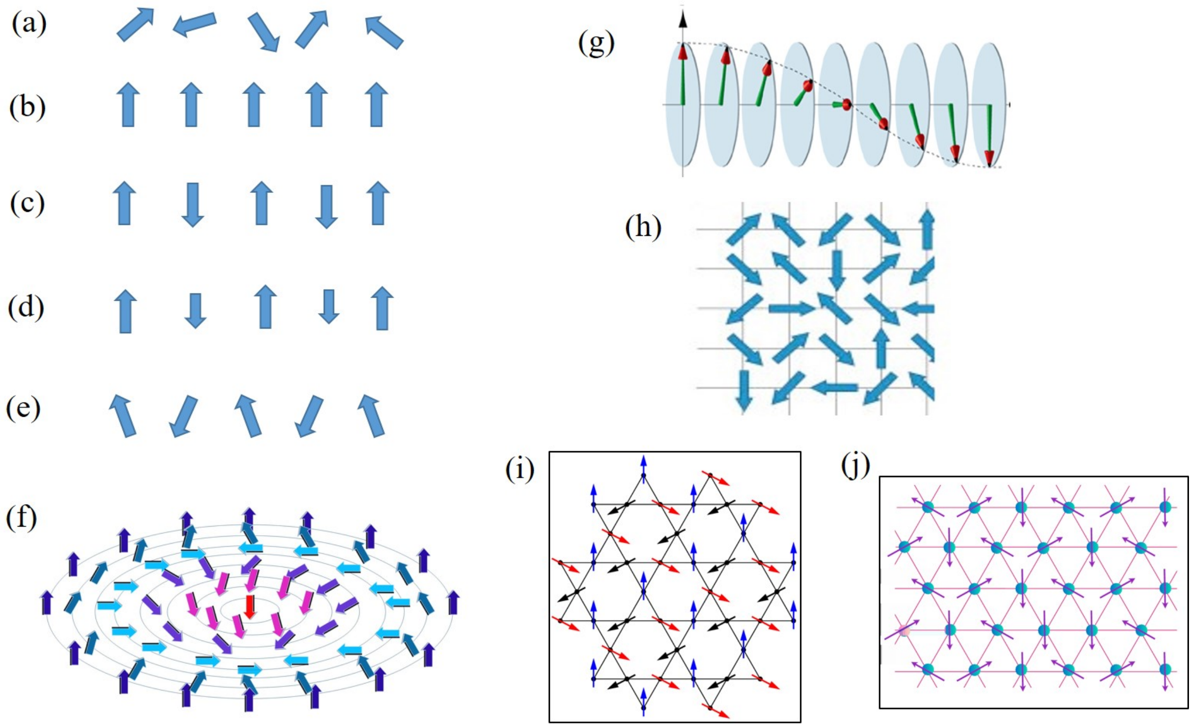

Figure 1.4 – Schematic of various types of magnetic orderings: (a) paramagnetic, (b) ferromagnetic, (c) antiferromagnetic, (d) ferrimagnetic, (e) canted antiferromagnetic. (f) non collinear spin structure in skyrmion, (g) helical magnetic ordering, frustrated spins in (h) spin glass, (i) 2D Kagome lattice , (j) 2D triangular lattice.

1.2 Weak ferromagnetism

The phenomenon of weak ferromagnetism was first observed in the compound α-Fe_2O_3 in 1916 by T. Smith [20]. The small spontaneous magnetic moment in α-Fe_2O_3 at first was thought to originate from the impurity or any inhomogenities present in the system. After 40 years, in 1957, this effect was experimentally observed by Borovik-Romanov and M.P. Orlova in some high quality single crystals of $MnCO_3$ and $CoCO_3$ [21]. To understand this fact, Dzyaloshinskii put forward a phenomenological argument of spin canting mechanism, in the same year, based on group theory and symmetry [18]. After 3 years, Moriya gave a microscopic origin of such spin canting in some magnetic insulators [19] in 1961. The microscopic picture of Moriya combines the usual superexchange interaction due to the hopping of electron between different sites described by the Heisenberg model and the onsite spin-orbit coupling. The spin Hamiltonian of such spin canted system can be expressed as:

$$H = -J_{ij}\ S_i.S_j + D_{ij}.(S_i \times S_j), \tag{1.4}$$

where the first term is the usual isotropic exchange and the second term is the antisymmetric superexchange interaction or Dzyaloshinskii-Moriya Interaction (DMI). As discussed in the previous section the existence of such an antisymmetric exchange interaction is mainly determined by the magnetic symmetry of the system.

To understand this fact we will consider the case of two classic AFMs α-Fe_2O_3 and Cr_2O_3 in more detail. α-Fe_2O_3 exists in two different magnetic states depending on the temperature region of interest. Below the Néel temperature, $T_N \sim 950$ K, α-Fe_2O_3 is a WFM. The weak ferromagnetism persistes upto a temperature of 260 K, below which α-Fe_2O_3 becomes a pure AFM. The temperature at which α-Fe_2O_3 becomes a pure AFM from a WFM is popularly known as Morin transition, T_M. The phenomenon of weak ferromagnetism in the isostructural compound Cr_2O_3 is however absent.

Both α-Fe_2O_3 and Cr_2O_3 possess the same rhombohedral crystal structure. The rhombohedral unit cell contains four magnetic ions which lie along the body diagonal ([111]

axis) of the rhombohedron [18, 19, 22]. The antiferromagnetic spin arrangement in the unit cell below T_N in Cr_2O_3 and in the weak ferromagnetic region, T_N < T < T_M in α-Fe_2O_3 is shown in Fig. 1.5. The spins of Fe atom in the unit cell lie perpendicular to the [111] axis in its WFM phase whereas the spins of Cr atom lie parallel to the [111] axis [4, 23].

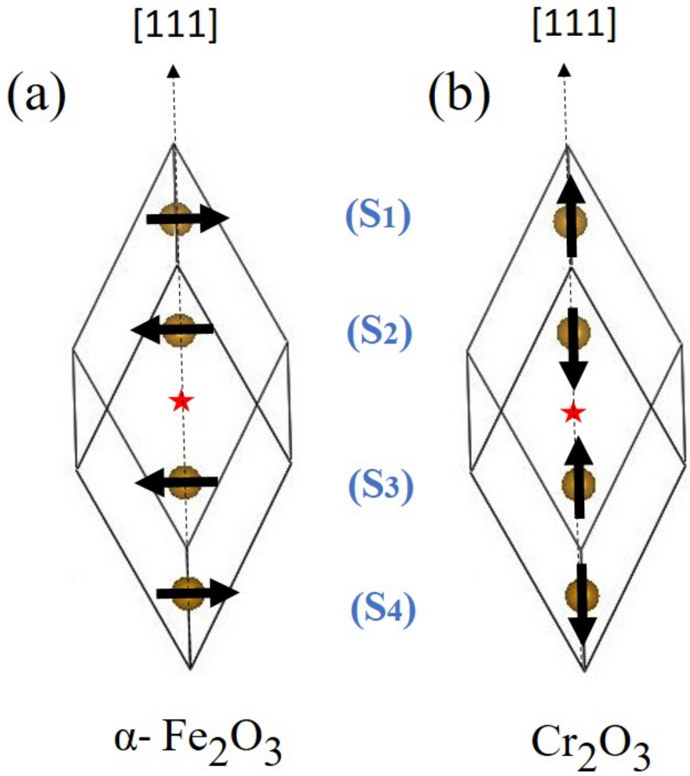

Figure 1.5 – A schematic representation of antiferromagnetic spin configuration below the Néel temperature in α-Fe_2O_3 and Cr_2O_3. Star mark denotes the inversion center and the spins S_1 and S_2 need not be parallel.

Let us impose the symmetry restrictions derived by Moriya [19]. Since there exists a 3 fold symmetry axis along the [111] axis, D vector is parallel to this [111] axis. There is also a center of inversion (denoted by a red star in Fig 1.5) at the mid point of the line joining all four spins. This will lead to the Dzyaloshinskii-Moriya term involving the spins 1 and 4 as well as that involving the spins 2 and 3 to vanish symmetrically. Due to the presence of a glide plane, the DMI coupling between the spins 1 and 2 must be equal and opposite to that between the spins 3 and 4. Similarly, the term connecting the spins 1 and 3 will be equal and opposite to that between the spins 2 and 4 respectively [24]. With these the Dzyaloshinskii-Moriya term for the unit cell can be expressed as (we suppress the indices of D for simplicity):

$$D.((S_1 \times S_2) - (S_3 \times S_4)) + D.((S_1 \times S_3) - (S_2 \times S_4)). \tag{1.5}$$

As can be seen from Fig. 1.5, the spin configuration in Cr_2O_3 is $S_1 \mid\mid S_3$ and $S_2 \mid\mid S_4$ whereas in α-Fe_2O_3, $S_1 \mid\mid S_4$ and $S_2 \mid\mid S_3$. In these two cases, therefore, Eq. (1.5) leads to

$$H_{DM}^{(Cr_2O_3)} \equiv 0, \qquad H_{DM}^{(\alpha Fe_2O_3)} = 4D \cdot (S_1 \times S_2).$$

Thus we see that the DM interaction vanishes identically in Cr_2O_3 because of its particular spin arrangement (independent of any canting between S_1 and S_2) whereas in α-Fe_2O_3 there can exist a finite non vanishing DMI term as long as S_1 is not (anti) parallel to S_2 (namely, when there is canting). In fact we see that α-Fe_2O_3 is a weak ferromagnet below its T_N where the spins are canted. However, when the same α-Fe_2O_3 is cooled there occurs the Morin transition, also known as spin reorientation transition, below which the spins are still antiferromagnetically coupled in the fashion $S_1 \mid\mid S_4$ and $S_2 \mid\mid S_3$ but point along the [111] axis of rhombohedron as shown in Fig. 1.6. This orientation of spins with the [111] crystal axis does not allow DMI to occur as a result α-Fe_2O_3 becomes a pure AFM [18, 24]. Both the AFM and WFM ground state spin configuration and the direction of net moment in the WFM state is discussed in detail in Appendix-1.

Let us again consider the DMI between two neighbouring antiferromagnetic spins S_1 and S_2. The antiferromagnetic vector can be defined as $l = S_1 - S_2$. Similarly, the weakly ferromagnetic vector (or the magnetization vector) can be defined as $m = S_1 + S_2$. With

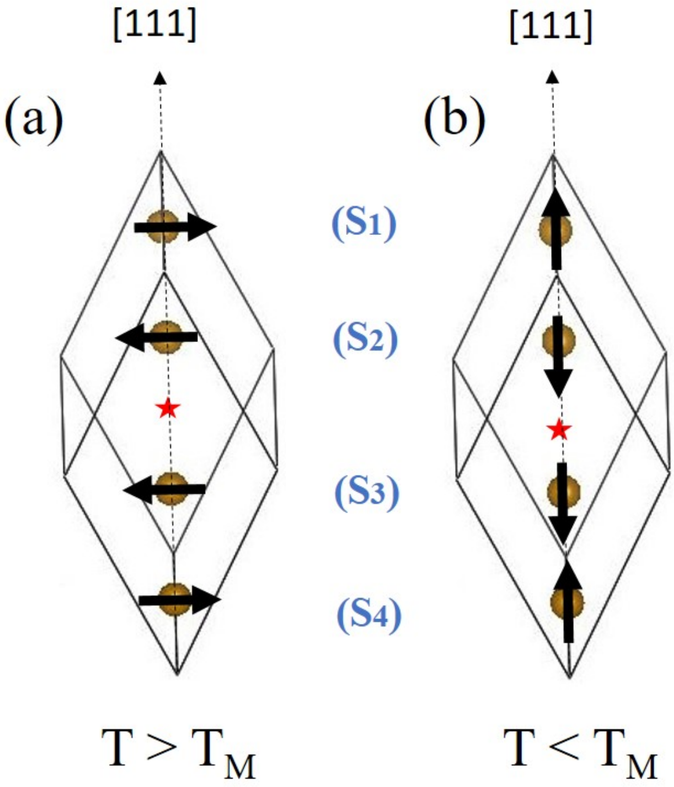

Figure 1.6 – A schematic representation of antiferromagnetic spin configuration below and above the Morin transition in α-Fe_2O_3. The slight canting of the spins above the Morin transition is not shown explicitly here. Star mark denotes the inversion center.

these, the DMI can be rewritten as [25]

$$D.(S_1 \times S_2) = \frac{1}{2}\, D.(l \times m). \tag{1.6}$$

This expression implies that the weak ferromagnetic moment m is always perpendicular to the antiferromagnetic vector l (which can also be seen from their definitions if we assume both the spins to have equal magnitude) [25]. Thus the DMI driven spin canting leads to a transverse weak ferromagnetism. However, there also exists longitudinal weak ferromagnetism with the direction of m parallel to l. The origin of such longitudinal weak ferromagnetism is not DMI, rather it arises when two antiferromagnetic sublattices differ in their magnetic moments. This happens due to the difference in the crystal field environment and SOC around the two magnetic sites. The effect is frequently known as single ion anisotropy (SIA) [19, 26, 27]. It is quite possible to have both types of weak ferromagnetism present in a system. However, the strength of DMI which is first order in SOC will have dominating contribution over the SIA which is second order in SOC [19].

1.3 Piezomagnetism

Piezomagnetism is a magnetic counterpart of piezoelectric effect [27–34]. The phenomenon was first theoretically predicted on symmetry grounds by Dzyaloshinskii for a number of antiferromagnetic compounds such as α-Fe_2O_3, $FeCO_3$, $CoCO_3$, CoF_2, FeF_2. The magnetic symmetry in these compounds is such that it allows the thermodynamic potential of the system to contain a term that is linear in both the stress (σ) and the magnetic field H [35]. Consequently, a magnetization (M_i) which varies linearly with the stress (σ_{jk}) can exist even in the absence of H:

$$M_i = P_{ijk}\, \sigma_{jk}. \tag{1.7}$$

It has been observed that many AFMs which are symmetry allowed weak ferromagnets, also exhibit the phenomenon of piezomagnetism [27–32]. However, unlike weak ferromagnetism, piezomagnetism is a relatively less explored phenomenon. Both the phenomena appear to be closely connected with each other [36]. Experimental observation of this fact was first made by Borovik-Romanov in a number of weak ferromagnets in the form of single crystals [27, 29, 30]. However, whether the phenomenon of piezpmagnetism will always co-exist in all WFMs is still an open question.

1.4 Thermoremanent magnetization

Thermoremanent magnetization (TRM) is a term frequently used in paleomagnetism to study the magnetism of igneous rocks [37, 38]. It is a form of remanent magnetization acquired when a magnetic mineral is cooled in a constant magnetic field H from above a Curie or Néel temperature. The bias field applied while cooling produces a net magnetization in the system. The magnetization relaxation after switching off H, namely, the TRM contains a wealth of information about the system. TRM measurement has proven to be an efficient tool to track the slow relaxation dynamics, for example, in spin glasses (SG), superparamagnets (SPM) and diluted antiferromagnets in a field (DAFF) systems [39–44]. The slow relaxation in these systems is known to follow various functional form such as logarithmic decay, stretched exponential decay or power law decay. The typical relaxation of TRM in some spin glass systems adapted from references [39] and [40] is presented in Fig. 1.7. On the other hand, isothermal remanent magnetization (IRM) is produced when a magnetic field is applied on a sample for a pulse of time (about say 100 sec) at a fixed temperature (isothermal) and then switched off. TRM measurement complimented with IRM (isothermal remanent magnetization) measurement act as finger prints to classify the SG, SPM and DAFF systems. TRM and IRM measurements are also useful in probing the irreversible magnetization dynamics often observed in nanostructured antiferromagnets [45–47]. Unlike TRM measurement where a FC protocol is used to prepare the remanent state, in IRM measurement the system is first zero field cooled (ZFC) to a low temperature. At low temperature, a magnetic field is applied for a finite interval of time and is then removed. The remanent magnetization obtained in this way can be explored as a function of time and temperature. Both the TRM and IRM measurement protocol thereby helps in probing different magnetic states of a magnetic system and when combined act as finger prints to distinguish between various magnetization dynamics. For instance, in the cases of SG and SPM, TRM increases monotonically with H and saturates at higher H. The IRM, on the other hand, increases relatively faster with H compared to the TRM versus H, touches the TRM curve eventually and saturates. The difference between the TRM curves for both the systems is that, in SG systems there appears a cusp in the TRM versus H curve at moderate field values which is absent in the SPM system (as well as in DAFF and AFM nanostructure). This appearance of a cusp in the TRM curve is characteristic to the SG systems. The variation of TRM and IRM with H in DAFF and AFM nano structure are more or less similar. In both the systems TRM increases monotonically with H, follows some power law whereas IRM remains negligibely small. The H dependence of TRM and IRM for a typical SG, SPM, DAFF and AFM nano structure are contrasted in Fig. 1.8.

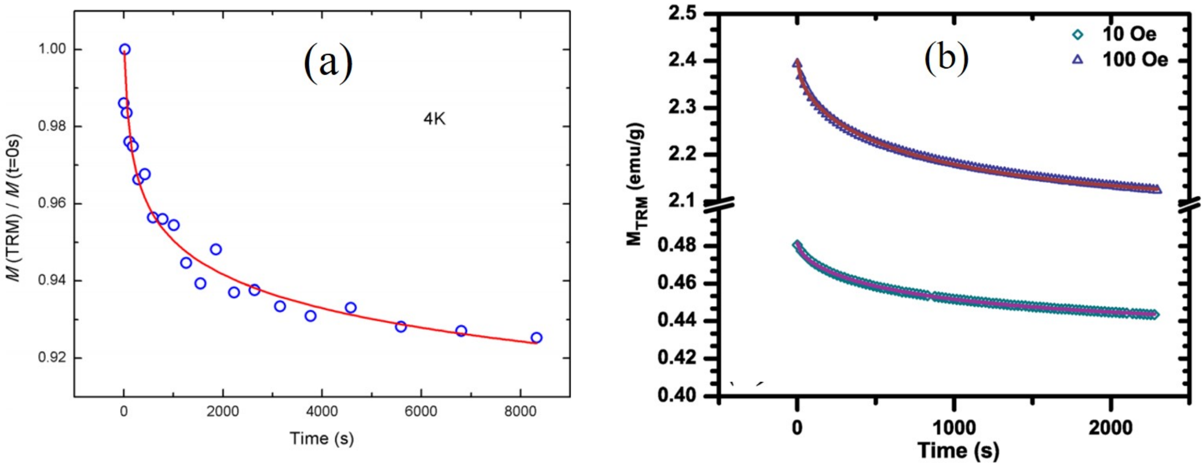

Figure 1.7 – Variation of TRM with time in spin glass systems following (a) power law decay in $Ge_{1-x}Fe_xTe$ epilayer adopted from [39]. (b) stretched exponential decay in Nickel-adsorbed graphene spin glass adopted from [40].

Interestingly, low field TRM measurements performed on some rutile structured WFM/PzM compounds such as FeF_2, MnF_2 or their doped systems has shown an unusually slow relaxation of magnetization dynamic in these systems [48–50]. This was first experimentally observed by J. Kushauer et al in $Fe_{1-x}Zn_xF_2$ system [48]. The unusual slow relaxation of

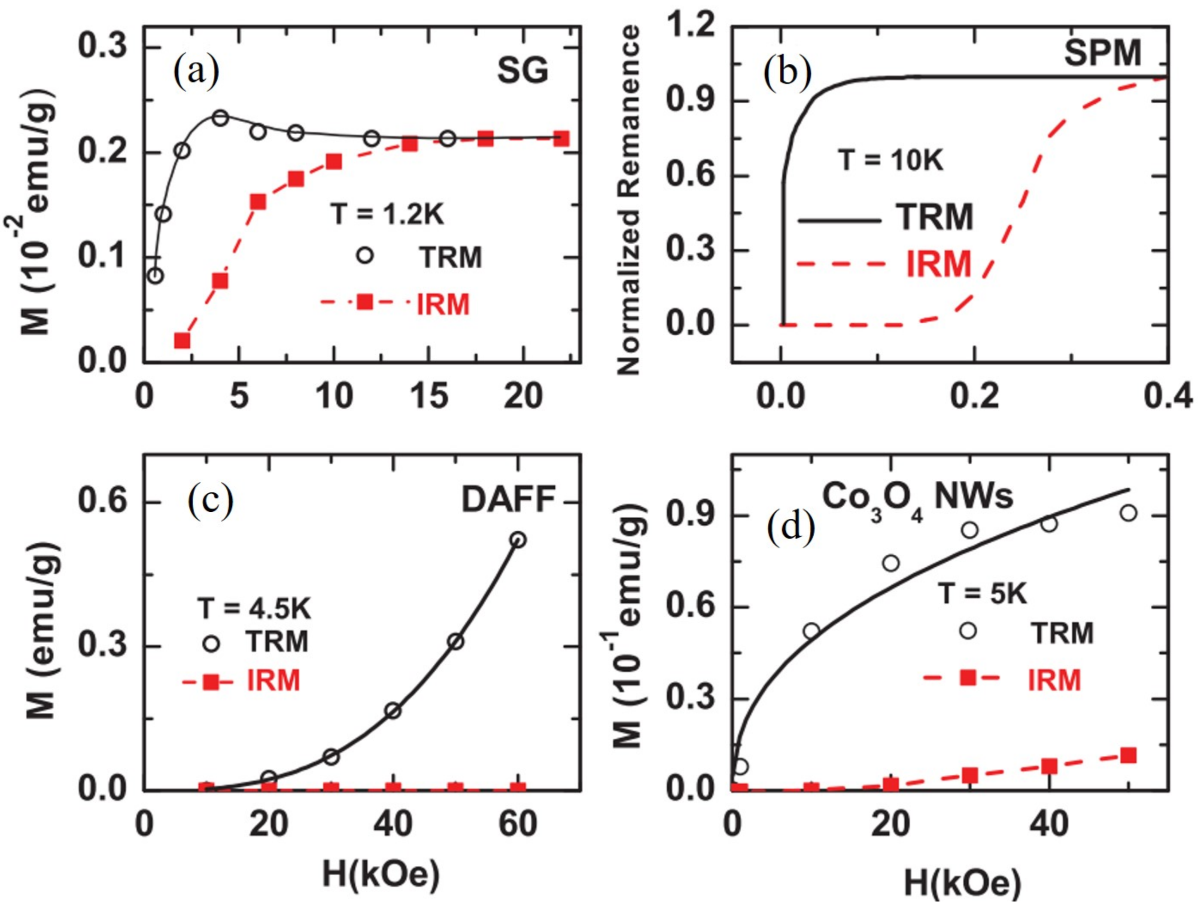

Figure 1.8 – TRM and IRM versus H in a typical (a) AuFe spin glass, (b) superparamagnetic Fe particles, (c) $Fe_{0.48}Zn_{0.52}F_2$ diluted AFM system, (d) Co_3O_4 nano wires adopted from [46].

TRM adopted from the Kushauer's work for $Fe_{1-x}Zn_xF_2$ system is presented in Fig. 1.9. From the main panel of the figure it can, in fact, be noticed that the measured TRM in this system remains almost stable with time up to a time scale of several hours.

1.5 Motivation and objective of the thesis

The unusual slow relaxation of TRM, as observed in some rutile structured flouride systems, has subsequently been observed in different nano scale versions of Cr_2O_3, for example, when Cr_2O_3 is in ultrathin film form grown on top of a Al_2O_3 substrate, or when Cr_2O_3 appears naturally as an insulating layer on top of a CrO_2 grain or when it is encapsulated inside a carbon nanotube [51–53]. In all these systems it has been observed

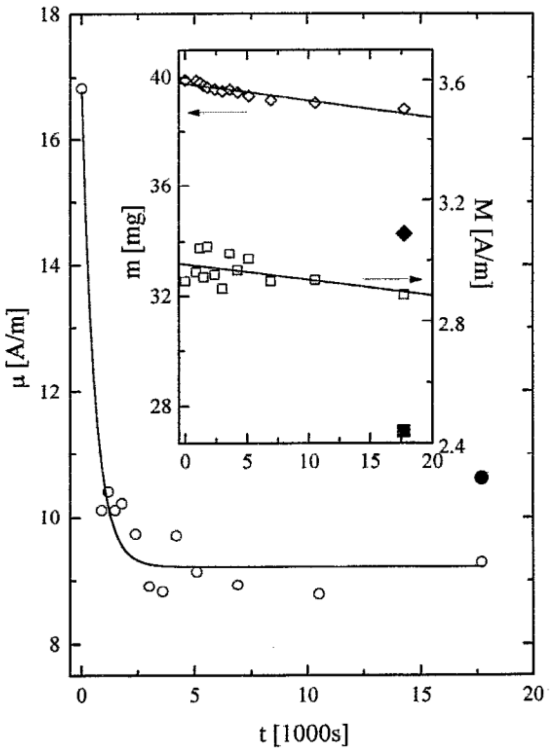

Figure 1.9 – Unusually slow relaxation of remanence in $Fe_{1-x}Zn_xF_2$ system adopted from [48]

that their TRM relaxation is ultraslow in nature. Furthermore, the remanence is seen to vary with the strength of magnetic field in a very counter-intuitive way [52]. These unique features of remanence observed in the Cr_2O_3 systems are presented in Fig. 1.10.

These features of remanence hint that its origin may possibly be related to the randomly built-in stress induced immobile domains whose reversal becomes energetically unfavourable once frozen in the presence of a guiding H. However, a point to ponder here is that, though Cr_2O_3 is isostructural with α-Fe_2O_3, the phenomena of weak ferromagnetism and piezomagnetism are restricted in Cr_2O_3 due to its symmetry [4, 18]. Another surprising feature is that the *quasi-static* remanence is observed only in ultra-thin forms of Cr_2O_3 but not in the bulk counterparts [51–53]. A systematic investigation is, therefore, required to understand whether the observed features of remanence are inherent to the symmetry allowed WFMs/PzMs. It is also important to investigate how these features can come in to existence in systems of tailored symmetry conditions arising due to any

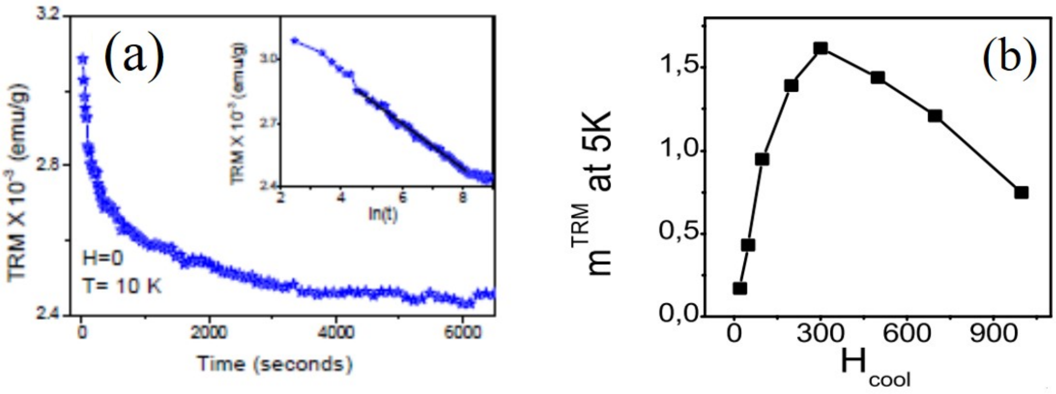

Figure 1.10 – (a) Unusually slow relaxation of TRM in Cr_2O_3 encapsulated inside the carbon nanotude adopted from [53], (b) Counterintuitive dependence of TRM with H in CrO_2/Cr_2O_3 composite adopted from [52]. The TRM increases with the increase of H, attains a maximum value at some particular H and then decreases with the further increase of H.

size and interface related effects as observed in case of Cr_2O_3. Another functionality, which has also been observed, is the scaling behaviour of TRM. It has been observed that the TRM curves obtained at different H during cooling can be gathered into a single master curve when each curve is normalized with its value at a fixed reference temperature T_r less than T_N. This scaling behaviour was first observed in the Zn doped fluoride systems such as in $Fe_{1-x}Zn_xF_2$ and $Mn_{1-x}Zn_xF_2$ systems [49, 50]. Later this behaviour also appeared in the nano structured Cr_2O_3 systems [51, 52]. The scaling behaviour of TRM observed in these systems suggests that its origin may possibly be due to the factorization of piezo moments. A natural question that arises is whether this is particular to some systems or is a general phenomenon likely to arise in other WFM/PzM systems. With these in mind we have worked with some prototypical WFM/PzM compounds. Our primary objective is to explore remanent magnetization in these compounds as a function of temperature and time. The second objective is to explore it in different length scale systems covering bulk single crystal to nano crystallites of various morphologies. This will help in understanding facts that are intrinsic and are associated with the size and morphologies related effects.

Chapter 2

Experimental techniques

2.1 Introduction

This chapter describes various experimental techniques employed for the synthesis and characterization of the samples used in the study. Polycrystalline samples of various shape size and morphologies were synthesized using hydrothermal and precipitation methods. The Phase formation and morphology of the samples were extensively analysed using X-ray diffraction (XRD), scanning electron microscopy (SEM) and energy dispersive X-ray spectroscopy (EDAX) techniques respectively. Magnetic properties of the samples were investigated using a super conducting quantum interference device (SQUID) magnetometer. Neutron diffraction (ND) and synchrotron XRD measurements were carried out for the magnetic and structural analysis respectively. Dielectric spectroscopy, complemented with Raman spectroscopy, was carried out to investigate the electrical properties of the samples. The details of the sample synthesis process and the basic working principles of the techniques employed for sample characterizations are described below.

2.2 Sample synthesis technique

Compare to other known synthesis techniques, the wet chemical synthesis route is the most effective and commonly employed technique for the synthesis of nano particles of various shapes and morphologies [54, 55]. The nano particle formation in the wet chemical synthesis route is a bottom-up approach which takes place in two sequential steps that are nucleation and growth of the nuclei to form nano particles. In the nucleation step the atoms or molecules present in the solution combine to form solid products called as nuclei or seeds. The as prepared seeds play as template for the nano particle growth. Nano particles with controlled shape and size can be synthesized through the precise control of the reaction kinetics/ thermodynamics during the wet chemical synthesis process.

In this thesis work, the samples of α-Fe_2O_3 and MCO_3 (M : Mn, Fe, Co and Ni) were prepared by following two wet chemical synthesis routes that are hydrothermal and chemical precipitation reaction. The materials and reagents used for the synthesis are AR grade purchased from Merck. Deionized distilled water (DDW) have been used through out the synthesis process.

2.2.1 Precipitation reaction

Precipitation reaction occurs when the cations and anions present in an aqueous solution react to form an insoluble solid product called as precipitate [56]. Whether a precipitation reaction will take place is determined by many factors such as the degree of solubility of ionic reactants, reaction temperature, concentration as well as pH of the solution. Once the precipitate forms it can remain suspended through out the solution or can sediment to the bottom of the solution through gravity. The liquid remains above the solid product after sedimentation is called supernatant. The precipitate can finally be separated from the supernatant by various methods mainly through a centrifugal acceleration.

2.2.2 Hydrothermal reaction

Hydrothermal synthesis technique basically involves crystallization of materials in water through the proper control over the thermodynamic variables such as temperature, pressure and reactants [56–58]. The technique is also known as solvothermal when the aqueous medium is other than the water. The synthesis is basically carried out in a Teflon liner that goes inside a sealed reactor, known as high pressure vessel or autoclave. The nano particle formation inside the bomb proceeds through the nucleation and grain growth process. The reaction temperature, pressure, pH and reactant concentration all these parameters affect the nucleation and the growth process and eventually control the crystallinity, shape, size and morphology of the particle [57, 58].

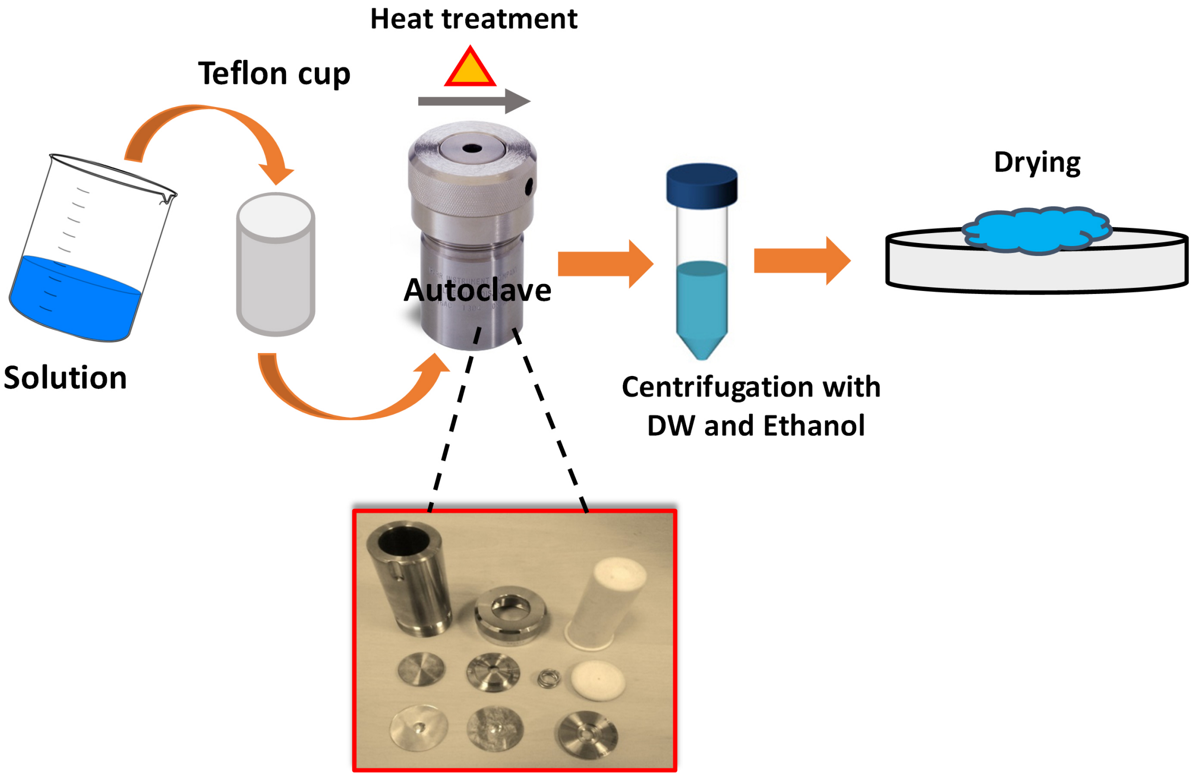

Figure 2.1 – Schematic illustration of hydrothermal synthesis steps followed for the sample preparation.

Crystallites are grown using hydrothermal technique rarely require a post-calcination step, as a result, the technique is more suitable for the synthesis of nano crystallites of different shapes and sizes. Also synthesis can be carried out using reactants which are normally volatile at the required reaction temperature. These volatile reactants may condense during the reaction inside the closed pressure vessel and thus helps in maintaining good stoichiometry of the synthesized product [57–60]. A large portion of the samples investigated in this thesis work were synthesized using hydrothermal reaction. The reaction was carried out using a Parr instrument designed autoclave (vessel no- 4744). A hot air oven (model no- UF 55^{PLUS}) manufactured by Memmert was used for heating and drying purpose. A schematic diagram of hydrothermal reaction process followed for the sample preparation is shown in Fig. 2.1 Various steps involved in the samples synthesis using hydrothermal and precipitation reaction process are described in the subsequent sections.

2.3 Synthesis of α-Fe_2O_3

α-Fe_2O_3 samples of various sizes and morphologies studied in this thesis work were synthesized using hydrothermal/solvothermal synthesis technique [61, 62]. Cuboid shaped α-Fe_2O_3 samples were synthesized in two different sizes namely *big cuboids* of side length $\sim$ 200 nm and *small cuboids* of side length $\sim$ 60 nm. Similarly, hexagonal plate shaped α-Fe_2O_3 samples were synthesized in two different sizes namely *micro plates* of side length (thickness) $\sim$ 1-2 μm ($\sim$ 0.5 μm) and *nano plates* of side length (thickness) $\sim$ 70 nm ($\sim$ 10 nm). Peanut shaped porous α-Fe_2O_3 samples containing spherical nano particles of $\sim$ 30 nm was synthesized by following a simple hydrothermal route described below.

Synthesis of big cuboids

For the synthesis of big cuboids $FeCl_3.6H_2O$ and urea were used as starting materials. In the typical synthesis, 1.10 g of $FeCl_3.6H_2O$ and 1.21 g of urea were dissolved in 40 ml of DDW under sonication. After complete dissolution of the reactants, 2.82 g of formamide was added into the solution. Here formamide acts as a structure directing agent which helps the nucleated particles to aggregate selectively in different directions. The whole mixture was stirred properly and then finally transferred into the Teflon-lined stainless steel autoclave of 45 ml capacity. The autoclave was heated at 160 °C for a period of 12 hours and then allowed to cool to the room temperature naturally. The precipitate deposited at the bottom of the Teflon cup was collected by the centrifugation and then washed repeatedly using DDW and ethanol. The collected precipitate finally dried at 80 °C for 7 hours before any characterization. Following this process the product obtained was weighed around 300 mg.

Synthesis of small cuboids

For the synthesis of small cuboids, the procedure used for the big cuboid synthesis was employed with a little modification. Keeping all the synthesis parameters same, 1.18 g $Fe(NO_3)_3.9H_2O$ was used instead of $FeCl_3.6H_2O$ as the Fe precursor source. The final product weighed was around 200 mg.

Synthesis of micro plates

For the typical synthesis of micro plates, first solution 'A' was prepared by mixing 0.55 g of $FeCl_3.6H_2O$ in 10 ml of absolute ethanol. A second solution 'B' was prepared by dissolving 1 g of NaOH pellets in 20 ml of DDW. Solution A and B were mixed properly under sonication to form a homogeneous mixture. The mixture was then transferred into a 45 ml capacity of Teflon-lined stainless steel autoclave and heated at 160 °C for 10 hours. After the completion of reaction, the precipitate was collected by centrifugation and washed repeatadely using DDW and ethanol. The product was Finally dried at 80 °C for 7 hours before any characterization.

Synthesis of nano plates

0.55 g of $FeCl_3.6H_2O$ was first dissolved in 20 ml of ethanol containing trace amount of DDW (1.4 ml). 1.6 g of Sodium acetate (NaOAc) was then added into the solution. After the complete dissolution of NaOAc, the mixture was transferred into a 45 ml capacity of Teflon-lined stainless steel autoclave. The autoclave was heated at a temperature of 180 °C for a period of 12 hours in the normal oven. After the reaction completed, the precipitate was collected through centrifugation, washed extensively using DDW and ethanol and finally dried at 80 °C for 7 hours.

Synthesis of porous α-Fe_2O_3

In a typical synthesis of porous α-Fe_2O_3 2.2 g of $FeCl_3.6H_2O$ was first dissolved in 8 ml of DDW. A separate solution was prepared by dissolving 0.35 g of NaOH pellets in 8 ml DDW. Both the sloutions were mixed properly under sonication and transferred into the Teflon-lined stainless steel autoclave. The reaction was carried out for 12 hours at a temperature of 160 °C. The precipitate was collected through centrifugation, washed extensively using DDW and ethanol and finally was dried at 80 °C for 7 hours.

2.4 Synthesis of MCO_3 (M : Mn, Fe, Co and Ni)

A large portion of the carbonate samples such as $CoCO_3$, $NiCO_3$, $FeCO_3$ were synthesized using hydrothermal reaction [63–65]. For the synthesis of $MnCO_3$ a simple precipitation reaction was followed [66]. The process involved in the synthesis of respective samples are described below.

Synthesis of $CoCO_3$

$CoCO_3$ sample was synthesized using cobalt acetate and urea as the source of cobalt and carbonates respectively. In a typical synthesis 0.62 g of cobalt acetate, 3 g of urea and 36 mg of cetyltrimethylammonium bromide (CTAB) surfactant were dissolved in 60 ml of DDW. The mixture was stirred properly and transferred into Teflon-lined stainless steel autoclave of 125 ml capacity. The reaction was carried out at 160 °C for a period of 12 hours. After the reaction completed, pink colour product was extracted through the process of centrifugation. The product was washed extensively using DDW and ethanol and air dried for 3-4 hours before any characterization.

Synthesis of $NiCO_3$

For the synthesis of $NiCO_3$, 10 g of nickel nitrate and 15 g of sodium dicyanamide were dissolved in 90 ml DDW. The mixture was stirred approximately for 15 mins and then transferred into the Teflon-lined stainless steel autoclave of 125 ml capacity. The reaction was carried out at 200 °C for 48 hours. The light green colour precipitate deposited at the bottom of the Teflon cup was washed with DDW and ethanol alternatively and finally air dried before characterization.

Synthesis of $FeCO_3$

In the typical synthesis, 946 mg of $FeCl_3.6H_2O$, 1.23 g of urea, 1.25 g of ascorbic acid and 1.0 g ployvinylpyrrolidone (PVP) as a surfactant were dissolved in 33 ml of DDW. After substantial stirring, the mixture was transferred into the autoclave of 45 ml capacity and heated at 130 °C for 3 hours. After completion of the reaction, the black colour precipitate deposited at the bottom of the Teflon cup was collected through centrifugation and finally air dried before characterization.

Synthesis of $MnCO_3$

$MnCO_3$ precipitation occurs when ammonium bicarbonate was mixed with manganese sulfate solution. In the typical synthesis of $MnCO_3$, a nano seed solution was first prepared by mixing 20 mg of ammonium bicarbonate and 10 mg of manganese sulfate in 100 ml of DW under rapid stirring. A target solution was prepared by mixing 50 ml of the nano seed solution with the 250 ml of 6 mM aqueous manganese sulfate solution under rapid stirring. Into the target solution a 250 ml of 0.06 M ammonium bicarbonate solution was mixed. The mixture was heated at 80 °C for 40 mins in an oven. The solid product deposited at the bottom was washed extensively with DDW and ethanol and then air dried to get the final product.

The list of starting materials, reaction conditions used for the sample synthesis are summarized in Table 2.1. Additional samples, which were not investigated in the present work but are interesting from the weak ferromagnetic and piezomagnetic point of view, have also been synthesized during the course of the study. Details of their synthesis process with basic characterization are given in Appendix-2.

Sample	Starting materials	Reaction conditions
Big cuboids of α-Fe_2O_3	$FeCl_3.6H_2O$, urea, formamide	160 °C , 12 hours
Small cuboids of α-Fe_2O_3	$e(NO_3)_3.9H_2O$, urea, formamide	160 °C , 12 hours
Micro plates of α-Fe_2O_3	$FeCl_3.6H_2O$, NaOH, ethanol	160 °C , 10 hours
Nano plates of α-Fe_2O_3	$FeCl_3.6H_2O$, NaOAc, ethanol	180 °C , 12 hours
Porous α-Fe_2O_3	$FeCl_3.6H_2O$, NaOH	160 °C , 12 hours
$CoCO_3$	$Co(CH_3CO_2)_2.4H_2O$, urea, CTAB	160 °C , 12 hours
$NiCO_3$	$Ni(NO_3)_2.6H_2O$, $NaN(CN)_2$	200 °C , 48 hours
$FeCO_3$	$FeCl_3.6H_2O$, urea, ascorbic acid, PVP	130 °C , 3 hours
$MnCO_3^*$	$MnSO_4.4\ H_2O$, ammonium bicarbonate	80 °C, 40 mins

Table 2.1 – List of starting materials and reaction conditions followed for the synthesis of α-Fe_2O_3 and various carbonate samples. The * mark denotes the precipitation reaction followed to synthesize the $MnCO_3$ sample at a relatively lesser reaction time and temperature.

2.5 Characterization techniques

2.5.1 X-Ray Diffraction (XRD)

X-ray diffraction (XRD) is a most powerful and widely used nondestructive technique for the identification and characterization of compounds based on their diffraction pattern [67]. When a monochromatic X-ray beam of wave length λ incident on a crystalline material, the periodic arrangements of atoms in the crystal acts like a three dimensional grating for the X-rays to scatter. The X-rays scattered elastically from the electrons of the atoms arranged periodically in planes separated by interplanar spacing d as shown in Fig. 2.2 (a). The scattered X-rays undergo constructive interference to produce diffraction patterns according to Bragg's law

$$n\lambda = 2dsin\theta \tag{2.1}$$

where θ is the scattering angle and $2dsin\theta$ is the path difference between two scattered waves.

For an ideal specimen the Bragg law should result in an infinitely sharp diffraction peak. However, imperfections such as stress/strain, defects or disorder present in the sample generally lead to broadening of the diffraction peak profile. The parameter full width at half maximum (FWHM) which describes the width of the diffraction peak at half of its maximum height is commonly used as a measure of the broadening of a diffraction peak. In addition to the factors intrinsic to the sample, error associated with the experimental set up such as monochromator, axial divergence also lead to peak asymmetry and broadening. Thus a diffraction peak profile shape is a convolution of both sample and instrument dependent factors and can best be modelled by the combination of Gauss and Lorentz functions as discussed in section 2.5.2.

In the present thesis work, the diffraction measurements were carried out using a Bruker D8 Advance powder X-ray diffractometer which works in Bragg-Brentano geometry (Fig. 2.2 (b)). In this geometry the sample stage remains fixed and the X-ray source and detector both move simultaneously at θ degree/min. The diffraction patterns were recorded using Cu-Kα radiation ($\lambda = 1.54178$ Å) at the tube operating voltage of 40 kV and current 30 mA. The samples were grounded properly using motor and pestle before performing the diffraction experiments. The diffraction pattern obtained was initially matched with the reference provided by the Joint Committee on Powder Diffraction Standard (JCPDS) database (Fig. 2.2 (c)).

We have also carried out temperature dependent synchrotron X-ray diffraction mea-

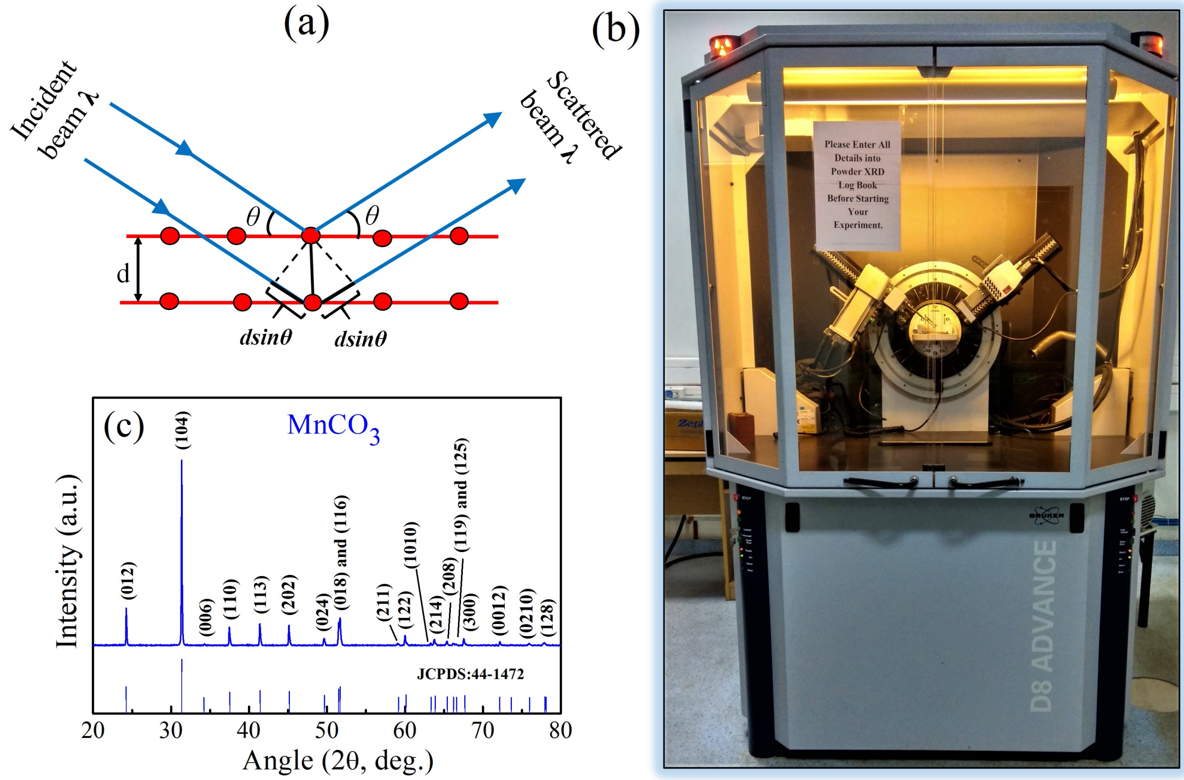

Figure 2.2 – (a) Geometrical illustration of the condition of X-ray diffraction from the crystal planes and Bragg's law. (b) Bruker D8 Advance Powder X-ray diffractometer used for the diffraction experiment. (c) A representative X-ray diffraction pattern of $MnCO_3$. Pattern indexing is done with respect to the JCPDS card no. 44-1472

surements from room temperature down to 20 K at the Indian beam line located at Photon Factory synchrotron radiation facility, Japan. Photon Factory is an accelerator based radiation source facility where X-rays are produced through the acceleration of charged particles at relativistic speed in a curved path guided by a magnetic field. A main advantage of the synchrotron X-ray source over the laboratory X-ray source is its high coherence and flux intensity which makes it an indispensable tool for structural investigations with high resolution. For detailed structural characteization, the diffraction profiles were further investigated by the Rietveld refinement analysis as described below.

2.5.2 Rietveld refinement of the XRD data

Rietveld refinement is a computer based technique used for the extraction of detail structural information of a material from its X-ray diffraction data [68]. The factors that determine the intensity of a X-ray diffraction profile can be expressed as

$$y_{ic} = y_{ib} + \sum_{\Phi} S_{\Phi} \sum_{k} m_k L_k |F_k|^2 P_k A_k G_{\Phi}(2\theta_i - 2\theta_k) \tag{2.2}$$

where the sum is over all phases ϕ and all reflections k.

y$_{ib}$ - the background of the diffraction pattern

S - the arbitrary scale factor

m - the multiplicity of a given hkl reflection

L - Lorentz polarization factor

F - structure factor

P - preferred orientation factor

A - absorption correction factor

G - diffraction profile peak shape function

In the Rietveld refinement technique, a model diffraction profile based on informations containing the hypothesized crystal structure and instrumental parameters as described above is first calculated. The model or calculated diffraction profile *y(calc)* is tried to fit with the experimentally observed one *y(obs)* by adjusting the parameters that describes the diffraction profile. The fitting is performed using a non linear least square approach and is carried out until a best fit is obtained between the *y(obs)* and *y(calc)*. The quantity which is aimed to minimize during the least square refinement process is the Rietveld residual (S) defined as [68, 69]

$$S = \sum_i w_i \left(y_i(obs) - y_i(calc)\right)^2 \tag{2.3}$$

where $w_i = 1/y_i(obs)$ is the statistical weight, $y_i(obs)$ and $y_i(calc)$ are the observed and calculated intensities at the $\mathrm{i^{th}}$ step respectively

The goodness of fit (GOF) is defined by the ratio of two numerical R values given by the expression

$$\chi^2 = \frac{R_{wp}}{R_{exp}} \tag{2.4}$$

Here R_{wp} is the weighted-profile R value expressed as

$$R_{wp} = \left\{ \sum_i w_i \left[y_i(obs) - y_i(calc)\right]^2 / \sum_i w_i \left[y_i(obs)\right]^2 \right\}^{1/2} \tag{2.5}$$

and R_{exp} is the expected profile R value expressed as

$$R_{exp} = \left[1/\sum_i^N w_i y_i(obs)^2 \right]^{1/2} \tag{2.6}$$

In the ideal condition when the model predicts the true value, R_{wp} approaches R_{exp}. A good fitting (true global minima) is then defined by the value of χ^2 close to 1.

In this thesis, detail structural analysis such as bond angle, bond length, lattice parameters, and electron density distribution of the samples have been estimated by the Rietveld refinement analysis using FullProf suite. In a typical refinement protocol, first the scale factor, background of the diffraction pattern and zero shift error were refined sequentially. Next the peak shape of the diffraction pattern was refined using the standard pseudo Voight (pV) peak shape function. A pseudo Voight function is a linear combination of both Gaussian (G))and Lorentzian (L) peak shape functions expressed as pV(x) = η L(x) + (1-η) G(x).

Here η is the mixing parameter that characterizes the Gaussian (G))and Lorentzian (L) peak shape contribution. The FWHM as a function of 2θ for the Gaussian and Lorentzian component of the pV peak shape function can be expressed as [69]

$$(H_K)_G = [U\ tan^2\theta + V\ tan\theta + W]^{1/2} \tag{2.7}$$

$$(H_K)_L = X\ tan\theta + Y/cos\theta \tag{2.8}$$

During refinement, the parameters $U,\ V,\ W,\ X, Y$ and η were refined sequentially. Finally, structural parameters such as atomic positions and site occupancy were refined. The fitting progress was checked after every step of the refinement by comparing the values R_{wp} and R_{exp}. Whenever possible, all variable parameters were refined together for final run. However, a good fitting does not always lead to a true global minima which can be identified from the non-physical values of the fitting parameters while refining the diffraction data [70]. In samples, where Rietveld refinement could not converge in a logical way, a structure free refinement such as Le-Bail fit embedded in the FullProf suite was followed for the evaluation of lattice parameters.

2.5.3 Neutron Diffraction (ND)

Like X-rays, neutrons have wave length comparable to atomic spacing and hence can diffract according to Bragg's law of diffraction [23, 71]. Neutrons are electrically neutral and hence, unlike X-rays, neutrons penetrate deep into the matter and scatter directly from the nuclei of the atoms through nuclear forces. The nuclear scattering cross section largely varies from nuclei to nuclei and therefore diffraction experiment performed with neutrons helps in localizing lighter element if present in a sample. However, the most important property of a neutron is it possess a magnetic moment. The spin of a neutron can interact with the magnetic atom through dipolar-dipolar interaction [71]. Due to this, neutron diffraction experiment is particularly advantageous for the investigation of microscopic magnetic structure. Similar to the X-ray diffraction technique, the samples that are to be investigated are bombarded with a highly monochromatic beam of neutrons. The diffracted beam collected at the detector can contain both the nuclear and magnetic Bragg reflections if the sample is in the magnetic state. If the sample is in paramagnetic state the diffraction pattern only comprises of nuclear Bragg reflections. Reflections that are purely of magnetic origin can be found through the subtraction of the diffraction patterns recorded in both the states. In the present thesis, the temperature variation of powder neutron diffraction measurement was carried out using neutron beam of $E = 6.5$ keV ($\lambda = 1.89$ Å) at the High Resolution Powder Diffractometer for Thermal Neutrons (HRPT) beam line, Paul Scherrer Institute (PSI), Switzerland.

2.5.4 Scanning Electron Microscope (SEM)

Scanning electron microscope (SEM) uses electrons for imaging, in a similar way like an optical microscope uses visible light [72]. A schematic representation of different components of a SEM is shown in Fig. 2.3 (a). A stream of electrons first produced by the electron gun made with a Tungsten filament. These primary electrons then accelerated by the positively charged anode. The stream of highly energetic electrons then pass through a set of magnetic lenses that are condenser and objective lenses respectively. Both the magnetic lenses use to converge the electron beam. In addition, the main job of condenser lens is to control the size of the electron beam which ultimately defines the image resolution and the main job of objective lens is to focus the beam on to the sample. As the name suggests, imaging is basically done by sweeping or scanning the beam in a grid fashion over the sample surface which is basically done by the scanning coils situated above the objective lens. The highly energetic focused electron beams finally

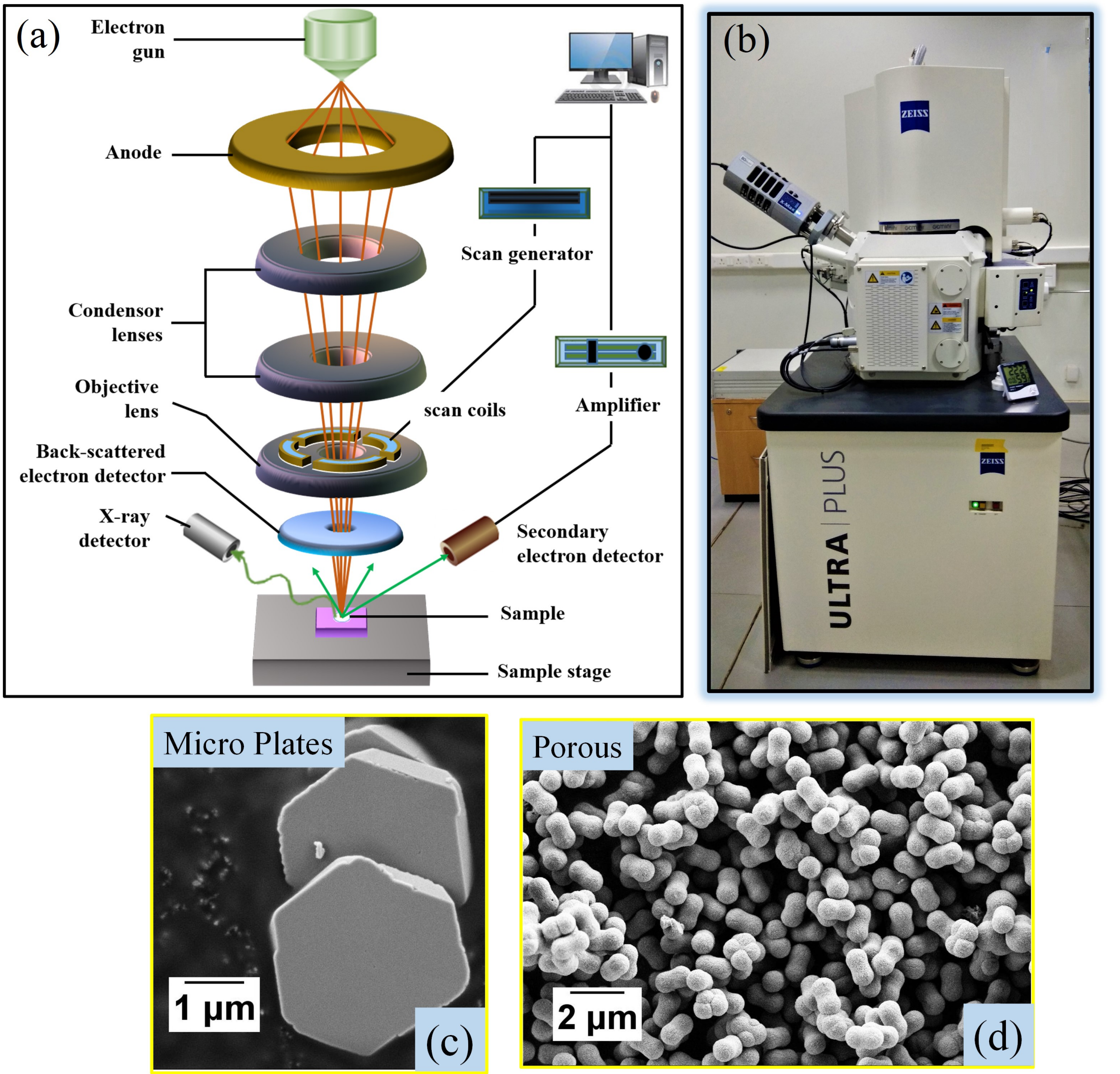

Figure 2.3 – (a) Schematic diagram of a SEM. (b) Zeiss Ultra Plus FESEM used for imaging purpose. Representative SEM images of (c) Hexagonal micro plates (d) porous α-Fe_2O_3.

allowed to fall on the sample. The electron beam interacts with the sample and produces different energies of electrons and photons. In SEM, electrons those are important for imaging purposes are the secondary electrons (SE) and back scattered electrons (BSE). The SE electrons originate from nearly the surface of the sample and hence are useful for the surface morphology and topography analysis. BSE are basically the primary electrons scattered back from deeper regions of the sample and hence are useful for the analysis of different elements present in the sample. These electrons are collected by their corresponding detectors and converted into electrical signals. The signals are finally amplified and fed into the display unit to view the images.

In the present thesis work, the shape and morphology of the samples were analysed using a Zeiss Ultra Plus field emission scanning electron microscope (FESEM) at 3 kV operating voltage (Fig. 2.3 (b)). A FESEM is eqipped with a field-emission type electron gun that emits electrons from an area which is much smaller than the area of thermionic guns. Correspondingly the electron beam probe size is much narrower in FESEM that results in better quality images with higher resolution and magnification. FESEM images of two representative samples micro plates and porous hematite is shown in Fig. 2.3 (c) and (d) respectively.

2.5.5 Energy Dispersive Analysis of X-rays (EDAX)

The energy dispersive analysis of X-rays (EDAX) is a technique that employs characteristic X-rays for the analysis of elemental/chemical compositions of a material [72]. For compositional analysis, an EDAX system is commonly attached with a SEM instrument where the electron gun of the SEM is used as an excitation source. When a specimen is excited with a highly energetic electron beam, the incident electron beam can knock out an electron from the inner shells of the atoms of the specimen. An electron from the outer most electronic state can jump immediately to fill the ground state vacancy. The X-rays emitted in this process carry energy that is characteristic to the energy difference between the upper and lower orbitals of the particular element. An EDAX detector is used to convert the amount of characteristic X-rays of different energies emitted from the specimen into the respective voltage pulses. The relative comparison between the intensities of different voltage pulses finally use to determine the approximate composition of the specimen volume in weight percentage (wt%) or atomic percentage (at%).

A representative EDAX spectra recorded to determine the elemental composition of the small cuboids of α-Fe_2O_3 is given in Fig. 2.4.

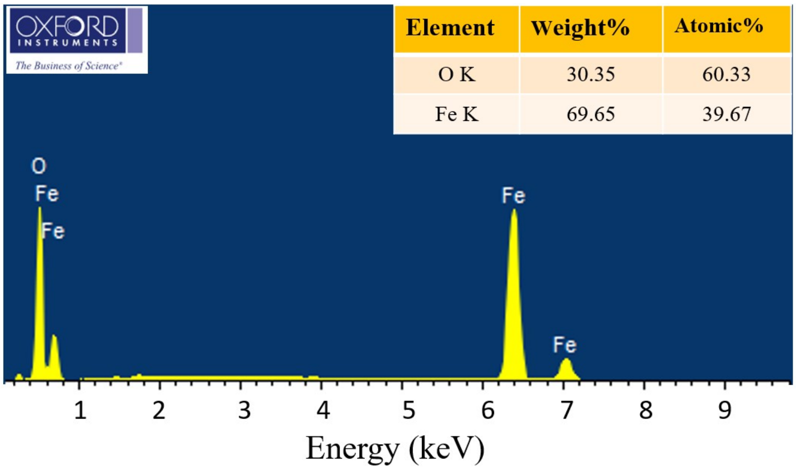

Element	Weight%	Atomic%
O K	30.35	60.33
Fe K	69.65	39.67

Figure 2.4 – A representative EDAX spectra recorded for small cuboids of α-Fe_2O_3.

2.5.6 SQUID Magnetometer

A magnetometer is an instrument that measures the magnetic flux density (B) according to the principle of Faraday's law of induction. Magnetometers that work with the technology of Superconducting Quantum Interference Device (SQUID) are the most sensitive instrument known so far to precisely measure an extremely small change in the magnetic field [73]. A SQUID comprises of a superconducting loop interrupted by two Josephson junction. The magnetic flux inside a superconducting loop is always quantized and can only exist in multiples of the Flux quanta

$$\Phi = \frac{2\pi\hbar}{2e} \approxeq 2.07 \times 10^{-15} Wb \tag{2.9}$$

The working principle of SQUID is based on the phenomenon of this flux quantization and the Josephson effect for which it works as an extremely sensitive current to voltage converter [74]. The sensitivity is such that any small change in the magnetic field $\sim$ flux quanta can be detected by measuring the voltage across the SQUID sensor.

The basic components of a magnetometer are the cryogenic dewar, sample rod, superconducting electromagnet/magnet, superconducting pickup coil, SQUID sensor and the electronic control system. The dewar stores the liquid helium used for the electromagnet to keep in the superconducting state and to cool the sample chamber as well. A liquid nitrogen jacket surrounds the dewar to prevent the excess liquid helium boiling off. The sample chamber is located within the superconducting pickup coil. The pickup coil is surrounded by the superconducting magnet that generates a longitudinal uniform magnetic field. For measurements, the sample is first loaded inside a gelatin capsule and then inserted into a plastic straw. The straw is attached to one end of the sample rod and the other end of the sample rod is connected to a stepper motor. The stepper motor's function is to drive (or scan) the sample position vertically (along let say Z-axis) inside the superconducting pickup coil so hence the magnetic moment of the sample produced by the magnetic field of the superconducting magnet can couple inductively to the pickup coils. The pickup coil made from a single piece of superconducting wire and is designed in a second order gradiometer configuration as shown schematically in (Fig. 2.5 (a)). The top and bottom coils are the single turns wounded clockwise whereas the center coil has two turns wounded counter clockwise. The gradiometer configuration allows to precisely measure the stray field signals from the sample while nullifying the contributions from any other external signals.

In the present study the magnetic measurements were carried out using a MPMS XL SQUID magnetometer manufactured by Quantum Design, USA. Before starting any measurement, the sample was positioned at the center of the gradiometer set up precisely. This corresponds to the point of maximum response of the SQUID output voltage for a total scan length across the gradiometer coil as shown in Fig. 2.5 (b). The SQUID output voltage noted as a function of total scan length across the gradiometer coil finally fitted

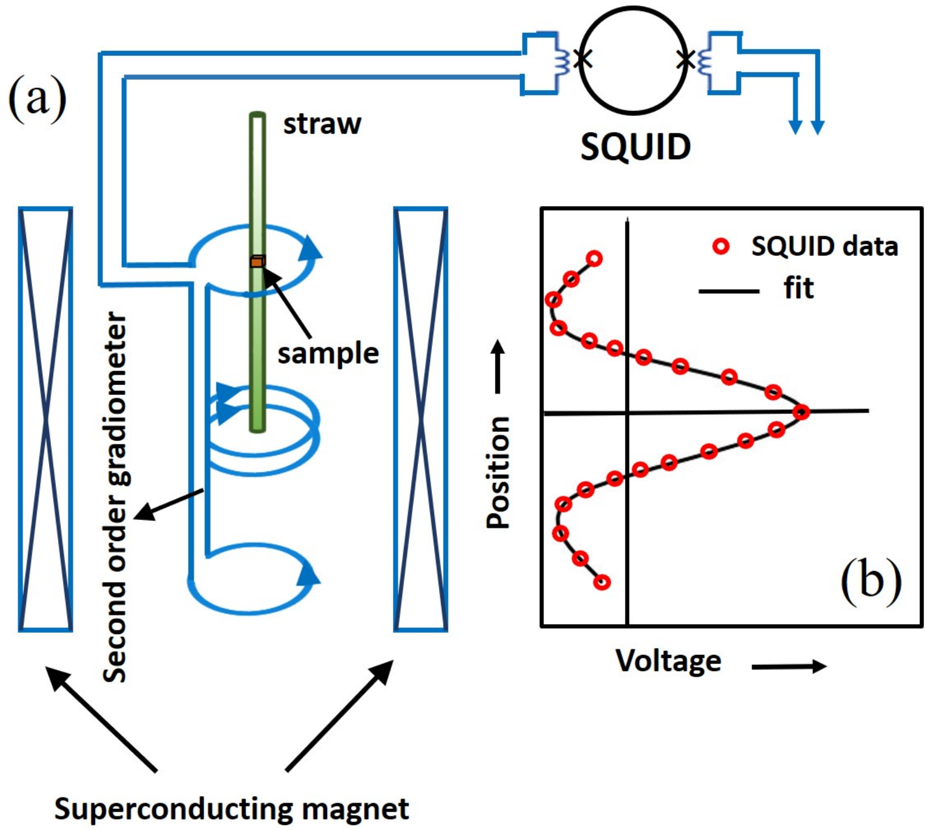

Figure 2.5 – (a)Second order gradiometer coil geometry. A magnetic sample positioned inside a plastic straw moves through the gradiometer coil set up. The voltage generated through the process according to Faraday's law of induction is coupled to the SQUID for magnetization measurement (b) The SQUID ouput voltage profile as a function of sample position inside the gradiometer coil.

with a curve fitting algorithm provided by the MPMS software to extract the magnetic moment. A complete scan was repeated a number of times and the signals resulted each time finally averaged out to improve the signal-to-noise ratio.

2.5.7 Dielectric Spectroscopy

Dielectric spectroscopy is a technique used to measure the dielectric and electric properties of materials such as ceramics, semiconductors, polymers etc as a function of frequency and temperature [75]. Dielectric measurement using parallel plate geometry arrangement is a well known method. The technique involves sandwiching a material between two parallel electrodes (copper plates) forming a sample capacitor. A schematic diagram demonstrating the dielectric measurement set-up is shown in Fig. 2.6. A sinusoidal voltage V_o with frequency $\omega/2\pi$ is applied across the sample capacitor. The applied voltage V_o made a current I_o to flow across the sample with the same frequency $\omega/2\pi$ but with a phase difference ϕ that depends on the electrical properties of the dielectrics such as the conductivity, permittivity etc.

The applied voltage and the current develops across the sample capacitor in the complex notation can be written as

$V(\mathrm{t}) = V_o \cos(\omega \mathrm{t}) = \mathrm{Re}\ (V^* \exp(\mathrm{i}\omega \mathrm{t}))$

$I(\mathrm{t}) = I_o \cos(\omega \mathrm{t} + \phi) = \mathrm{Re}\ (I^* \exp(\mathrm{i}\omega \mathrm{t}))$

Here

$$V^* = V_0, \quad I^* = I^{'} + iI^{''} \ \ ; I_0 = \sqrt{I^{'2} + I^{''2}} \ \ ; tan\phi = \frac{I^{''}}{I^{'}}$$

A complex impedance (Z^*) then defined as

$$Z^* = Z^{'} + iZ^{''} = \frac{V^*}{I^*} \tag{2.10}$$

An impedance analyzer connected across the sample capacitor measures the complex impedance Z^* and the phase ϕ. Finally the dielectric constant (ϵ^*) can be calculated from the complex impedence (Z^*) by using the following relation

$$\epsilon^*(\omega) = \epsilon^{'} + i\epsilon^{''} = \frac{-i}{\omega Z^*(\omega)} \frac{1}{C_0} \tag{2.11}$$

where C_0 is the capacitance of the empty capacitor when air is a medium.

Dielectric properties were measured in this thesis work using an Alpha-A high performance impedence analyzer from Novocontrol technology. For low temperature measurements the samples were cooled through a thermodynamic refrigeration process using a Closed Cycle Refrigerator (CCR) manufactured by Cryo Industries of America, Inc

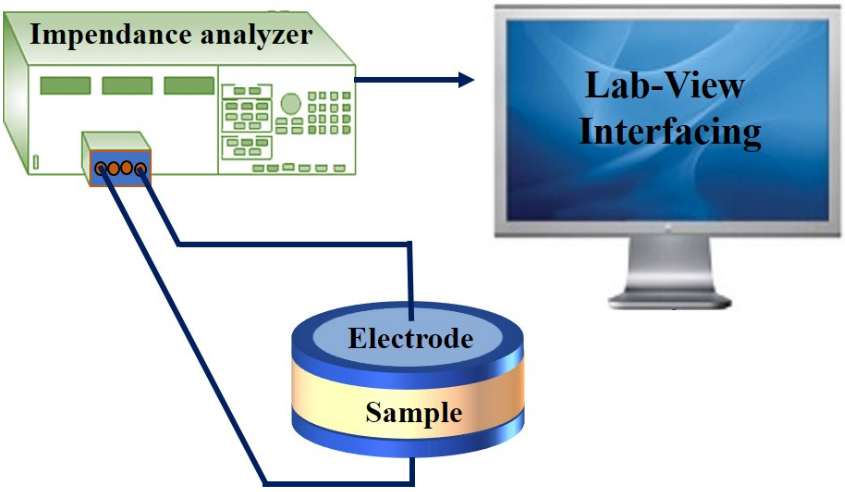

Figure 2.6 – Schematic of dielectric measurement set up.

(Model-204-N). A home-made sample holder compatible with the CCR set up was used for low temperature measurements.

2.5.8 Raman Spectroscopy

Raman spectroscopy technique is based on the inelastic scattering process through which it probes the vibrational level of the molecules in a sample [76].

In a Raman spectroscopy experiment, a sample (solid, liquid, or gas) is perturbed with a highly coherent monochromatic electromagnetic wave. The oscillating electric field of the electromagnetic wave excites the molecules of the sample to the virtual states. The molecules in the virtual states are short lived and they relax back to the ground state by scattering photons. The scattered photon collected at the detector contains information about the molecular vibrations. Mostly a major portion of the scattered photons have frequency equal to the incident photon and this elastic scattering process is called as Rayleigh scattering. A small percent of incident photon undergo change in frequency and this inelastic scattering process is called as Raman scattering. The increase in frequency (incident photon frequency plus the vibrational frequency) is known as an Anti-Stokes scattering and the decrease in frequency (incident photon frequency minus the vibrational

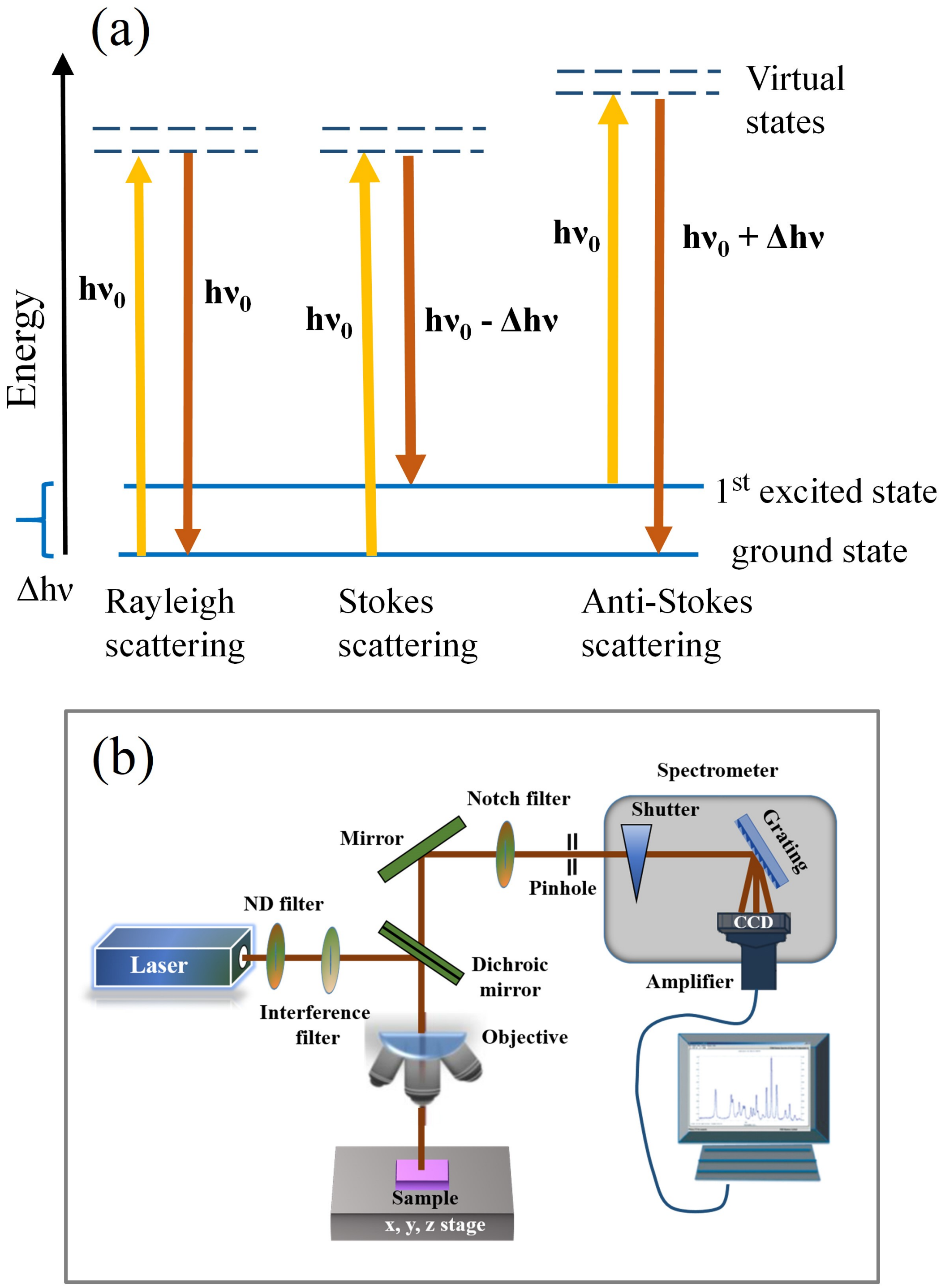

Figure 2.7 – (a) Jablonski diagram of Quantum Energy Transitions for Rayleigh scattering, Stokes (Raman) scattering, and Anti-Stokes (Raman) scattering. (b) Schematic diagram of a typical Raman spectrometer.

frequency) is known as Stokes scattering. These quantum energy transition processes are described pictorially in Fig. 2.7 (a). By measuring the Raman shift, which is the change in scattered photon frequency from the incident photon frequency, one can get informations about the vibrational frequency of the molecules in a sample. Since the number of molecules in the ground state is higher than the excited state, the intensity of Stokes scattering is generally higher than the anti-Stokes scattering. A Raman spectrum is thereby basically a plot of intensity of stokes scattering versus the Raman shift. Since different materials have different vibrational modes, Raman spectra acts as a finger print to identify the materials. A schematic illustration of the main components of a Raman spectrometer is shown in Fig. 2.7 (b). Since Raman effect is very weak (intensity of stokes scattering $\ll$ Rayleigh scattering) a highly monochromatic light such as a laser light with high flux intensity is generally used to excite the sample. A microscope is used to focus the laser light onto a very small region ($<$ 1-100 μm) of the sample. The scattered light from the sample travels back through the microscope optics and the notch filter into the spectrometer. The notch filter filtrates out the stokes scattered light from the Rayleigh and anti stokes scattered lights. The Raman shifted light is dispersed according to wave length through the spectrometer grating and detected with the charge coupled device (CCD) detector. The signal recorded at the detector finally fed into a computer for data acquisition. In this thesis work, Raman spectroscopy measurements were carried out using a Horiba LabRAM micro Raman system. The samples used for the measurement were in the pellet form. A He-Ne laser of wave length 532 nm was used to excite the samples. The incident laser light was focused to a spot size of $\sim$ 2 μm and the scattered light was collected using a 50 X objective lens.

Chapter 3

Quasi-static remanence in Dzyaloshinskii-Moriya Interaction driven weak ferromagnets

3.1 Introduction

In some symmetry allowed weak ferromagnets and piezomagnetic compounds or in their doped versions an *ultra-slow* relaxation of magnetization was tracked through the Thermoremanent (TRM) measurements [49]. Interestingly, this ultraslow relaxation of remanence was also observed in various nanoscaled Cr_2O_3 systems [51–53]. This led to the observation of a *quasi-static* remanence, which was also seen to vary with the magnetic field H in a counter-intuitive way [52, 53]. These intriguing features of remanence pointed its origin to be connected with the phenomenon of weak ferromagnetism/piezomagnetism present in an otherwise AFM. However, Cr_2O_3 is not a symmetry-allowed WFM/PzM in bulk but *quasi-static* remanence is seen to be present in its various nano versions. A systematic investigation of this phenomenon is, therefore, required in understanding whether these unique features of remanence are intrinsic to symmetry allowed WFM/PzM.

In view of this, in this chapter we present a systematic investigation of magnetization and TRM in a series of isostructural AFMs, more specifically, in $MnCO_3$, $CoCO_3$ and $NiCO_3$ and $FeCO_3$. Out of these, the first three compounds are symmetry allowed WFM with the spin canting angle larger in $NiCO_3$ and smaller in $MnCO_3$ [18, 77–83]. They belong to the same crystal structure as that of α-Fe_2O_3 and are also symmetry allowed to show the phenomenon of piezomagnetism under the application of an external stress [18, 28, 84]. The orbital contribution to the magnetic ground state in all these isostructural carbonates are quite different. The orbital contribution remains largely unquenched in $CoCO_3$, which leads to a strong spin-orbit coupling (SOC) and consequently a large single ion anisotropy (SIA). This SIA is relatively strong in $CoCO_3$ as compared to $MnCO_3$ and $NiCO_3$ [4, 85]. Thus systematic investigation of thermoremanent magnetization in this series of prototypical DMI driven carbonates will be certainly interesting keeping in view of the fine differences in the SOC influenced by their respective orbital contributions.

The forth compound, namely $FeCO_3$ is not a symmetry allowed WFM [18] but reported to be a PzM [28, 30]. Since this compound is isostrutural with the remaining three carbonates, we intended to explore the nature of remanance in this compound. Also, similar to the case of Cr_2O_3 [51–53] whether nanoscaling in $FeCO_3$ would also result in generation of WFM/PzM traits is another issue we intend to explore. The crystallographic and magnetic characterization, along with the remanance data on $FeCO_3$ is presented in a separate section, at the end of this chapter.

All four carbonates used for the study are in the powder form synthesized by the hydrothermal and precipitation methods and have thoroughly been characterized using the XRD and SEM techniques. The magnetization and the thermoremanent magnetization in the samples have been measured by SQUID magnetometry. The magnetization, hereafter referred to as M is measured in routine Field Cooled cycle (FC), in which the sample is cooled in a fix magnetic field (H) from above its magnetic transition temperature. At the lowest temperature, the H is removed and the thermoremanent magnetization (μ) is measured, either as a function of increasing temperature (T) or time (t). In this thesis, thermoremanent magnetization is also referred as remanent magnetization or simply remanence with the symbol μ.

3.2 Results and discussion

3.2.1 XRD and SEM

The SEM micrographs presented in Figs. 3.1 (a)-(b) show the samples of $MnCO_3$ and $CoCO_3$ are cuboid in shape. The side lengths of each cuboid in $MnCO_3$ and $CoCO_3$ are $\sim$ 4 and 10 μm respectively. In case of $NiCO_3$, each individual grains, which are in the shape of a regular polyhedra, (Fig. 3.1 (c)) consists of rectangular plates of size $\sim$ 1-5 μm. The X-ray diffraction patterns fitted with Rietveld refinement using FullProf software is shown in Fig. 3.1 (d). The diffraction patterns confirm the samples are stabilized in the hexagonal R-3c symmetry and are free from any impurity or secondary phases. The lattice parameters extracted from the Rietveld analysis is presented in Table 3.1. The contraction in the lattice parameters as can be noticed from Table 3.1 is expected due to the continuous reduction in the ionic radii while going from Mn to Ni. The unit cell of the isostructural carbonates generated in the VESTA programme using crystallographic information inputs obtained from the Rietveld analysis is shown in Fig. 3.1 (e). Each M^{2+} ion coordinated with the six oxygen atom forms a distorted MO_6 octahedral structure. The unit cell consists of stacks of MO_6 and CO_3 layers. The spins belong to the M^{2+} ion coupled ferromagnetically with in the basal plane and antiferromagnetically along the c-axis of the unit cell. Furthermore the antiferromagnetic coupling between the adjacent layers is not perfect. The antiferromagnetic spins belong to the adjacent layers are slightly canted as a result of DMI to generate a weak ferromagnetic moment in these system [85–87]. We have also conducted temperature variation of synchrotron XRD mesurement in a representative carbonte sample $MnCO_3$. The variation of lattice parameters with temperature as determined from the Rietveld analysis is discussed in the later part of the text.

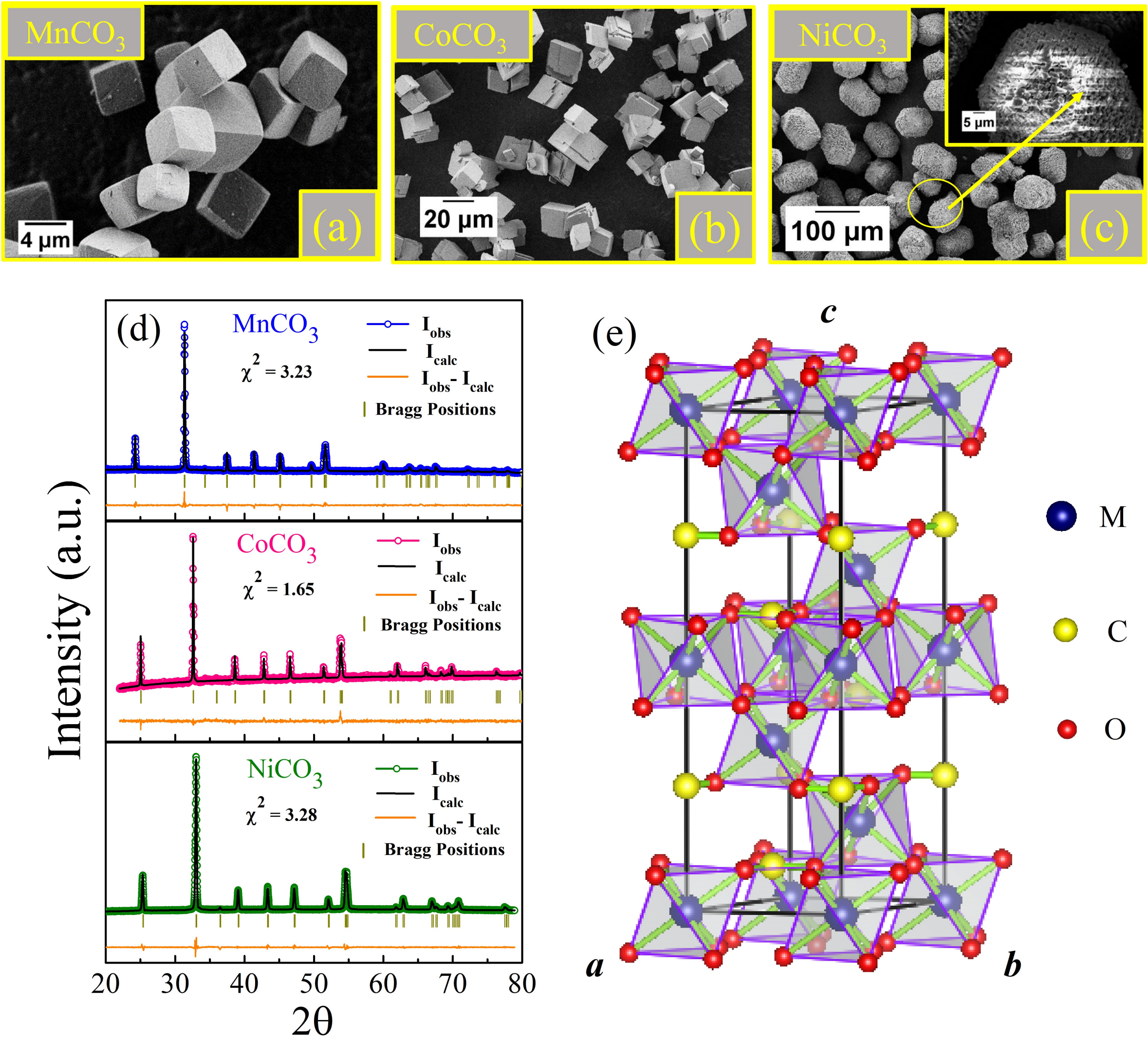

Figure 3.1 – SEM images of the cuboids of (a) $MnCO_3$, (b) $CoCO_3$ and (c) $NiCO_3$. (d) Room temperature XRD data of all three carbonate samples fitted with Rietveld refinement. (e) Depicts a representative unit cell of MCO_3, generated in the VESTA programme using crystallographic information inputs obtained from the Rietveld analysis of the diffraction data.

Sample	a (Å)	c (Å)	c/a
$MnCO_3$	4.7993(2)	15.6943(8)	3.27
$CoCO_3$	4.6612(3)	14.9678(2)	3.21
$NiCO_3$	4.6059(4)	14.7677(1)	3.20

Table 3.1 – Lattice parameters of $MnCO_3$, $CoCO_3$, and $NiCO_3$ extracted from the Rietveld analysis of room-temperature lab X-Ray diffraction data.

3.2.2 Magnetic characterization: M vs T and M vs H

In this section, we first present the basic magnetic characterization (M versus T and M versus H) for all the three WFM carbonates. The magnetization (M) as a function of temperature (T) curve obtained for all samples at an applied field of H = 100 Oe is shown in Fig. 3.2 (a). The Néel temperature (T_N) of the samples noted from figure 3.2(a) are ∼ 30, 24 and 18 K respectively for $MnCO_3$, $NiCO_3$ and $CoCO_3$. These values match well with the literature values [78, 88, 89]. One feature, which distinguishes the weak ferromagnets from the normal or routine ferromagnets is that the DM interaction is not present in the Hamiltonian (thermodynamic potential) of these routine ferromagnets. As a result, while the routine ferromagnets obey the standard Curie-Weiss law between the magnetic susceptibility and temperature, weak ferromagnets obey a modified Curie-Weiss law derived by Moriya [19, 90].

$$\chi = \frac{C(T - T_0)}{(T - \theta)(T - T_N)} \tag{3.1}$$

where χ is the dc susceptibility of the sample, T is the temperature, θ is the Weiss temperature, C is the Curie constant, T_N is the Néel temperature and T_0 is the fitting parameter. The ratio $\frac{(T-T_0)}{(T-T_N)}$ in the susceptibility formula results directly from the DM interaction. Our samples do obey this modified law. For example, the inverse susceptibility vs temperature curve in one representative weak ferromagnetic sample, $CoCO_3$, fitted using the above equation is presented in the inset of Fig. 3.2 (a). The best fitted parameters obtained from the fit are C = 3.7004, θ = -70.11, T_N = 17.59 and T_0 = 16.56. The main panel of Fig. 3.2 (b) shows the typical M vs H curve recorded for $MnCO_3$ at 5 K. The loop opening is clearly depicted in the inset of the figure. The MH isotherms recorded for $CoCO_3$ and $NiCO_3$ are shown separately in Fig. 3.2 (c). The open hysteresis loop and non saturation of magnetization observed below T_N is a reflectance of the weak ferromagnetic traits in otherwise AFMs.

Remanent magnetization in the samples is prepared using a measurement protocol where the samples are first cooled well above from their respective T_N down to 5 K at different constant magnetic field H. This is a typical field cooled (FC) cycle. The magnetization data recorded while field cooling the samples is denoted as M_{FC}. After a typical M_{FC} measurement the applied H is turned off at 5 K and the remanent magnetization (denoted as μ_{FC}) prepared in this way is measured either (i) as a function of increasing temperature from 5-100 K or (ii) as a function of time while keeping the temperature constant at 5 K. The behaviour of remanent magnetization explored in the series of carbonate samples are discussed below.

3.2.3 Magnetization and Remanance (μ) in MnCO$_3$: $\boldsymbol{H}$ variation

The M_{FC} vs T curve (black dots) recorded while cooling in presence of $H \sim 100$ Oe is shown in Fig. 3.3 (a). After the typical M_{FC} versus T measurement, the applied magnetic field is turned off at 5 K and the corresponding μ_{FC} recorded with the increase of temperature is shown with the blue dots in Fig. 3.3 (a). The very first observation is that, the magnitude of μ_{FC} is comparable with the magnitude of M_{FC}. For instance, the magnitude of M_{FC} at 5 K is 0.75 emu/g. After removal of field at 5 K, the magnitude of μ_{FC} is $\sim$ 0.7 emu/g. This indicates, after removal of field, a very small part of magnetization decays instantaneously, however, a significant part of magnetization remains pinned. Also, on increasing the temperature, while $H = 0$, the μ_{FC} versus temperature curve follows a path qualitatively similar to the variation of M_{FC} with T right up to the T_N of MnCO$_3$ (Fig. 3.3 (a)).

Along the similar way the remanent magnetization obtained for an applied field of $H =$ 30 kOe is shown in Fig. 3.3 (b). Here the magnitude of M_{FC} at 5 K is $\sim$ 12 emu/g whereas

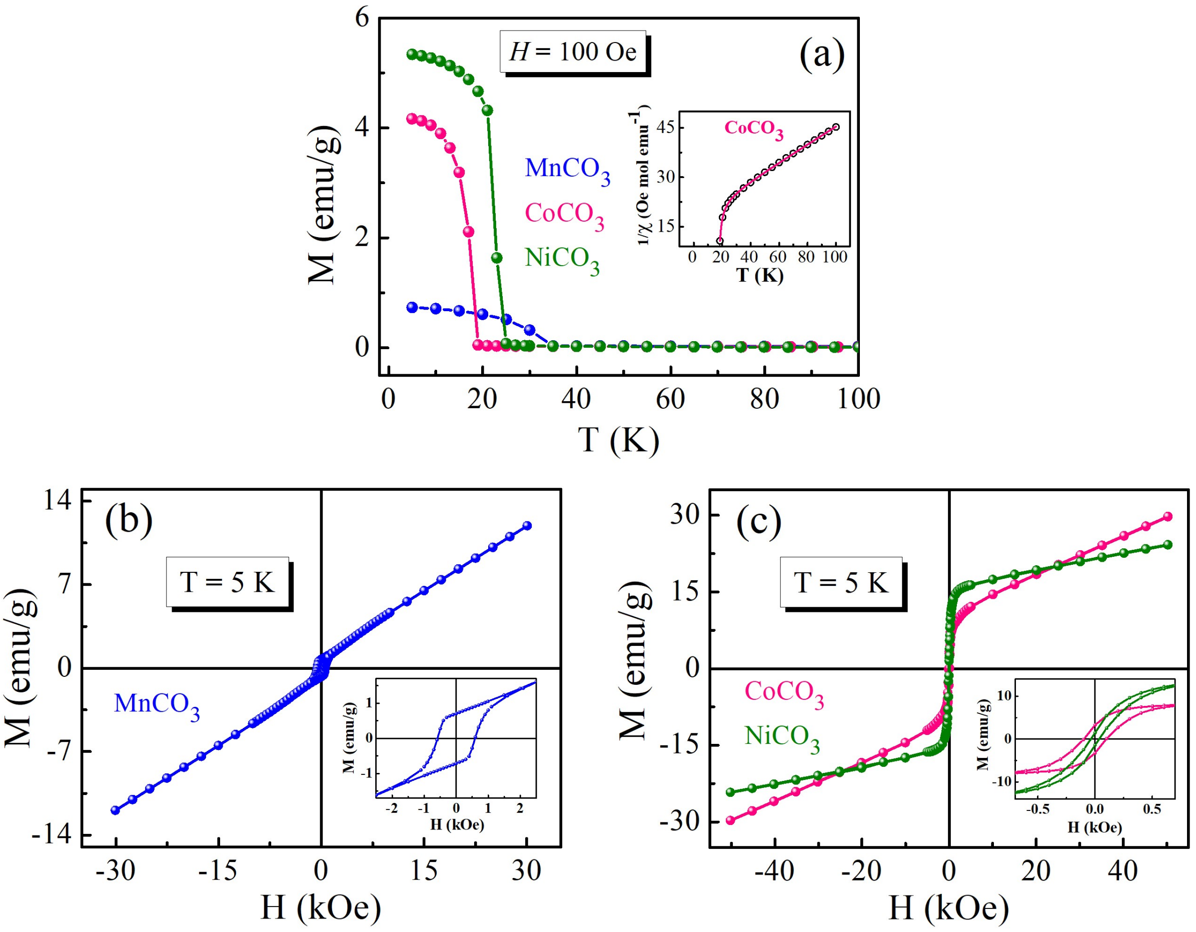

Figure 3.2 – (a) Magnetization as a function of temperature recorded for all the three carbonate samples in presence of H = 100 Oe field. Inverse susceptibility vs temperature curve obeying modified Curie-Weiss law is shown in the inset for a representative weak ferromagnetic sample $CoCO_3$. (b) M vs H curve recorded for $MnCO_3$ at 5 K. Same recorded for $NiCO_3$ and $CoCO_3$ is shown separately in (c). The loop opening is clearly depicted in the inset of the figures.

the magnitude of μ_{FC} is $\sim 10^{-5}$ emu/g. Thus the magnitude of μ_{FC} is vanishingly small when the remanence prepared at higher magnetic field values. This vanishingly small magnitude of μ_{FC} can be considered roughly arising due to the quenched field associated with the superconducting magnet of the SQUID magnetometer whose value roughly lies around $\sim$ 5-10 Oe and can also vary from run to run.

The M_{FC} versus T and the corresponding μ_{FC} versus T curves measured at all intermediate field values are presented in Fig. 3.3 (c) and (d) respectively. From Fig. 3.3 (c) it is evident that the M_{FC} increases with the increase of H as is obvious for a regular

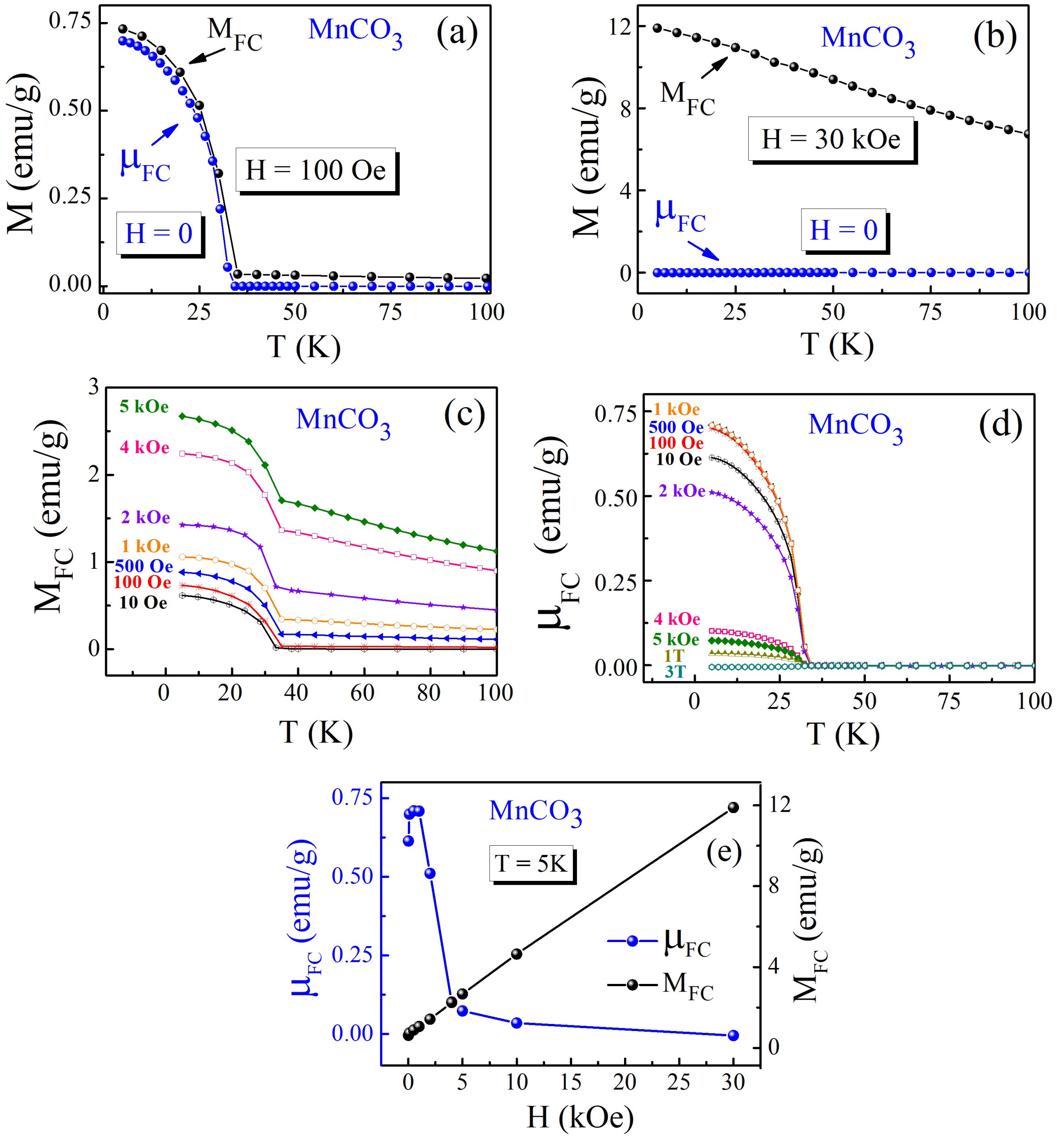

Figure 3.3 – (a) M_{FC} vs T (black dots) and the corresponding μ_{FC} vs T (blue dots) at H = 100 Oe recorded for MnCO$_3$. The same recorded for H = 30 kOe is shown in (b). (c) M_{FC} vs T curves recorded at different cooling H depicting the regular AFM behavior with M_{FC} rising with the rise in H. (d)Corresponding μ_{FC} vs T exhibits a counter-intuitive cooling H dependence. (e) Comparison of the magnitude of M_{FC} (black dots) and the corresponding μ_{FC} (blue dots) as a function of cooling H at 5 K. The counter-intuitive dependence of μ_{FC} with H is clearly evident from the figure.

AFM, whereas the corresponding remanence varies with the cooling H in a quite unusual way. To clearly bring out this fact, the variation of M_{FC} with H at 5 K is plotted in conjunction with the variation of μ_{FC} with H in Fig. 3.3 (e). Here the M_{FC} values and the corresponding μ_{FC} values are picked up from the various M_{FC} and the corresponding μ_{FC} versus T runs recorded at different cooling H. Here the M_{FC} increases linearly with the increase of H (black dots) whereas the corresponding μ_{FC} (blue dots) first seen to rise with the H, attains a maximum value at some critical H, and then sharply decreases with the further increase of H. The remanence eventually vanishes beyond another critical H value. Thus in contrary to M_{FC}, the μ_{FC} in $MnCO_3$ varies in a counter-intuitive or unusual way with the strength of cooling H.

3.2.4 Remanance (μ) in $MnCO_3$: variation with *time*

We performed magnetization relaxation measurements as a function of time in $MnCO_3$. To measure the same after a typical FC cycle the applied magnetic field is turned off to zero at 5 K. The remanent magnetization thereafter measured as a function of time while the temperature held constant at 5 K. Fig. 3.4 (a) shows the remanent magnetization as a function of time obtained for a cooling H of 100 Oe in $MnCO_3$. The data clearly depicts two distinct time scale of magnetization relaxation process. After removal of H, a part of magnetization decays instantaneously from the initial M_{FC} value (only one data point shown). This instantaneous drop in magnetization is clearly evident from Fig. 3.4 (a). However, a significant part of the magnetization remains pinned and does not show appreciable decay measured up to a time scale of 2 hours. Similar relaxation measurement performed at other selected field values is shown in Fig. 3.4 (b). Here the magnitude of remanence prepared at the cooling H of 5 kOe is less than the magnitude of remanence prepared at other two cooling H values. This is consistent with the data presented in Fig. 3.3 (c) depicting the counter-intuitive dependence of remanence with the strength of magnetic field. Also it can be noticed that the initial drop in the magnitude of remanence that occurs after the immediate removal of the H is large when the remanence prepared at higher H values. For instance, the magnitude of remanence retained after the removal of $H \sim 100$ Oe at 5 K is ~ 95 % of its in-field M_{FC} value. These values for the cooling H of 1 and 5 kOe are 70 and 3% respectively. Nevertheless the remanence relaxation is always ultra-slow irrespective of the cooling magnetic field used to prepare the remanent state. This ultra slow relaxing remanence can be termed as *Quasi-static* or *time-stable* remanence.

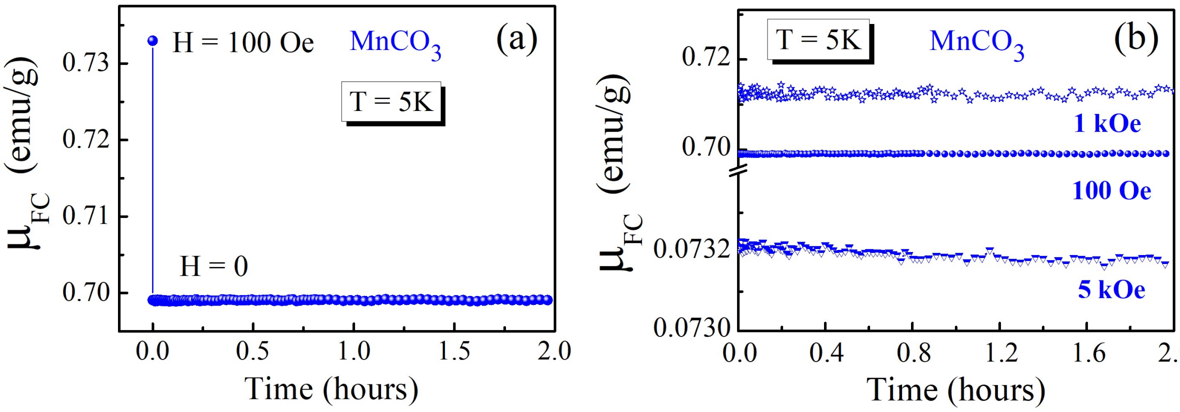

Figure 3.4 – (a) Remanence as a function of time at 5 K for a cooling H of 100 Oe in $MnCO_3$. Remanence as a function of time at 5 K for the three different cooling H. These data depicts the *quasi-static* nature of remanence that remains almost constant over a time period of 2 hours.

3.2.5 Experimental evidence of robust magnetization pinning

The presence of *time-stable* remanence as observed in $MnCO_3$ implies a robust magnetization pinning process. To understand the fact more clearly we consider the case of $MnCO_3$ as shown in Fig. 3.5. Here the sample is first cooled from the paramagnetic region down to 5 K in presence of a $H = +\ 100$ Oe field. The M_{FC} data recorded while cooling is represented in the blue dots. After the typical FC cycle, the applied magnetic field is removed at 5 K and holding the temperature constant at that 5 K, a reverse magnetic field of $H = -\ 100$ Oe is applied. The magnetization data M_{FH} subsequently recorded in the heating cycle is presented in the black dots. It is observed that the magnetization

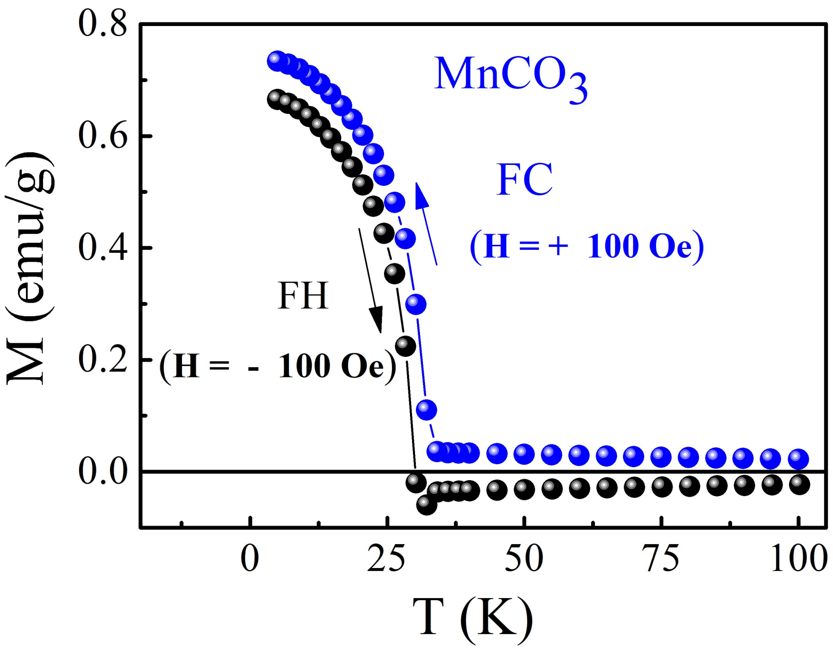

Figure 3.5 – Blue dots represent the M versus T recorded while cooling in presence of H = +100 Oe. At 5 K, the H = +100 Oe is removed and H = -100 Oe is applied while the temperature is held constant at 5 K. The M vs T measured subsequently in presence of H = -100 Oe in the warming cycle is represented in the black dots. The robustness of pinned moment is clearly evident from this data.

measured for the applied field of H = - 100 Oe in the warming cycle is positive. The magnetization remains positive even up to the T_N of the sample. This implies the magnetization prepared while the field cooling process remains pinned even after the removal of H. The pinning is so robust that an applied of H = - 100 Oe is not sufficient enough to reverse the direction of magnetization in the entire weak ferromagnetic region. The measured magnetization in the warming cycle is basically therefore the positive remanence that is prepared while field cooling the sample in presence of a positive guiding magnetic field of H = + 100 Oe. This indicates the robustness of the magnetization pinning in this DMI driven WFM.

3.2.6 Magnetization and Remanance (μ) in NiCO$_3$

The M_{FC} versus T and the corresponding μ_{FC} versus T curves measured for another DMI driven WFM sample, NiCO$_3$ are shown in Fig. 3.6 (a) and (b) respectively. The magnitude of M_{FC} at 5 K for the applied field of $H = 50$ Oe is 3 emu/g (Fig. 3.6 (a)). After turning off the H to zero, the magnitude of corresponding μ_{FC} is $\sim$ 1.4 emu/g (Fig. 3.6 (b)). Similarly, the M_{FC} value at 5 K for the 2 kOe run is 21 emu/g, whereas, the corresponding μ_{FC} value is negligibly small. The variation of M_{FC} and the corresponding μ_{FC} as a function of (cooling) H for $NiCO_3$ is shown in Fig. 3.6 (c). Here the M_{FC} (black dots) increases in a non-linear fashion with H whereas the corresponding μ_{FC} (green dots) first increases with the increase of H, peaks up at some critical H and then decreases with the further increase of H. The remanence eventually vanishes at some other critical H. Thus the trend of variation of μ_{FC} with H observed in $NiCO_3$ is qualitatively similar to $MnCO_3$. The critical field values, where the remanence peaks up and vanishes for both the samples, are however different. Remanence variation with time measured for three different cooling H for $NiCO_3$ is presented in Fig. 3.6 (d). Here again , similar to the case of $MnCO_3$, the *quasi-static* nature of remanence is also evident in $NiCO_3$. However, Unlike the case of $MnCO_3$ the remanence relaxation in $NiCO_3$ proceeds through several jumps. This jump like feature in the remanence data is only exclusive to $NiCO_3$ and is not observed in other carbonate samples.

3.2.7 Magnetization and Remanance (μ) in $CoCO_3$

The M_{FC} versus T and the corresponding μ_{FC} versus T curves recorded for $CoCO_3$ are shown in Fig. 3.7 (a) and (b) respectively. The H dependence of μ_{FC} in $CoCO_3$ has a different scenario compared to the other two carbonate samples. Here the magnitude of μ_{FC} obtained at the highest applied H of 50 kOe is on par with the magnitude of μ_{FC} obtained at 50 Oe field value (Fig. 3.7 (b)). Unlike the case of $MnCO_3$ and $NiCO_3$, the remanence in $CoCO_3$ does not vanishes with the increase of cooling H. The remanence rather increases slightly with the increase of cooling H as shown in Fig. 3.7 (c) .

The relaxation measurement performed at three selective field values is shown in Fig.

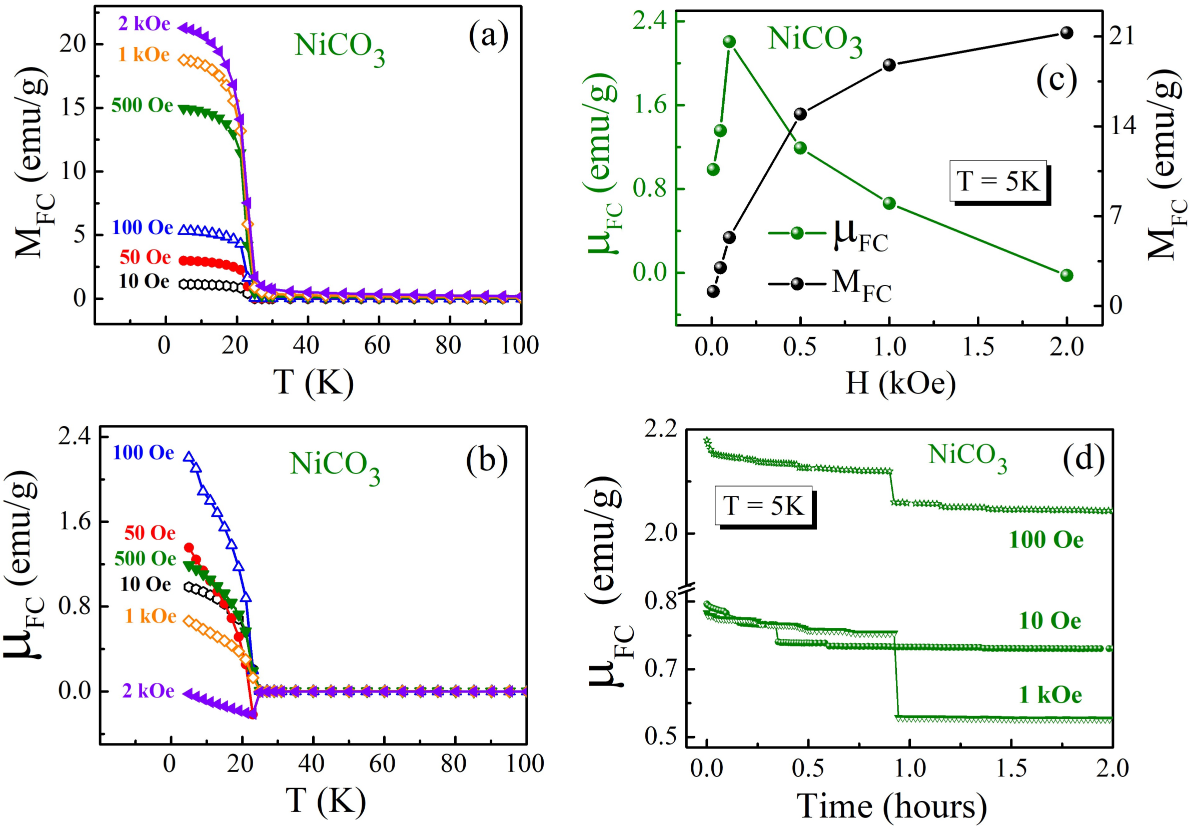

Figure 3.6 – (a) M_{FC} versus T at different cooling H in NiCO$_3$, (b) The corresponding μ_{FC} versus T curves obtained at different cooling H. (c) (Black dots) variation of in-field magnetization with H; the corresponding remanent magnetization (green dots) shows a counter-intuitive H dependence. (d)Remanence as a function of time at three different cooling H.

3.7 (d). The remanence in CoCO$_3$ appears to be less stable with time compared to other two carbonate samples. The remanence relaxation however, does not follow a single exponential decay. After systematic data fitting we found that the remanence relaxation in CoCO$_3$ can be described by a superposition of three single exponential decay function

$$\mu(t) = \mu_1 e^{\frac{-t}{\tau_1}} + \mu_2 e^{\frac{-t}{\tau_2}} + \mu_3 e^{\frac{-t}{\tau_3}} \tag{3.2}$$

where μ_1, μ_2, μ_3 and τ_1, τ_2 and τ_3 are the coefficients and decay times of the function respectively. The solid curve in the main panel is the triple exponential fit to the μ_{FC} versus time data. The decay time extracted for the particular H of 5 kOe with τ_1 (=

0.03 h) $< \tau_2$ (= 0.2 h) $< \tau_3$ (1.8 h) implies a slow relaxation process in $CoCO_3$. We see that the remanence relaxation in $CoCO_3$ can also be described by a logarithmic decay as shown in the inset of figure. Overall, the magnetization relaxation in $CoCO_3$ can be anticipated to be different from that in conventional FMs or AFMs.

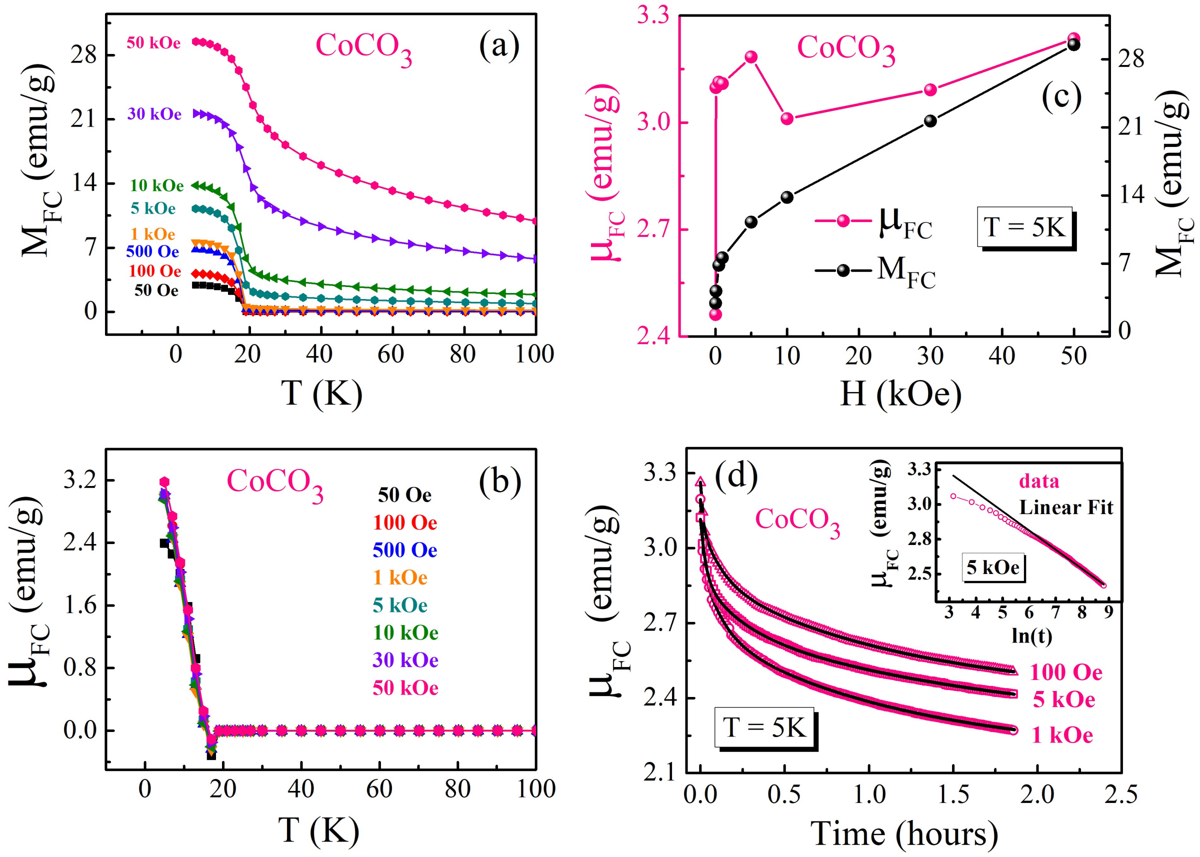

Figure 3.7 – (a) M_{FC} versus T at different cooling H in $CoCO_3$, (b) The corresponding μ_{FC} versus T curves obtained at different cooling H. (c) Variation of in-field magnetization (black dots) and the corresponding remanent magnetization (pink dots) with H. (d) Main panel shows the variation of remanence with time at three different cooling H following the triple exponential decay function depicted with the black solid line. The inset shows the logarithmic dependence of remanence with time.

From the relaxation measurement performed in all the three carbonate samples, we generally notice two distinct time scale of magnetization relaxation process one of which is ultraslow leading to the observation of *quasi-static/time-stable* remanence. The presence of *quasi-static* remanence in all these carbonates is associated with a robust magnetization pinning mechanism which appears to be larger in $MnCO_3$.

To understand the physical mechanism responsible for the strong magnetization pinning that results in ultraslow magnetization relaxation in all these carbonates a number of slowly relaxing systems for instances the case of superparamagnetism (SPM), spin glasses (SG), exchange bias effect at the FM/AFM interface and the case of diluted antiferromagnets in a field (DAFF) can be taken into account [43, 46, 47, 91–96]. Such systems are known to exhibit slow magnetization relaxation that follows a number of functional forms. However, none of these phenomena appears to be the reason behind the observation of *quasi-static* remanence and its unusual/counter-intuitive H dependence as observed in the present carbonate samples. It is to be noted that the samples under our study do not come under the category of spin glasses or frustrated AFMs. The samples are regular crystallites with well defined facets and are devoid of any interface effects. Moreover, the particles are fairly big with size ranging from $\sim$ 1-20 μm. Therefore the phenomenon of nanoscale ferromagnetism or superparamagnetism can also be ruled out. Furthermore, the μ_{FC} in all the above mentioned systems including the case of regular FM or AFM should have shown saturation with H unlike the sharp drop as observed in the present carbonate samples (Fig. 3.3 (e)). Thus the fact such as coercivity responsible for the strong magnetization pinning and hence ultra-slow relaxation of remanence as observed in these weak ferromagnetic carbonates can be ruled out. It therefore appears that the ultra-slow relaxation of remanence and its unusual field dependence as observed in such bulk unstrained carbonate samples is some way connected to the weak ferromagnetic nature intrinsic to the systems.

It is to recall that the phenomenon of weak ferromagnetism observed in otherwise antiferromagnets can have two type of origin. One is due to DMI which is the antisymmetric part of the anisotropic super exchange interaction and the second one is due to the single ion anisotropy (SIA) arises as a consequence of large SOC and crystal field effects [4, 9, 19, 24, 97–99]. The later is more important for the systems with low T_N [19].

The role of orbital contribution to the weak ferromagnetism recently has been studied in these carbonates. Compared to all the canted antiferromagnets of the trigonal R-3c series, the orbital magnetic moment in $CoCO_3$ remains largely unquenched [85, 100]. The large unquenched orbital magnetic moment gives rise to a large contribution of SIA present in $CoCO_3$. Consequently, the weak ferromagnetism in $CoCO_3$ is driven both by the phenomenon of DMI as well as SIA. It is to be noted that remanent magnetization observed in $NiCO_3$ more particularly in $CoCO_3$ is less stable compared to the spin-only ($l = 0$) system $MnCO_3$ (Fig. (d) of 3.3, 3.6 and 3.7). Thus at this point, remanent magnetization investigation in weak ferromagnets driven purely by SIA may require further measurements to gain better insight on the magnetization dynamics in Ni and Co systems.

Another member of this rhombohedral carbonate series is $FeCO_3$ which was theoretically predicted by Dzyaloshinskii to show the phenomenon of piezomagnetism but not the phenomenon of weak ferromagnetism [18, 28]. The phenomenon of piezomagnetism has also been verified experimentally in the compound by Borovik-Romanov [30]. The rhombohedral unit cell contains two antiferromagnetically coupled spins of Fe^{2+} ions pointed along the body diagonal of rhombohedron (equivalent to c-axis in hexagonal unit cell) [101, 102]. The spin configuration is similar to that of AFM state of α-Fe_2O_3 which does not respect DMI to occur as pointed out by Dzyaloshinskii and Moriya [18, 19, 101, 102]. In our present investigation on remanent magnetization, we consistently observe a presence *time-stable* remanence in the series of isostructural weak ferromagnetic carbonates that are potentially PzMs [103]. Since the compound $FeCO_3$ is isostrutural with the remaining three carbonates, it is interesting to explore the nature of remanance in this compound as well. It is also to recall that, the phenomenon of weak ferromagnetism observed in otherwise AFMs depends on the magnetic symmetry. The phenomenon of piezomagnetism thereby appears in converting a pure AFM to WFM under an external stress [36]. This indicates that strain effects as a consequence of nano scaling in FeCO$_3$ could possibly play a prominent role in developing the WFM traits as has been observed in nanostructured Cr$_2$O$_3$ systems. In our present investigation of remanent magnetization, we therefore intend to explore the nature of remanence in the nanostructured FeCO$_3$ to shed light on the popssibility of weak ferromagnetism associated with it. We will discuss below the structural characterization, magnetization and the remanent magnetization results obtained in FeCO$_3$.

3.2.8 Magnetization and Remanance (μ) in FeCO$_3$

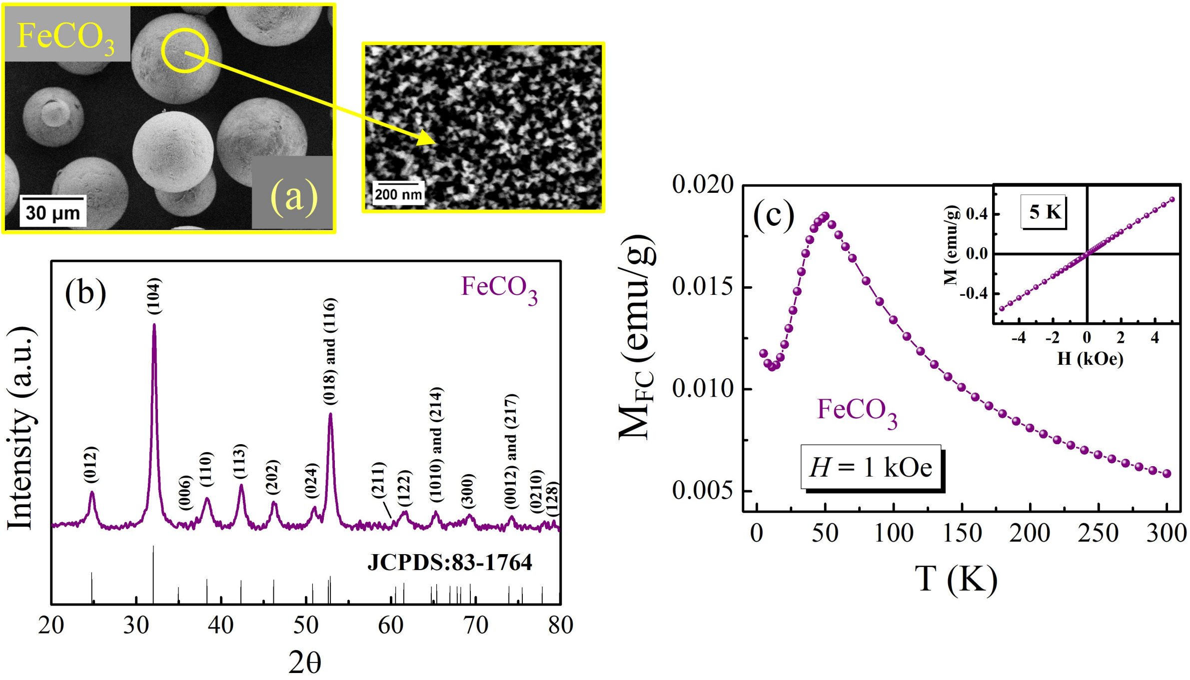

Figure 3.8 – (a) SEM image of the FeCO$_3$ micro spheres. Each micron size sphere composed of triangular grains of size ∼ 2-5 nm. (b) Laboratory souce based X-Ray diffraction data recorded at room temperature. (c) Magnetization versus temperature curve recorded while cooling in presence of H = 1 kOe field. The inset shows the MH isotherm recorded at 5 K.

Fig. 3.8 (a) shows the SEM image of the polycrystalline FeCO$_3$ micro spheres. Each big micro spheres contains triangular grains of size ∼ 2-5 nm. The room temperature XRD recorded using Cu Kα wave length is shown in Fig. 3.8 (b). The diffraction pattern contains no impurity peaks. The peak indexing is done with respect to the JCPDS number: 83-1764. Magnetization as a function of temperature measured while cooling in presence of $H = 1$ kOe is shown in Fig. 3.8 (c). The Néel temperature of the sample is consistent with the literature value [101, 102]. The inset of Figure shows the MH isotherm recorded at 5 K in the AFM region. The magnetization increases linearly with the increase of H characterizes the AFM nature of the sample.

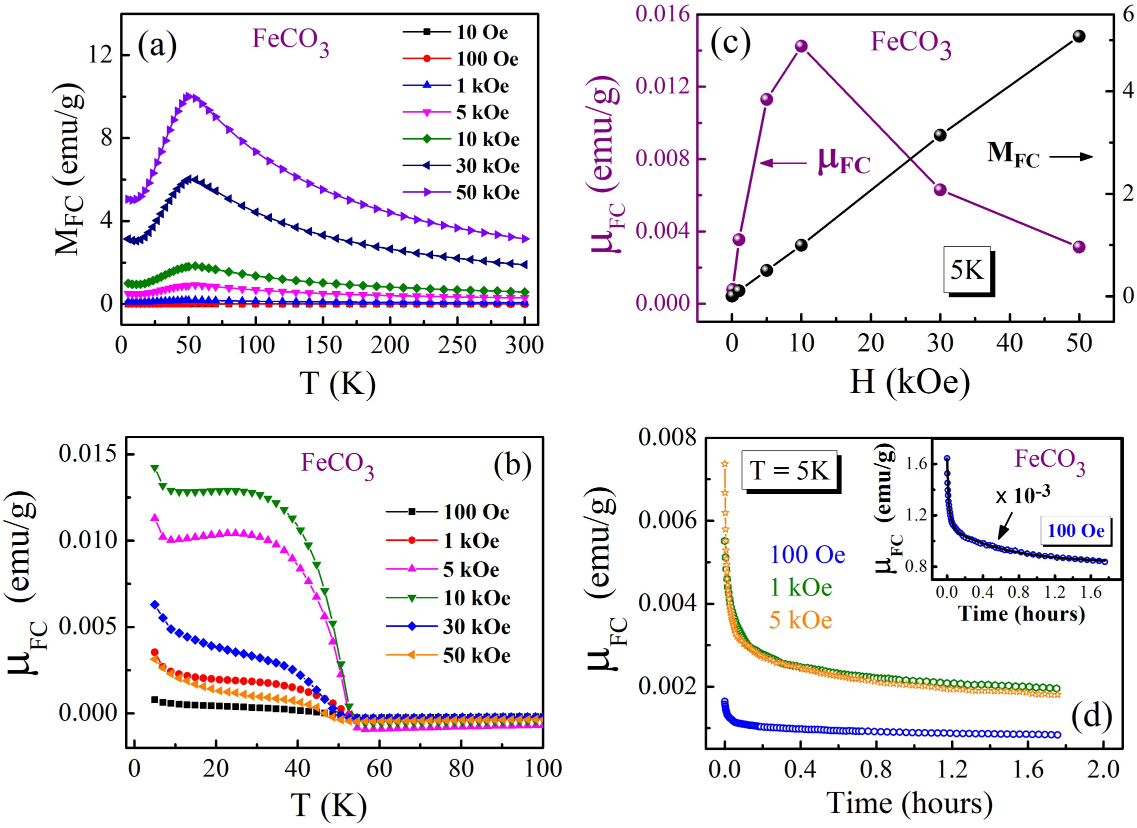

Figure 3.9 – (a) M_{FC} versus T recorded at different cooling H. (b) Corresponding μ_{FC} versus T data recorded after switching off H to zero. (c) (Black dots) variation of in-field magnetization with H; the corresponding remanent magnetization (purple dots) shows a counter-intuitive H dependence. (d)Remanence as a function of time at three different cooling H. The inset shows the remanence relaxation in $FeCO_3$ following a triple exponential decay function.

For remanent magnetization measurement the same field cooling (FC) protocol used before for preparing the remanent state for other carbonates has been followed. The M_{FC} and the corresponding μ_{FC} versus temperature curves measured at different cooling field H is presented in Fig. 3.9 (a) and (b) respectively. Interestingly the counter-intuitive dependence of μ_{FC} with H is evident in $FeCO_3$ as clearly shown in Fig. 3.9 (c). The M_{FC} increases linearly with the increase of H as it should be for a regular AFM, whereas the corresponding μ_{FC} versus H shows a peak like behaviour. As pointed out earlier, this peculiar H dependence of remanence is not related to any of the nano scale SPM, SG or irreversible magnetization contributions such as observed in AFM nano structures [46, 47]. Thus it appears that the origin of such unusual H dependence of remanence in $FeCO_3$ has similar ground as that of other weak ferromagnetic carbonates as far as nano-scaling is concerned. The magnitude of remanence is however one - two orders of magnitude smaller compared to other carbonate samples.

We next performed the relaxation rate measurement to check if the remanence has *time-stable* nature. To check the same, after a typical FC cycle the applied H is removed and the corresponding remanence measured as a function of time. These are shown in Fig. 3.9 (d) for three selective cooling H. Similar to $CoCO_3$, we see that the remanence relaxation in $FeCO_3$ can best be described by the triple exponential decay function as shown in the inset of Fig. 3.9 (d). From the present set of data obtained on ultra thin nano particles of $FeCO_3$, it appears that nano scaling results generation of WFM/PZM like features, (as seen in the remanence of symmetry allowed WFM carbonates) in this sample as well. However further investigations are needed for a firm conclusion on this matter. For instance, in ultra small nano particles, the strain in lattice parameters may lead to generation of WFM like features.

3.2.9 Remanent magnetization and structural correlation

To further probe the remanent magnetization and its correlation with structural parameters in the carbonate samples we perform low temperature synchrotron XRD measurement from 300-20 K in $FeCO_3$ and compare it with one of the WFM carbonate sample $MnCO_3$. Fig. 3.10 (a) and (b) show the representative synchrotron XRD data fitted with

Rietveld refinement for the samples $MnCO_3$ and $FeCO_3$ respectively. The lattice parameters as determined from the Rietveld refinement of the synchrotron X-ray diffraction data are shown in Fig. 3.10 (c) and (d) for $MnCO_3$ and $FeCO_3$ respectively. Here the lattice parameters are normalized with the their respective values at 300 K. It is observed that, both the lattice parameters of $MnCO_3$ and $FeCO_3$ contract with reducing temperature till about the T_N. The c-axis is seen to contract more rapidly than the a-axis. However below T_N, an expansion in both the lattice parameters is observed with reducing temperature. Fig. 3.10 (e) compares the normalized c/a ratio of both the samples. In both the samples the c/a decreases monotonically with the decrease of temperature till about their respective T_N and a subtle anomaly is observed in the AFM region below T_N. The c/a ratio in $MnCO_3$ falls relatively faster with reducing temperature compared to $FeCO_3$. This subtle difference in the behaviour of c/a ratio possibly differentiates $MnCO_3$ and other weak ferromagnetic carbonates from $FeCO_3$ in which both the magnitude and stability of remanence is less compared to other carbonates in the series.

Overall, we see that remanence in $FeCO_3$ has qualitatively similar feature as that observed in other carbonate samples. However, unlike other carbonates where the particles are bulk with size varying from 1-20 μm, in $FeCO_3$ the particles are ultra-small with size ranging from 2-5 nm. Thus the morphology of the sample makes it difficult to conclude whether the observed features of remanence are intrinsic or is restricted only to nanoscaled $FeCO_3$. The situation is similar to Cr_2O_3 which is not a WFM in bulk but develops the traits upon nano scaling [52, 53]. Further measurements on bulk $FeCO_3$ with microscopic measurements are certainly required in understanding if the qualitative features of remanence are intrinsic to the system. It is also to be noted that, it is hard to stabilize Fe in its 2+ oxidation state. This somehow hinders the formation of $FeCO_3$ in bulk form. However, after several attempts we have successfully synthesized bigger $FeCO_3$ particles of grain size ~ 0.5 μm. Remanent magnetization investigation on this

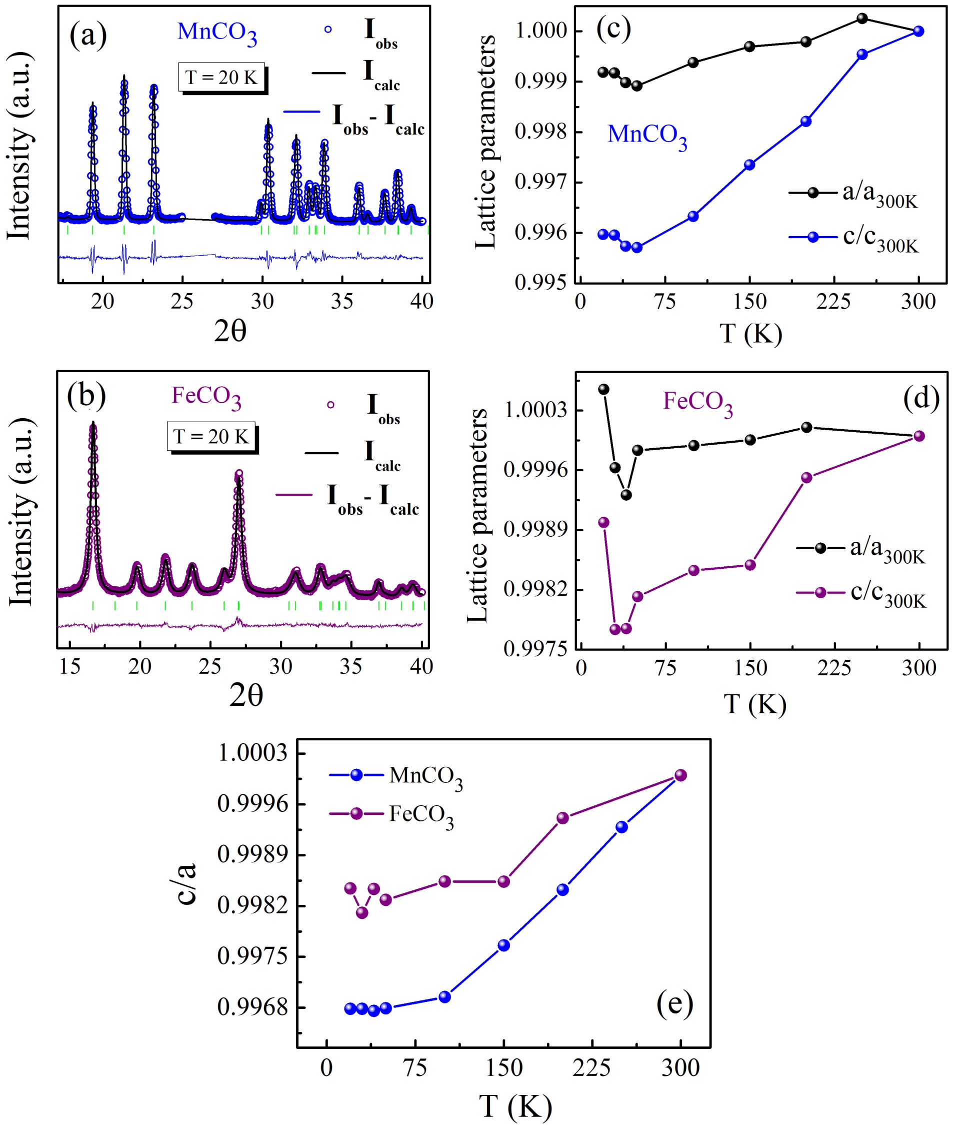

Figure 3.10 – Low temperature synchrotron XRD data with Rietveld fitting in (a) $MnCO_3$, (b) $FeCO_3$. (c) and (d) temperature variation of lattice parameters in $MnCO_3$ and $FeCO_3$ respectively. (e) Compares the temperature variation of c/a ratio for both the samples.

bigger $FeCO_3$ sample is under the way. The synthesis procedure with XRD and SEM image of the bigger $FeCO_3$ particles is given in Appendix-2.

3.3 Conclusion

To summarize the work, we have systematically explored remanent magnetization in the prototype DMI driven weak ferromagnets $MnCO_3$, $NiCO_3$ and $CoCO_3$. The remanent magnetization in these systems exhibits two distinct time scale of relaxation one of which is ultraslow leading to the observation of *time-stable* remanence. This *time-stable* remanence also varies with the strength of the magnetic field in a counter-intuitive way which is pointed out. The qualitative features of remanent magnetization as observed in the series of rhombohedral carbonates is associated with a robust magnetization pinning mechanism. This robust magnetization pinning resulting in the observation of *quasi-static* remanence indicates its origin possibly connected with the DMI driven weak ferromagnetic nature of the samples, which is different from the conventional magnetization pinning mechanism such as seen in spin glasses, exchange bias or frustrated antiferromagnetic systems. Remanent magnetization in WFMs where spin canting is not exclusively driven by DMI but also due to SIA is yet to be explored. This might help in understanding the qualitative features of remanent magnetization observed in $CoCO_3$. The remanence in nanostructured $FeCO_3$ exhibits qualitatively similar feature as that observed in the other isostructural WFMs included in our remanence study. Further measurements on a bulk $FeCO_3$ sample including microscopic measurements are also important to realize if the features are generic to the system. Remanent magnetization investigation on big $FeCO_3$ particles is also under way. Overall, the presence of *quasi-static* remanence and its counter-intuitive field dependence can possibly be taken as the footprint of weak ferromagnetism present in the rhombohedral carbonates.

Chapter 4

Time-stable remanence in room temperature weak ferromagnet α-Fe_2O_3

4.1 Introduction

As shown in the previous chapter, we find a presence of unique remanence in WFM carbonates that remains fairly stable for an experimental time scale of several hours. This *time-stable* remanence appears to be connected to the spin canting phenomenon driven by the Dzyaloshinskii-Moriya Interaction (DMI) [103]. In addition to the fundamental aspects, the presence of *time-stable* remanence in the DMI driven multifunctional compounds particularly at room temperature can have technological importance in the upcoming areas of spin based device applications [33, 34, 51]. In this context, the antiferromagnetic oxide compound α-Fe_2O_3 (hematite) is particularly an ideal candidate. The rhombohedral structure α-Fe_2O_3 is the most stable form of iron oxide enriched with exotic magnetic ground states. The compound is basically an antiferromagnet with T_N as high up to ~ 960 K. Below T_N the antiferromagnetic spins are slightly canted, giving rise to weak ferromagnetism, similar to the rhombohedral carbonates [18]. As the temperature decreases there occurs a first order spin reorientation transition below which α-Fe_2O_3 becomes a pure AFM [104]. In addition to the room temperature weak ferromagnetism

α-Fe_2O_3 is also well known for its piezomagnetic properties [28, 32, 33, 105]. Remanent magnetization investigation in such a exotic magnetic system where WFM/PzM both exists at room temperature will certainly be interesting both from the fundamental and technological aspects point of view.

We have also observed that, the magnitude of the *time-stable* remanence is higher for the compounds with larger spin canting angle [103]. For instance, $NiCO_3$ is a stronger weak ferromagnet with larger spin canting angle compared to $MnCO_3$ [82]. Consequently the magnitude of *time-stable* remanence in $NiCO_3$ is an order of magnitude higher than $MnCO_3$. In the series of rhombohedral weak ferromagnets, carbonates are known to be stronger weak ferromagnets as compared to α-Fe_2O_3 [18, 82]. Thus the magnitude of *time-stable* remanence if present in α-Fe_2O_3 is expected to be very less. Optimization of the magnitude of the *time-stable* remanence in α-Fe_2O_3 through nanoscaling is therefore certainly requierd considering it is more suitable for practical applications.

Although *time-stable* remanence is connected to the DMI driven weak ferromagnetic phase, its presence in some isostructural systems has also been realized due to the size and interface related effects. For instance, *time-stable* remanence which is usually expected not to be present in Cr_2O_3 due to the symmetry restrictions have been observed in its various nanoscale versions [51, 52]. This also indicates down scaling will certainly be promising for the optimization of the magnitude of *time-stable* remanence. Considering this fact the first part of the chapter presents remanent magnetization study in α-Fe_2O_3 crystallites synthesized in various shape, size and morphologies. The samples are in powder forms synthesized in two different shapes such as cuboids and hexagonal plates. For a given shape, key size effects have been explored in the acquisition of remanent magnetization. Finally a porous sample consisting of spherical nanoparticles of diameter 10-30 nm has also been included in the study. Comparison of the magnitude of *time-stable* remanence in all these series of α-Fe_2O_3 samples of various shape and morphologies provides a indirect way of gauging the magnitude of spin canting angle whose estimation in general is a non-trivial task.

In the second part of this chapter, we have explored remanent magnetization in a defect free pure single crystal (SC) of α-Fe_2O_3. Observation of quasi static remanence in a single crystal firmly confirms that the unusual pattern in remanence is intrinsic in nature and indeed relates to the WFM phase. The features of remanent magnetization observed in the SC of α-Fe_2O_3 also enables us to better understand the close connection between the phenomenon of weak ferromagnetism and piezomagnetism present in a system.

The rhombohedral primitive unit cell of α-Fe_2O_3 contains four Fe atoms with spins coupled antiferromagnetically in the fashion S1 = - S2 = -S3 = S4 along the [111] axis of rhombohedron (equivalently 001 axis or c-axis of conventional hexagonal unit cell) [18, 23]. Depending on the temperature region of interest α-Fe_2O_3 exists both in the weakly ferromagnetic and antiferromagnetic states with different spin configurations shown schematically in Fig. 1.5. Bulk α-Fe_2O_3 has Néel temperature (T_N) $\sim$ 960 K. Below T_N, the spins belong to the four Fe atoms lie almost in the (111) plane of rhombohedron Fig. 1.5 (a). However, the antiferromagnetic coupling among the Fe spins is not perfect. The spins are rather slightly canted to generate a small net magnetic moment similar to the case in $MnCO_3$. As the temperature goes down, Morin transition (T_M) takes place at the temperature of 260 K [104]. At T_M the spins reorient from the (111) plane towards the [111] axis (Fig. 1.5 (b)). The magnetic symmetry below the Morin transition does not allow the DMI to occur for which α-Fe_2O_3 becomes a pure AFM. Thus one can find α-Fe_2O_3 in two different magnetic states depending on the temperature region of investigation.

It is easier to visualize and understand the antiferromagnetic spin arrangements in α-Fe_2O_3 in the rhombohedral unit cell. However, for the structural analysis of the system, the hexagonal indexing is always more useful. Therefore, in the present study of structural investigation, we will follow the conventional hexagonal geometry of the unit cell.

4.2 Tuning the ***time-stable*** remanence in α-Fe_2O_3 : effect of shape, size and morphology

4.2.1 XRD and SEM

The samples shown in Fig. 4.1 (a)-(e) are synthesized using hydrothermal technique as described in section 2.3. FESEM micrographs show the samples of hexagonal plates and cubes contain grains in the form of regular shape with well-defined facets. The side length (thickness) of hexagonal micro and nano plate are $\sim$ 1-2 μm ($\sim$ 500 nm) and $\sim$ 70 nm($\sim$ 10 nm) respectively. Similarly side lengths of big and small cuboids are $\sim$ 200 nm and 60 nm respectively. The peanut shaped porous α-Fe_2O_3 sample is formed due to the coagulation of spherical nanoparticles of diameter $\sim$ 10-30 nm. The phase purity and crystallinity of the samples have been characterized by using a Bruker D8 advance powder X- ray diffractometer (XRD) with Cu Kα radiation (λ = 1.54056 Å). The diffraction patterns matched with the JCPDS card numbers are presented in Fig. 4.2.

4.2.2 Magnetization and remanent magnetization

For magnetization measurement a Quantum Design MPMS-XL SQUID magnetometer is used in the field values ranging from 100 Oe to 50 kOe. A typical MH isotherm recorded in the AFM and WFM region of the α-Fe_2O_3 micro plates is presented in Fig. 4.3 (a). The loop opening (blue dots) observed in the room temperature is associated with the weak ferromagnetic nature of the sample that vanishes in the AFM region (black dots) . The M versus T data measured for the same sample in the temperature window of 5-300 K using FC and ZFC protocol is presented in Fig. 4.3 (b). Here in the FC cycle the magnetization data was recorded while cooling the sample from 300 K to 5 K in presence of H = 100 Oe field. In the ZFC cycle, the sample is first cooled down from 300 K to

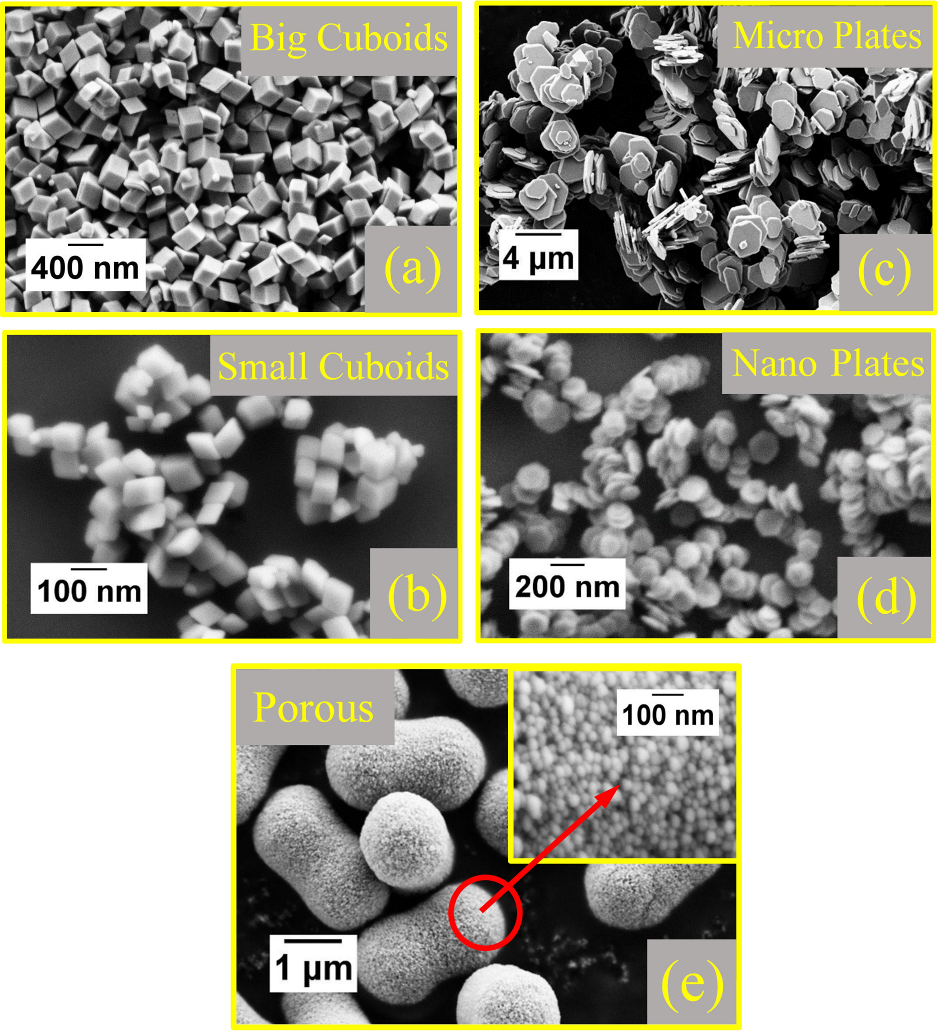

Figure 4.1 – SEM images of (a) big cuboids, (b) small cuboids, (c) micro plates, (d) nano plates and (e) porous α-Fe_2O_3 samples.

5 K in zero field. At 5 K, $H = 100$ Oe field is applied and the M versus T data is recorded while warming the sample up to 300 K. The M versus T data measured in the ZFC and FC cycle clearly show the Morin transition, T_M, which demarcates the pure antiferromagnetic region of α-Fe_2O_3 from the weak ferromagnetic region. This Morin transition which usually occurs at a temperature of $\sim$ 260 K in bulk α-Fe_2O_3 is known to depend on many factors such as the shape and size, defects and the related strain effects [106–108]. Strain effects in the lattice parameters with the reduction of grain size is a fact which is common in nanoparticles [109, 110]. In particular, an expansion in the lattice

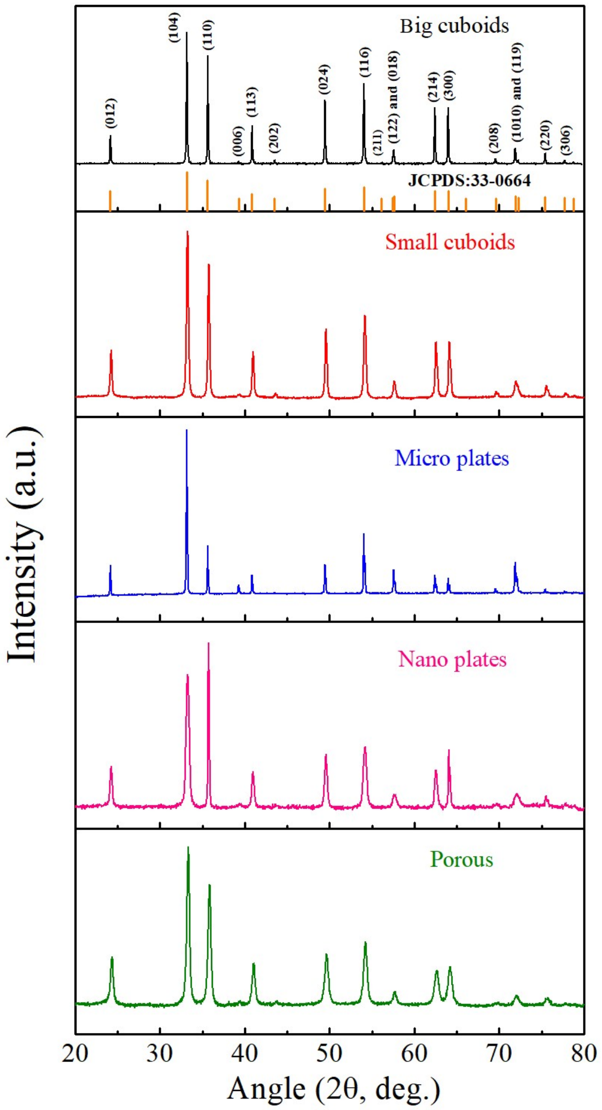

Figure 4.2 – Laboratory source based X-ray diffraction data recorded at room temperature for the cuboids, hex plates and porous α-Fe_2O_3 samples.

parameter with the reduction of grain size (or with the increase of S/V ratio) in many perovskites and corundum based oxides including α-Fe_2O_3 have been observed previously [111]. In addition, within a given morphology, anomalous strain effects can also result from the anisotropic growth of nanoparticles in a particular crystallographic direction. For instance, nano plates with thickness of ∼ 10 nm can be more strained in one specific direction. Thus the total strain effects in nanoparticles can be due to the combined effect of size and morphology factors. Overall, the strain effects arising due to these factors can modulate the number of uncompensated surface spins, bond angle and lengths and consequently magnetic interactions. For instance, a decrease in T_M with the decrease of grain size or with the increase of S/V ratio observed in the present α-Fe_2O_3 samples is shown in Fig. 4.3 (c). The T_M of all the samples have been obtained here as the peak point of their dM/dT versus T curves. From Fig. 4.3 (c), it is apparent that the T_M of micro plates which is least strained (S/V ratio $\sim$ 0.008 nm^{-1}) is 225 K. The T_M is seen to decrease with the increase of S/V ratio or strain effects and reached a temperature value of 125 K in case of porous sample.

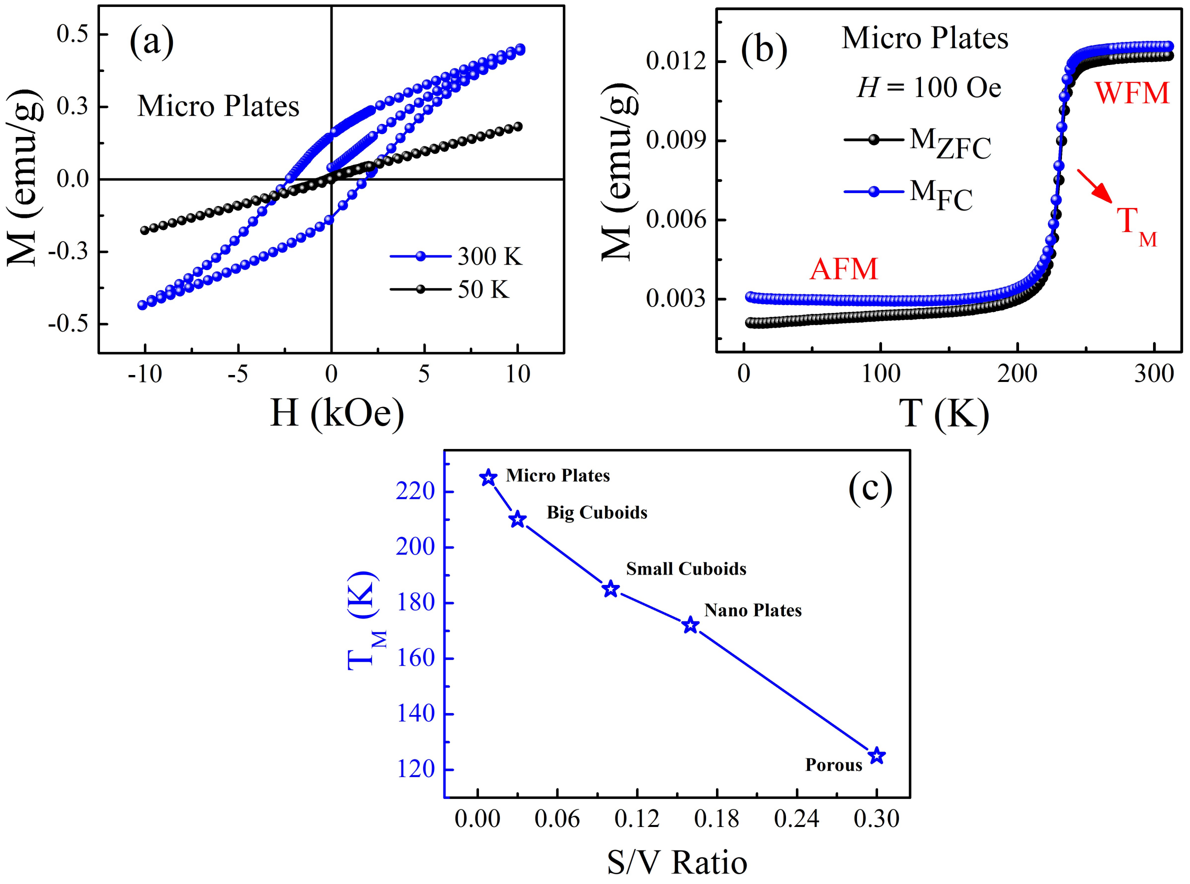

Figure 4.3 – (a) MH isotherm recorded at 300 K (WFM state) and at 50 K (in pure AFM state) for the micro plates. (b) M versus T curves recorded in the FC (blue dots) and ZFC (black dots) cycles for the micro plates. (c) Displays the decrease in Morin transition temperature as a function of increase in surface to volume ratio of the as synthesized α-Fe_2O_3 samples.

After some basic magnetic characterization for one representative hematite sample we next explore the M versus T and the corresponding μ versus T in all α-Fe$_2$O$_3$ samples of different shape size and morphology. The Morin transition being a first order spin reorientation transition is known to exhibit thermal hysteresis for the magnetization data recorded in the heating (ZFC) or cooling (FC) cycles. Considering this fact, in the present study we stick only to the FC cycles for the magnetization and remanent magnetization measurements. We first explore the key size effect on the acquisition of remanent magnetization for a given shape and morphology. Next we try to correlate the magnitude of remanence with the strain effects present in the lattice parameters. In this way, the remanent magnetization and the strain effects in the cuboid and plate shaped α-Fe$_2$O$_3$ samples are discussed separately. Finally we explore the behaviour of remanent magnetization in the porous α-Fe$_2$O$_3$ sample and compare the results with the cuboid and plate shaped samples.

4.2.3 Magnetization and remanence in cuboids of α-Fe$_2$O$_3$

The M_{FC} versus T data recorded for two different cuboids of α-Fe$_2$O$_3$ at different applied magnetic field H is presented in Fig. 4.4 (a)-(c). Here we note that, for the applied H of 100 Oe the magnitude of M_{FC} in the WFM region is significantly larger for small cuboids. With the increase of field, for H = 1 and 50 kOe, the magnitude of M_{FC} for both the cuboids are similar in the WFM region. In the AFM region, the magnitude of M_{FC} for both cuboids are similar for the applied H of 100 Oe and 1 kOe. However, for H = 50 kOe the magnitude of M_{FC} in the AFM region is significantly larger for small cuboids. This magnetization at low temperature and at higher applied H is due to the surface uncompensated spins which are usually present in the nanosized AFM materials [112, 113].

The μ_{FC} versus T data of the respective M_{FC} versus T runs recorded in the warming

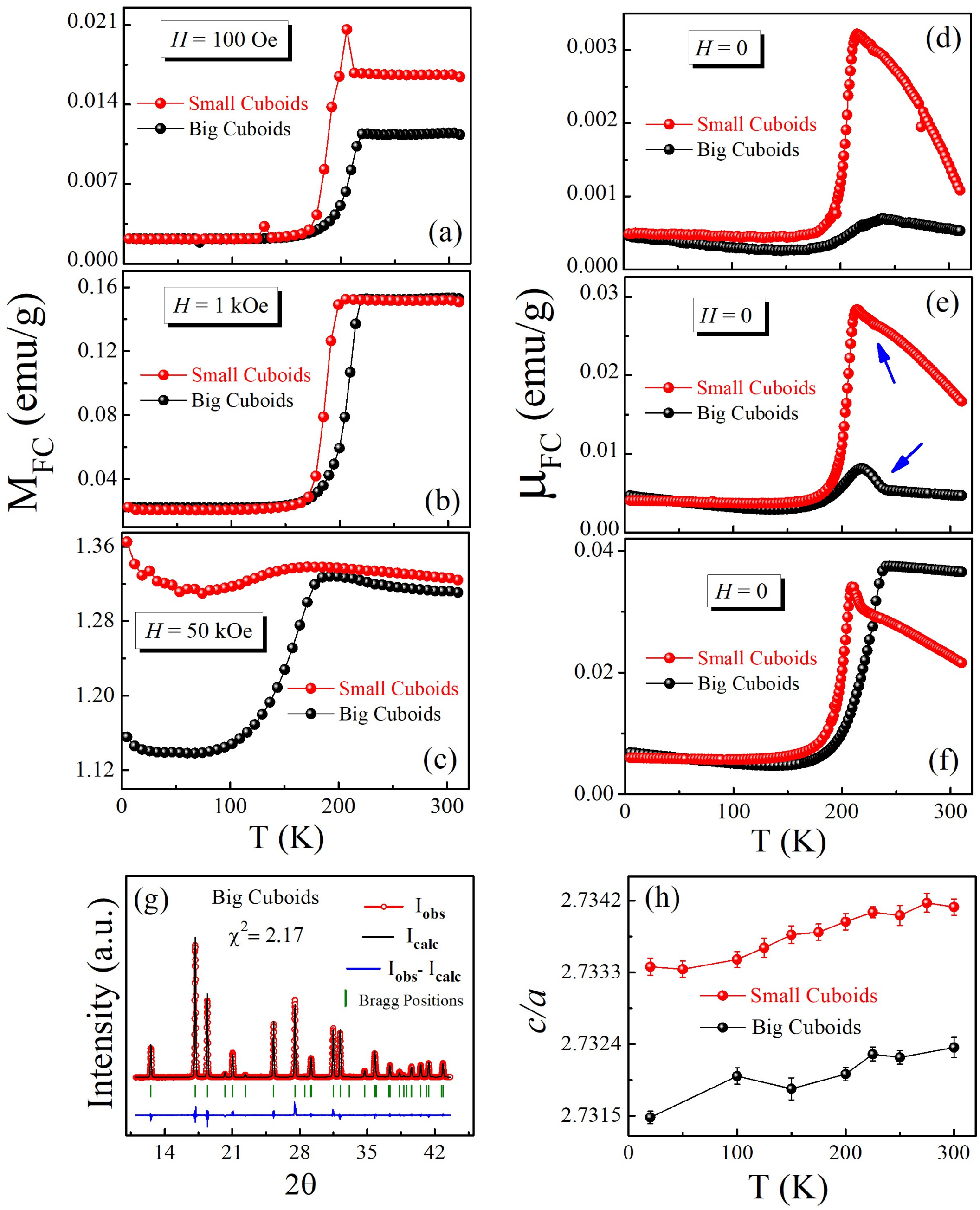

Figure 4.4 – M_{FC} versus T for big cuboids (black dots) and small cuboids (red dots) at different (cooling) H of (a) 100 Oe, (b) 1 kOe, (c) 50 kOe. (d)-(f) are the corresponding μ_{FC} versus T runs. (g) Representative synchrotron XRD data at 300 K with Rietveld fitting. (h) Compares the variation of c/a ratio with temperature in big and small cuboids.

cycle is presented in Fig. 4.4 (d)-(f). Here we observe that the magnitude of remanence in the WFM region is larger for the small cuboids particularly at 100 Oe and 1 kOe. At higher H of 50 kOe, the magnitude of remanence in the WFM region is relatively smaller for the small cuboids. The H dependence of remanence is discussed in more detail the later part of the text.

Below T_M, in the AFM region, the magnitude of remanence for both the cuboids is similar irrespective of the size effect and (cooling) H used for preparing the remanent state. Overall, the magnitude of remanence for both the cuboids is small in the AFM region compared to their respective values in the WFM region. These observations bring out the importance of DMI driven canted phase in the acquisition of remanent magnetization. The functional form of the μ_{FC} versus T for both the sample is similar below T_M where as above T_M, μ_{FC} decays relatively faster with T for the small cuboids. We also notice subtle anomalies (marked by arrows) in the μ_{FC} versus T curves in the WFM region for both the samples. These anomalies that are present in the μ_{FC} versus T data are however not prominent in the respective M versus T data. Thus remanence measurement appears to be more efficient tool to uncover the anomalies that are present in the WFM phase of α-Fe_2O_3. These anomalies appears to be connected to the DMI driven spin canting mechanism as discussed in the latter part of the text.

Synchroton XRD data fitted with Rietveld refinement for a representative cuboid sample is shown in Fig. 4.4 (g). The c/a ratio extracted from the Rietveld fitting of the synchrotron XRD data is given in Fig. 4.4 (h). Here we notice that for a given morphology the strain effects in the lattice parameter is larger for small cuboids. This observation is consistent with the increased magnitude of remanence and decreased value of T_M in small cuboids compared to the big cuboids.

4.2.4 Magnetization and remanence in hexagonal plates of α-Fe_2O_3

The M_{FC} versus T data recorded for micro and nano hex plates at different magnetic field is shown in Fig. 4.5 (a)-(c). The corresponding remanence data is shown in Fig. 4.5 (d)-(f). In hex plate morphology, the magnitude of M_{FC} in the WFM region for H

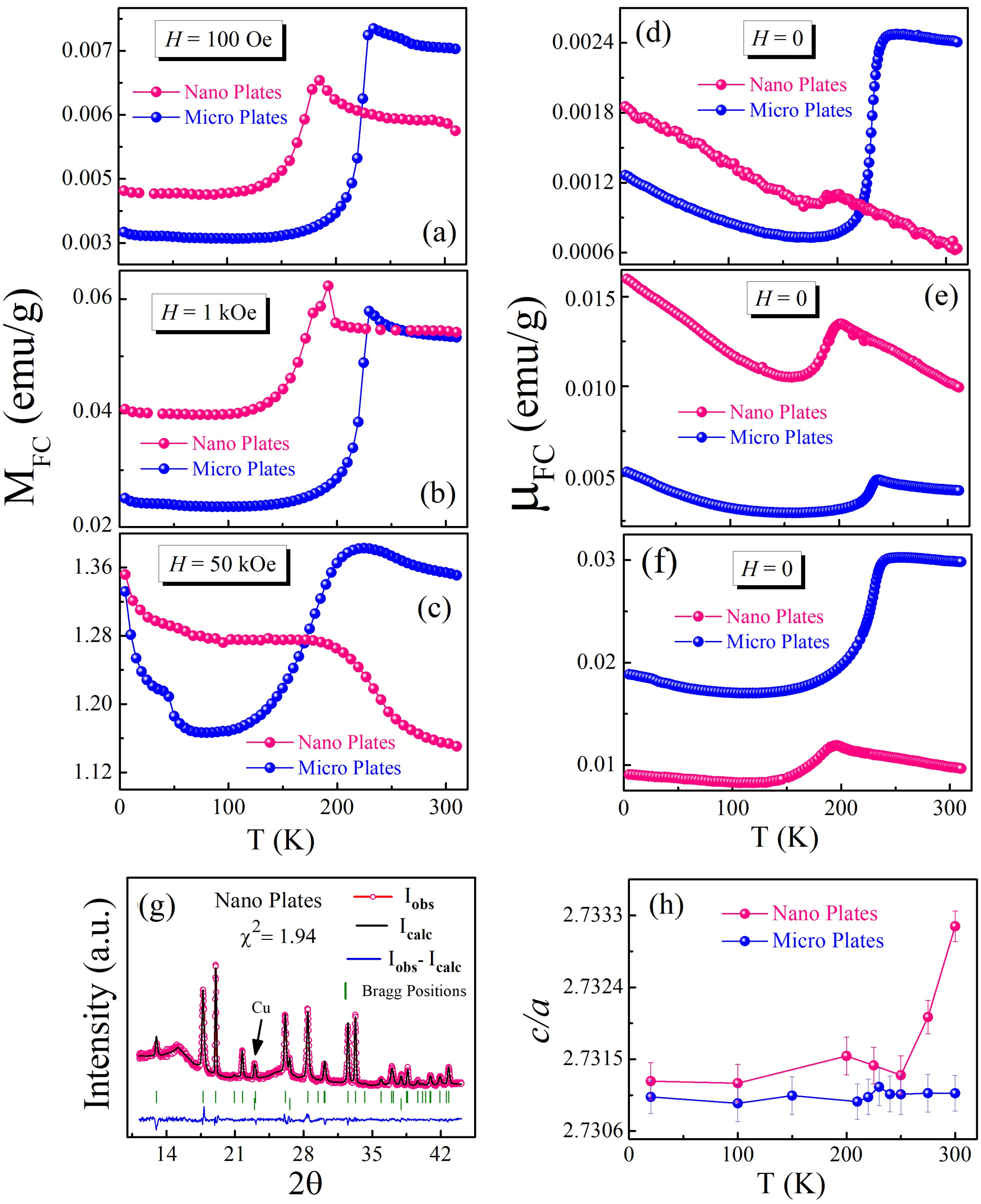

Figure 4.5 – M_{FC} versus T for micro plates (blue dots) and nano plates at different (cooling) H of (a) 100 Oe, (b) 1 kOe, (c) 50 kOe.(pink dots). (d)-(f) are the corresponding μ_{FC} versus T runs. (g) Representative synchrotron XRD data at 300 K with Le Bail fitting. (h) Compares the variation of c/a ratio with temperature in micro and nano plates.

= 100 Oe is small for nano plates. The magnetization increases with field and becomes similar in magnitude as that of micro plates at 1 kOe. With the further increase of field the magnitude of M_{FC} in WFM region is again smaller for nano plates. The reduced magnetization in the WFM region with the increase of S/V ratio can be expected for nano plates whose S/V ratio is two orders of magnitude higher as compared to the micro plates.

The magnitude of μ_{FC} is again larger for nano plates for $H = 1$ kOe, even though the corresponding M values for both the plates are of similar in magnitude. Similar to small cuboids, the magnitude of remanence for $H = 50$ kOe is also small for nano plates. The anomaly in the lattice parameters for both the samples obtained from the Rietveld refinement is presented in Fig. 4.5 (h). For hex plate morphology the anomaly in the lattice parameters is more prominent in the WFM region. Also in nano plates, the μ_{FC}, both above and below the Morin transition decreases relatively faster with T. This indicates upon down scaling the canting angle and the magnitude of remanence may be larger but the effect is relatively less robust as a function of temperature.

4.2.5 Magnetization and remanence in the porous α-Fe$_2$O$_3$

Black dots in Fig. 4.6 (a) represents the M_{FC} data recorded while cooling the sample in presence of $H = 1$ kOe. At 5 K the field is turned off to zero and the remanent magnetization μ_{FC} recorded while increasing the temperature is presented in the green dots. In case of porous sample the Morin transition is quite subdued. A slight hump at 125 K, more clearly can be seen from the μ_{FC} vs T data, marks the onset of Morin transition in the porous sample. From Fig. 4.6 (a) we see that, before turning off the H, the magnitude of M_{FC} at 5 K is $\sim$ 0.056 emu/g and after turning of the H the magnitude of μ_{FC} is $\sim$ 0.025 emu/g. We observe that this part of remanence remains fairly stable with time as long as the temperature held constant at 5 K. To clearly bring out this fact we check the stability of remanence as a function of time for the porous sample and compare that with a representative cuboid sample (Fig. 4.6 (b)). For the particular (cooling) H of 1 kOe, the percentage retainment of remanence in case of porous and big cuboids at 5 K are 50 and 18 % of their respective in-field M_{FC} value. The decay in remanence after the time period of 2 hours for the porous and big cuboids are < 1 and 3% respectively. Thus consistent with our previous observation on the carbonate samples, the remanence relaxation is case of α-Fe_2O_3 samples are ultraslow and leads to the observation of *time-stable* remanance.

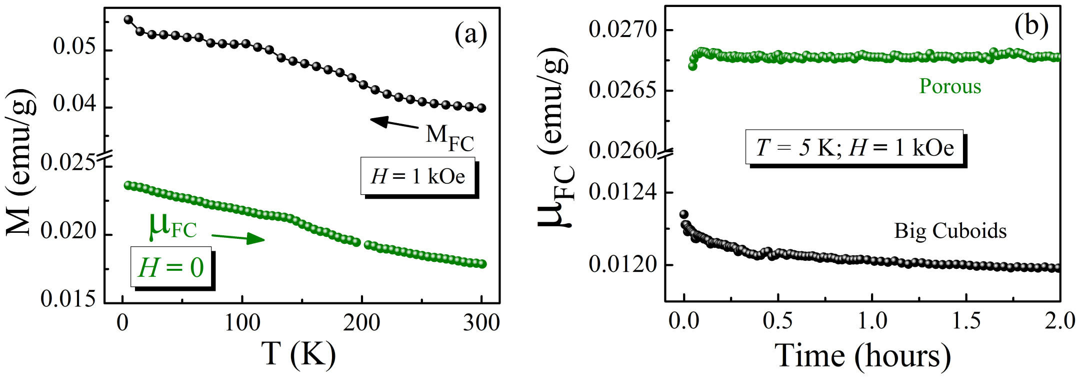

Figure 4.6 – (a) M_{FC} versus T (black dots) measured at $H = 1$ kOe and the corresponding μ_{FC} versus T (green dots) data, measured after removal of $H = 1$ kOe for the porous sample. (b) μ_{FC} as a function of time obtained for porous sample is compared with a representative cuboid sample.

To clearly bring out the effect of size and morphology in tuning the magnitude of this *time-stable* remanence, we finally grouped all the five α-Fe_2O_3 samples and discuss their remanent magnetization in the next subsection.

4.2.6 Remanence as a function of (cooling) *H*: cuboids, hexplates and the porous sample

In Fig. 4.7 (a)-(e) we compare the H dependence of M_{FC} (black dots) and the corresponding μ_{FC} (orange dots) for all five samples. Here the values of M_{FC} and μ_{FC} are picked up from the various M and the corresponding μ vs T runs. In all sample the M_{FC} as usual increases with the increase of H. The saturation magnetization, irrespective of morphology, are also similar in magnitude. However, the *time-stable* part of remanence

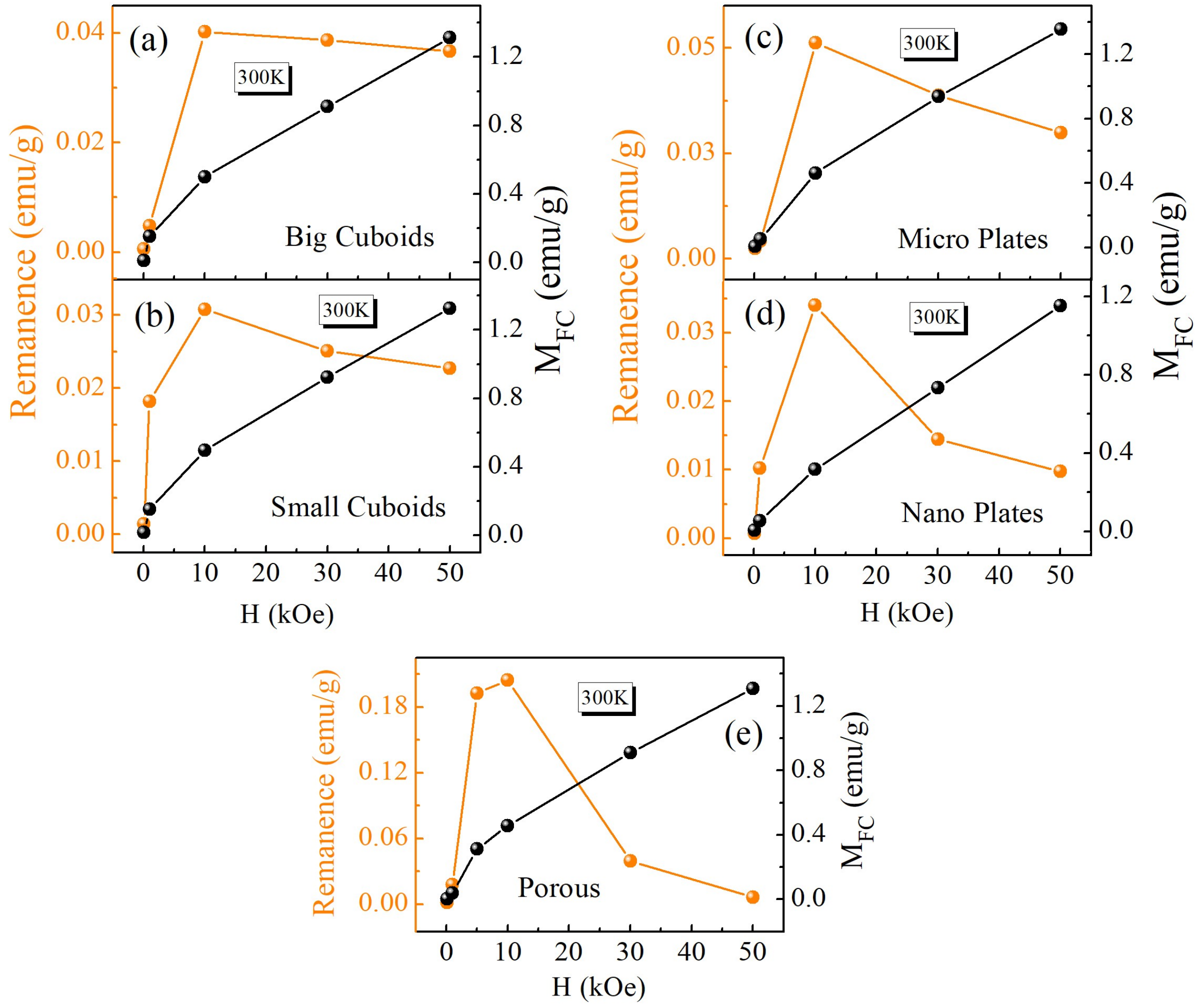

Figure 4.7 – (a)-(e) Depicts the M_{FC} versus H (black dots) and corresponding remanence versus H (orange dots) for α-Fe_2O_3 samples of different size and morphologies. These data points are extracted from various M_{FC} and the corresponding μ_{FC} vs T runs.

first increases with the increase of H, shows a maxima and then decreases with the further increase of H. Thus unlike M_{FC} versus H curve, the μ_{FC} versus H curve in all sample shows a peak like pattern. The magnitude of *time-stable* remanence is small for small as well as large values of H. There is an optimum critical H, at which the magnitude of the *time-stable* remanence attains the maximum value. This type of unusual variation of *time-stable* remanence with H is due to the phenomenon of weak ferromagnetism as observed previously in the carbonate samples.

From Fig. 4.7 it can also be noticed that, the magnitude of this *time-stable* part of remanence is ∼ 4-5 times higher in the porous sample as compared to other samples of different size and morphology. To clearly bring out this fact, we compare the magnitude of *time-stable* remanence of all the samples obtained at different (cooling) H in the AFM and WFM regions. From the grey rectangle regions as shown in Fig. 4.8, we note that, irrespective of the shape, size and morphology effects, the magnitude of remanence in the cuboids and plate shaped samples roughly lies in the range of ∼ 0.05 emu/g whereas the magnitude of remanence in case of porous sample is at least 4 times higher as compare to all other samples. It is to note here that the S/V ratio of the porous sample is higher than all other samples. Correspondingly the T_M of porous sample is lower than all other samples. Thus we see a correlation among the magnitude of remanence, S/V ratio and Morin transition. This is depicted clearly in Fig. 4.9.

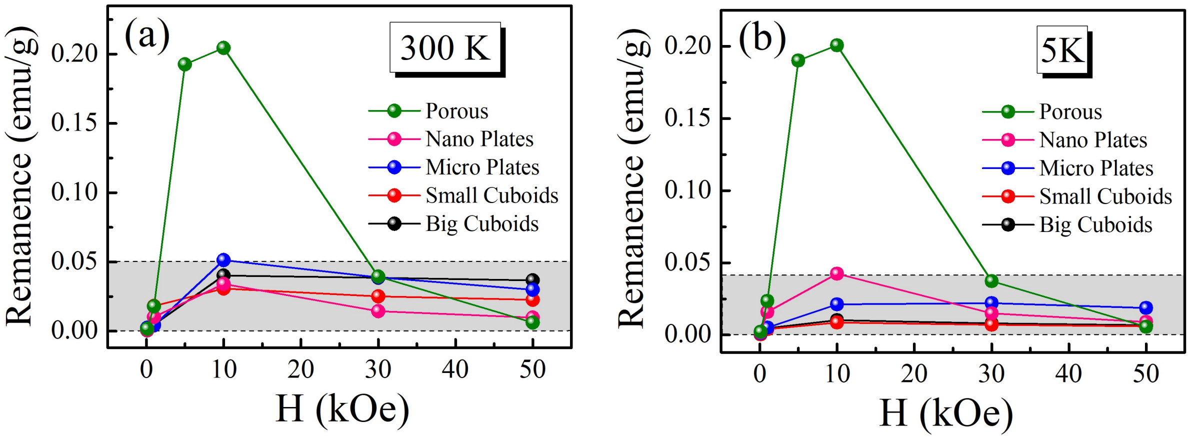

Figure 4.8 – The magnetic field dependence of remanence for all samples at (a) 300 K, (b) 5 K.

From Fig. 4.9 we see that with the increase of S/V ratio, a reduction in the T_M to around 125 K leads to four times increment in the remanence as observed in the porous sample. This fact can be understood in the following way. Though not shown explicitely here, the reduction in T_M implies the corresponding reduction in T_N. The reduction of T_N implies the weakening of basic antiferromagnetic interaction in α-Fe_2O_3 driven

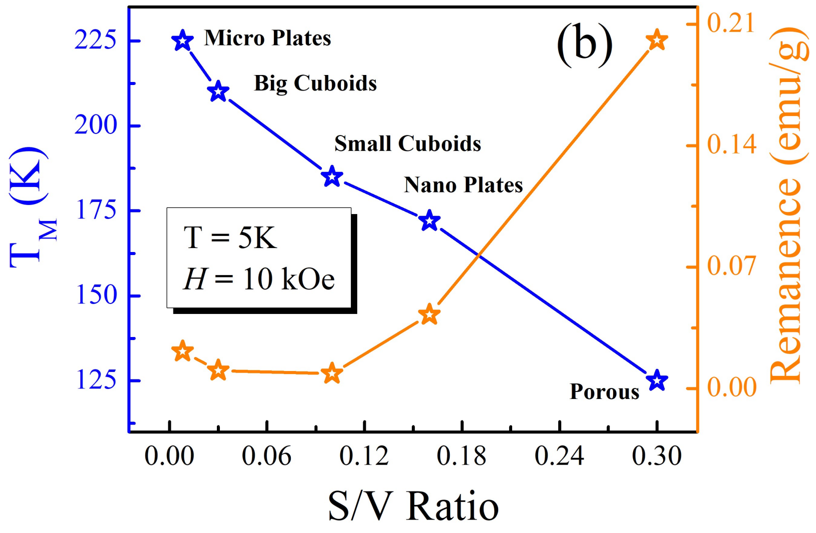

Figure 4.9 – The variation of the Morin transition temperature (left axis) and the peak value of remanence (right axis) as a function of the S/V ratio of the α-Fe_2O_3 samples.

by the superexchange interaction. This should lead to a larger spin canting angle and the associated weak ferromagnetism since the canting angle θ is propertional to the ratio D/J [4, 19]. A similar fact we have observed in the $MnCO_3$ and $NiCO_3$. Here the spin canting angle and consequently the magnitude of remanence is higher in $NiCO_3$ which has lower T_N compare to $MnCO_3$. Another fact which we would like to bring out here is the sharpness of the μ_{FC} versus H peaks. From Fig. 4.7 it can be noticed that the FWHM of the μ_{FC} versus H peak is sharper for the porous sample which has lower T_M and large magnitude of remanence. Comparing the FWHM of the porous sample with the $MnCO_3$/$NiCO_3$ we notice a further sharpening of μ_{FC} versus H peaks. These facts further clarifies that comparing the magnitude of *time-stable* remanence one can gauge the nature of spin canting and its extent in a weak ferromagnet.

As pointed out earlier, strain effects that are most commonly associated with the nanoscaling can significantly modulate the magnetic interactions. Strain effects in the lattice parameters can significantly alter the bond angle and bond length and in turn the variation in T_N, T_M and canting angle. Thus in the next step we investigate the strain effects and its impact on the exchange interaction pathways.

From the grey rectangle region as shown in Fig. 4.8 it is clear that the magnitude of *time-stable* remanence is significantly higher in the porous sample compared to the cuboids and plate shaped samples which have similar magnitude of remanence. Thus in order to keep the discussion incisive and contentful we choose big cuboid as a representative of α-Fe_2O_3 crystallites and compare it with porous sample for detail structural analysis.

4.2.7 Strain effects in lattice parameters and *time-stable* remanence

In Fig. 4.10 (a) the temperature variation of c/a ratio obtained for the porous sample is compared with the big cuboids. The lattice parameters are extracted from the Rietveld refinement of the synchrotron X-ray diffraction data. As expected the strain effect is significantly larger in the porous α-Fe_2O_3. To further understand the strain effects in the atomistic level we have analysed the electron density (ED) maps of big cuboid and porous sample. ED can be obtained from the inverse Fourier transformation of the structure factor given by [68, 114]

$$\rho(x, y, z) = \sum_{hkl} \frac{F_{hkl}.e^{-2\pi i(hx+ky+lz)}}{Z} \tag{4.1}$$

where ρ(x,y,z) is the electron scattering density; V is the unit cell volume; F_{hkl} is the structure factor; h, k, and l are the Miller indices.

The structure factor information is extracted from the Reitveld analysis of the synchrotron X-ray diffraction data. A slice of hexagonal unit cell of hematite in the xy plane we are interested for the ED analysis is shown in 4.10 (b). The orange and the grey balls corresponds to the Fe and O atoms respectively. The four corner Fe atoms lie on the same xy plane. The middle Fe atom lies little above the plane contaning the four corner Fe

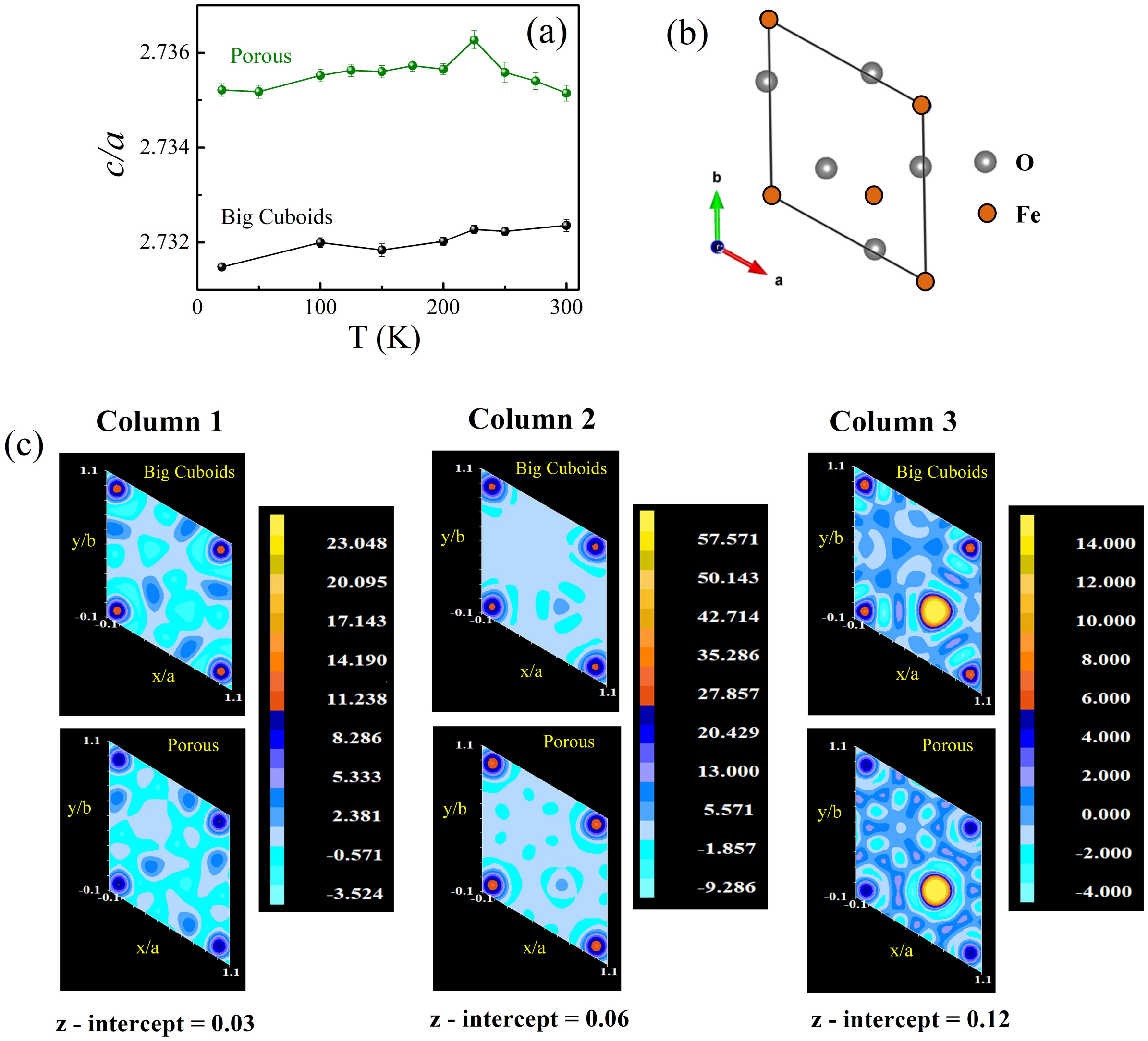

Figure 4.10 – (a) Temperature variation of c/a ratio compared between Big cuboids (black dots) and porous sample(green dots). (b) A slice of ab plane of the hexagonal unit cell generated using Vesta programme. (c) ED maps of the big cuboids (top panel) and porous sample (lower panel) obtained from the Fourier transformation of synchrotron XRD using Rietveld refinement.

atoms. There are four such layers of corner Fe atoms (two above and two below the center of inversion) that are present in a unit cell of hematite. Traversing in the z direction, the ED maps obtained at different z intercepts are shown in coulmn 1 to 3 (4.10 (c)). The scale bar corresponds to the ED of Fe and O atoms is shown adjacent to each column. For each column, the top and bottom panel displays ED map for the big cuboid and porous sample respectively.

In column-1 the ED maps of big cuboids and porous samples are compared for the z intercept of 0.03. At this intercept the first layer of four corner Fe atoms just start to appear. Here the ED around the corner Fe atoms is larger for the cuboid as (upper panel) compared to the porous sample (lower panel). At the z intercept of 0.06 (column-2), the ED around the corner Fe atoms in both the samples approaches their maxima. Here we notice that as compare to big cuboids the ED around the Fe atoms is more in the porous sample. Next in column-3 we compare the ED pattern at the z intercept of 0.12 where the four corner Fe atoms just start to disappear. Here we again notice that, similar to the z intercept of 0.03 (column-1), the ED around the corner Fe atoms is larger for the cuboid and is smaller for the porous sample. From the ED pattern of both sample it is apparent that unlike the case of porous sample where the ED around the Fe atoms is largely confined at the centres, where as the ED around the Fe atoms in the big cuboids is more uniformly distributed in the space. The ED maps thus pictorially represent the strain effects at the atomistic level, which are the consequence of nanoscaling. The strain effect microscopically related to the change in bond angle and bond length that profoundly affects the exchange interaction pathways and hence the variation in T_N and T_M.

The hexagonal unit cell of α-Fe_2O_3 is presented in Fig. 4.11 (a). Here grey balls represents the oxygen atoms. Blue and orange balls represents the layers of Fe atoms correspond to the up and down spins. There are four different superexchange paths between the Fe atoms of up and down spins through the intervening O atom [115]. Out of four superexchange paths, the dominant paths are the angles close to 131° and 120°. The temperature variation of these bond angles and the corresponding bond lengths between the Fe atoms is presented in Fig. 4.11 (b)-(e). Here the bond angle and bond length of the primary superexchange paths is larger for the porous sample implying the weakening of primary super exchange paths. This observation is consistent with the lowering of T_M

and larger magnitude of *time-stable* remanence as observed in the porous sample.

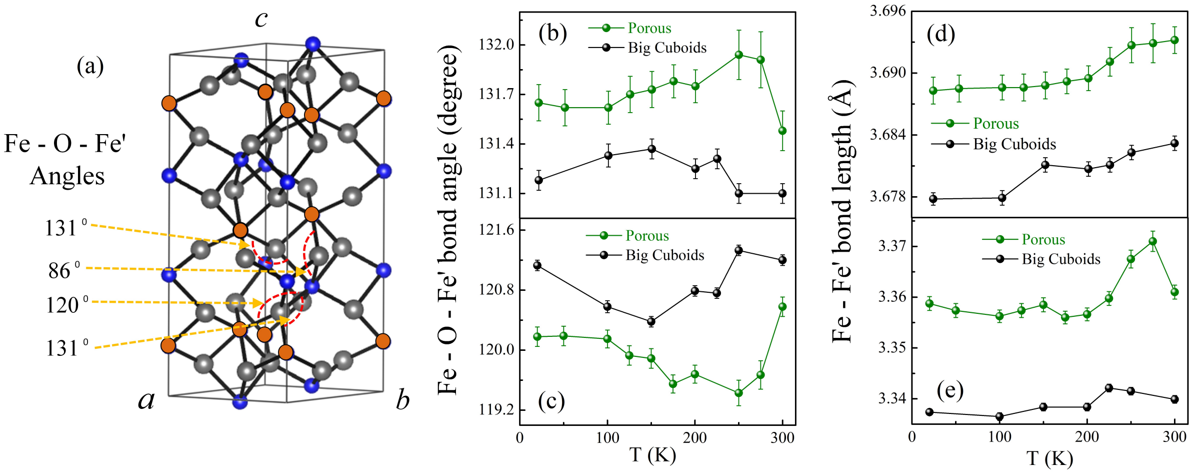

Figure 4.11 – (a) The hexagonal unit cell of hematite shown with the blue and orange balls representing the Fe atoms corresponding to up and down spins. The four different super exchange pathways and the corresponding bond angles are marked by the red curves. The temperature variation of bond angles (b, c) and bond lengths (d, e) governing the major superexchange pathways in big cuboids (black dots) and porous (green dots) hematite respectively.

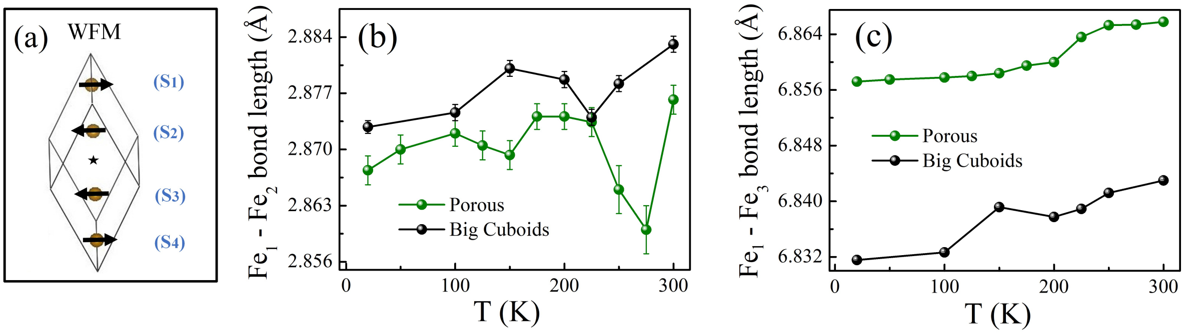

Figure 4.12 – Schematic of spin arrangement in the WFM region of the rhombohedral unit cell of α-Fe$_2$O$_3$. Temperature variation of bond length between the Fe atoms corresponding to the spin pairs (b) S$_1$ and S$_2$, (c) S$_1$ and S$_3$.

Another fact which we would like to point here is about the second Morin transition also referred to as dual Morin transition in α-Fe$_2$O$_3$. The presence of a small magnetic transition near the Morin transition have been observed earlier in different hematite nanostructures [116, 117]. In some of our samples especially in the cuboids we also observe a presence of second Morin transition in the μ_{FC} versus T curves (Fig. 4.4

(e) and (f)). The reason for this dual Morin transition is not yet fully understood. Samples containing mixture of two significantly different size distribution with different morphology may account for the presence of dual Morin transition. However, in our case the cuboid samples are fairly regular in shape with quite narrow size distribution as evident from their SEM images. Also a broad distribution of particle size will lead to broadening of Morin transition unlike the appearance of the second transition as observed in the present study. Since the presence of this dual Morin transition is evident only in the *time-stable* remanence, it appears that its origin is some way connected to the canted phase. Thus to understand the fact in detail we recall the primitive unit cell of hematite containing four Fe atoms as shown in Fig. 4.12 (a). These four Fe atoms are located along the [111] direction of rhombohedral unit cell considered by Dzyaloshinskii. In Fig. 4.12 (a) we schematically show spin configuration of the Fe atoms in WFM state with spins designated as S_1 to S_4. The spins lie almost perpendicular to the 111 direction consistent with symmetry considerations that give rise to finite net FM moment associated with DMI driven canting. Spin Pair S_1 and S_2 should be equivalent to spin pair S_3 and S_4 and correspond to the AFM planes above and below the inversion center. The associated DMI driven coupling should be $D_{12}.(S_1 \times S_2)$ and D_{34} (S_3 X S_4) respectively. Here D_{12} and D_{34} should be related such that the canting is consistent with symmetry considerations to give rise to a finite net FM moment associated with DMI driven canting as discussed in section 1.2. These adjacent AFM planes lies above and below the inversion center can be identified as the primary source of DMI coupling and the net FM moment. In Fig. 4.12 (b) we present the variations in the bond length as a function of temperature corresponding to the spin pairs S_1 and S_2. This exhibits anomalous features, especially two broad humps for both the samples. Looking into the anomalous features in the temperature variation of bond length corresponding to spin pair S_1 and S_2, we also present the bond length corresponding to spin pair S_1 and S_3. The spin pair S_1 and S_3 (which should be equivalent to S_2 and S_4) can be identified as the secondary source of DMI coupling. The corresponding bond length between the spin pair S_1 and S_3 also shows a change of slope as a function of temperature (Fig. 4.11 (c)). Though more careful microscopic measurements are needed to confirm this, but we propose that this secondary DMI driven coupling should also be taken into account. Especially the temperature dependence of individual AFM coupled spin pairs needs to be explored more carefully, looking into the anomalous strain effects in the lattice parameters, as observednhere. Overall, temperature variation of remanence and crystallographic data on the powders of these crystallites may not be sufficient, but still suggestive of this possibility. This may enable one to understand the double transition such as seen in case of cuboids in Fig. 4.4 (e) and (f) .

4.3 Exploring *time-stable* remanence in a single crystal of α-Fe_2O_3

So far we observe that in rhombohedral WFMs such as in carbonates and α-Fe_2O_3, a presence of unique remanence that remains almost stable with time. This *time-stable* remanence appears to be connected to the phenomenon of spin canting mechanism driven by DMI, the magnitude of which can be tuned upon down scaling. However, to further highlight that the features of remanent magnetization are intrinsic in nature it will be interesting to explore the remanent magnetization in a single crystal as well. Considering this fact, in the part-II of this chapter we present remanent magnetization investigation in a single crystal (SC). We use a SC of α-Fe_2O_3 for this purpose in which remanent magnetization can be probed both in the antiferromagnetic and weakly ferromagnetic regions. The SC used in the study has been grown using floating-zone technique in Prof. S W Cheong's lab, Rutgers University, USA.

4.3.1 Single crystal of α-Fe$_2$O$_3$: μ vs T

The magnetization data recorded while cooling the sample in presence of $H = 1$ kOe field applied parallel to the a-axis of the crystal is presented in Fig. 4.13 (a). The inset of the figure depicts the dimension of the crystal ($\sim 6 \times 4$ mm) used in the study. The Morin transition demarcating the pure AFM region of α-Fe$_2$O$_3$ from the WFM region occurs at a temperature of 260 K is clearly evident from the figure. After the typical M_{FC} measurement the magnetic field is turned off to zero and the remanent magnetization data recorded in the warming cycle is shown in Fig. 4.13 (b).

Here we observe that the sign of remanence does not commensurate with the sign of H applied for preparing the remanence state. From a number of μ_{FC} vs T data we note that the sign of remanence in the WFM region remains primarily negative and its magnitude shows a slight decreasing trend with the increasing magnetic fields (inset in Fig. 4.13 (b)). It is to be noted that for preparing the remanence state in α-Fe$_2$O$_3$ the magnetic field is applied at 300 K where the system is already in the WFM state. This is unlike the case with weakly ferromagnetic carbonates, where remanent state can be prepared with the magnetic field applied in the paramagnetic state far above their WFM state. In the same system we also have noticed that, once the spontaneously canted domains frozen from the AFM state to the WFM state in presence of a positive guiding magnetic field, it is hard to change the sign of magnetization if the sign of H reversed in the WFM state. Thus for obtaining the remanence data unambiguously such as observed in the carbonate sample, it is preferable to apply the H in the paramagnetic region in α-Fe$_2$O$_3$. However the T_N of α-Fe$_2$O$_3$ $\sim$ 960 K, and practically it is not feasible to cool the sample each time above 960 K for preparing the remanent state. Irrespective of the ambiguity related to the sign of remanence, from the present data we note that the magnitude of the remanence is substantial only in the WFM region. With this our next endeavour is to check the stability of this remanence both in the WFM and AFM region of the SC.

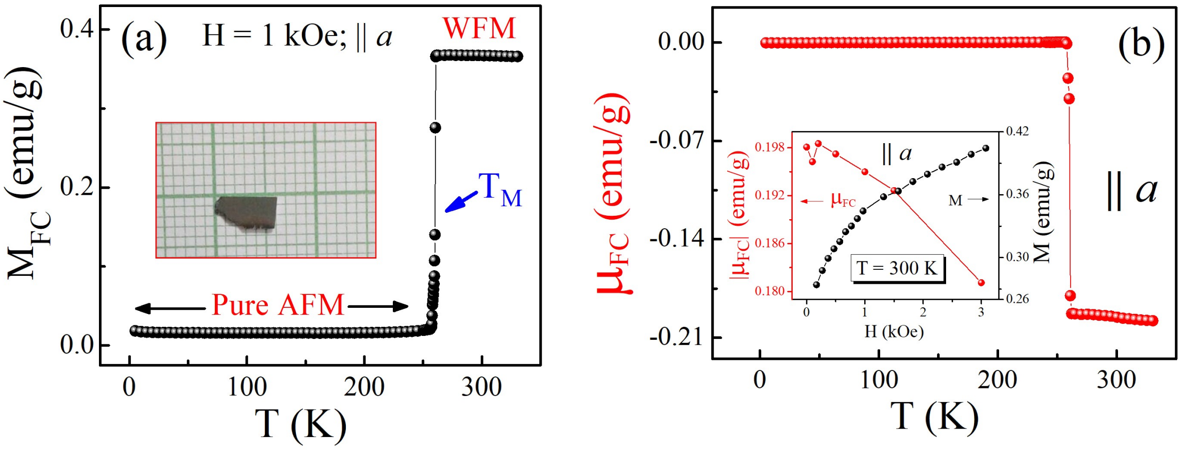

Figure 4.13 – (a) M_{FC} versuss T measured parallel to the a axis of the single crystal of α-Fe$_2$O$_3$. The Morin transition occurs at a temperature of $\sim$ 260 K is marked with a blue arrow in the figure. The inset shows the picture of the single crystal used in the study. (b) μ_{FC} versus T run corresponding to the M_{FC} versus T run. Here the remanence is vanishingly small in the pure AFM region and finite in the WFM region. The inset shows the μ_{FC} obtained at 300 K parallel a axis as a function of various (cooling) H.

4.3.2 Single crystal of α-Fe$_2$O$_3$: μ vs *time*

Since the magnitude of remanence is substantial in the WFM region, we first check the stability of remanence in the WFM region. Similar to the FC measurement protocol, we follow a ZFC measurement protocol for preparing the remanent state in the weakly ferromagnetic region. In this protocol the single crystal was heated in presence of a guiding magnetic field from below its T_M upto 300 K. At 300 K the field is removed and the remanent magnetization (denoted as μ_{ZFC}) is measured as a function of time. Following this protocol the magnetization relaxation process is checked both along the a and c axis of the SC (main panel of Fig. 4.14). Here we first note that the remanent magnetization relaxation is ultraslow in nature irrespective of the direction of H. Next the magnitude of remanence in the WFM region is slightly higher along the a-axis. Though the difference is small, this is due to the weakly ferromagnetic nature of α-Fe$_2$O$_3$ which

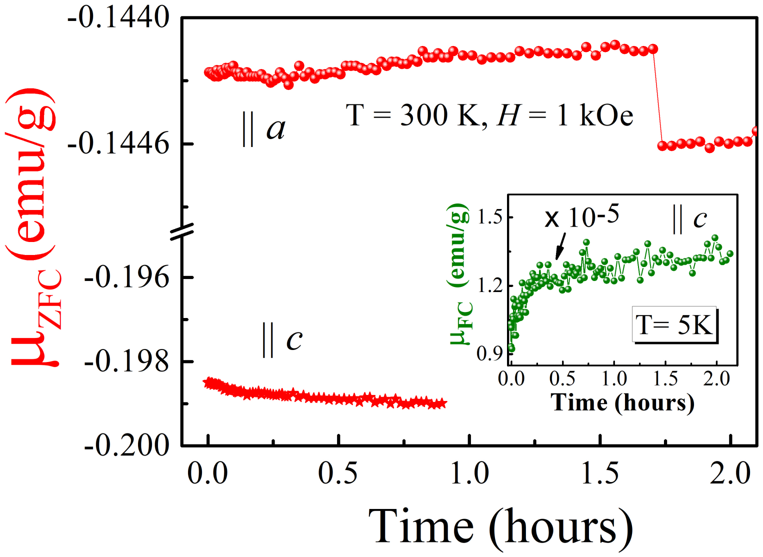

Figure 4.14 – Main panel displays remanence as a function of time at 300 K for a (cooling) H of 1 kOe measured parallel to a and c axes. The inset displays the same measured at 5 K parallel to c-axis of the single crystal.

has a large in plane component and a slight out of plane component (see Appendix-1 for detail). The variation of remanent magnetization with time measured in the AFM region following the FC protocol is presented in the inset of the figure. Here the sign of remanence is positive, however, its magnitude is negligibly small as is expected. This data further suggests that heating and cooling protocols play an important role to control the magnitude of *time-stable* remanence in α-Fe$_2$O$_3$. Heating in presence of H below T_M would enable larger number of weak ferromagnetic domains to orient in the direction of H and hence decides the magnitude of remanence as seen in the present case.

Overall the data presented in Figs. 4.13 and 4.14 clearly brings out the unusual features of remanent magnetization that are not perceptible from the routine M versus T and M versus H measurements. It is also to note that α-Fe$_2$O$_3$ is not a frustrated AFM. Furthermore observation of ultraslow magnetization relaxation in the defect free SC of α-Fe$_2$O$_3$ firmly excludes any possibility of any size and interface related effects that can result in slow magnetization relaxation. Thus from the presence of *time-stable* remanence observed in a variety of weak ferromagnetic carbonates including the present case of the SC α-Fe_2O_3 it can be concluded that the ultraslow relaxation of magnetization dynamic is a ramification of the phenomenon of DMI driven spin canting mechanism present in such systems.

It is to note that the ambiguity related to the sign of remanence that we observe in the SC of α-Fe_2O_3 has also been observed in the sign of stress induced moments in some weakferromagnets/piezomagnets on repeated cooling [27, 105]. Also it is observed that, magnetization reversal in PzMs require the reversal of weakly ferromagnetic domains and such process is energetically unfavourable. We see that in our remanence measurements on varities of WFMs this phenomenon is reflected in the form of *time-stable* remanence. This observation further demonstrates the intimate connection between weak ferromagnetism and piezomagnetism which can better be tracked through remanence measurement than the routine M versus H or M versus T measuements.

4.4 Conclusion

To summarize, we have explored remanent magnetization in a series of α-Fe_2O_3 samples of different size and morphologies synthesized by the hydrothermal method. In all the samples we observe a part remanence that is *time-stable* in nature and it appears to be connected with the DMI driven spin canting phenomenon. The *time-stable* remanence shows a unusual dependence with the (cooling) H, the magnitude of which is maximum for an optimum (cooling) H used to prepare the remanent state. We observe that the magnitude of this *time-stable* remanence can significantly be tuned with nanoscaling. The ED maps and the temperature variation of lattice parameters, bond angle and bond length determined from the synchrotron XRD data brings out the anomalous strain effects associated with the nanoscaling, which plays a significant role in tuning the magnitude of remanence. The temperature variation of remanence data and structural parameters reveals a clear correlation between the Morin transition, extent of spin canting and the magnitude of *time-stable* remanence. Further to this, the *time-stable* character of remanence is also explored in a SC of α-Fe_2O_3 as well. Observation of *time-stable* remanence in a varieties of α-Fe_2O_3 samples including the single crystal enables us to generalize that its origin is intrinsic, solely connected to the phenomenon of spin canting mechanism driven by the DMI. The presence of *time-stable* remanence can be exploited in the next generation of antiferromagnetic spintronics device applications where such WFMs/PzMs can be used as pinning layer at the FM/AFM interfaces. Finally remanence measurement is proven to be an efficient tool to capture the essential physics of DMI driven spin canting mechanism better than the routine M versus T or M versus H measurements.

Chapter 5

Time-stable remanence in DMI driven weak ferromagnets: scaling analysis & microscopic evidence

5.1 Introduction

In this chapter we first present a scaling analysis pertaining to the time stable remanence in carbonates. For this purpose, we have explored all three WFM carbonates including $MnCO_3$, $NiCO_3$ and $CoCO_3$. The presence of *time-stable* remanence and its qualitative and quantitative features are compared in conjunction with their respective Néel temperatures. Further to this, we present a plausible microscopic reason for the observation of *time-stable* remanence in all these DMI driven compounds included in our study. Finally we present a microscopic experimental evidence for the presence of *time-stable* remanence which is obtained through the neutron diffraction mesurement performed on the remanent state of a representative weak feromagnetic sample $CoCO_3$.

5.2 Universal scaling behaviour of remanent magnetization

It has been observed that the remanence data of the nano structured Cr_2O_3 systems obtained at different cooling field H when normalized with a fixed reference temperature T_r less than T_N of the sample shows a universal scaling behaviour [51, 52]. It is an interesting question to ask whether such a scaling behaviour of the remanence is particular only to the nano structured Cr_2O_3 systems or is a general phenomenon likely to arise in other WFM/PzM systems.

We consider remanence as a function of temperature, obtained in different (cooling) H for all three carbonates. These data are shown in Figs. 5.1 (a)-(c). As evident from Fig. 5.1 (a) and (b) both in $MnCO_3$ and $NiCO_3$, the remanent magnetiztion increases with the cooling H, attains a maximum at some particular H and and it vanishes with with the further increase in (cooling) H. The peak like behavior of the remanence with (cooling) H was also shown in chapter 3 (Figs. 3.3 (e) and 3.6 (c))for $MnCO_3$ and $NiCO_3$. However, the remanent magnetization in $CoCO_3$ is seen not to vanish with the (cooling) H. Rather the remanence data obtained at different cooling H ranging from 50 Oe - 50 kOe shows a mild variation with H (Fig. 5.1 (c)).

Interestingly we observe that each remanence curve obtained at different cooling H, when normalized with the value of μ_{FC} at a fixed reference temperature $T_r < T_N$, becomes indistinguishable. The curves obtained at different cooling H, merge to form a single universal curve. The universal curve obtained for a particular T_r of 10 K is presented in Figs. 5.1 (d)-(f). These data show that the ratio $\frac{\mu_{FC}(H,T)}{\mu_{FC}(H,T_r)}$, where T_r is the reference temperature, is independent of the applied magnetic field and is simply a function of temperature. As mentioned before, similar scaling has been observed in ultra-thin films of Cr_2O_3 [51]. Here it was pointed out that the remanent magnetization factorizes in the two variables, namely, μ_{FC} (H,T) = f(H) g(T) so that

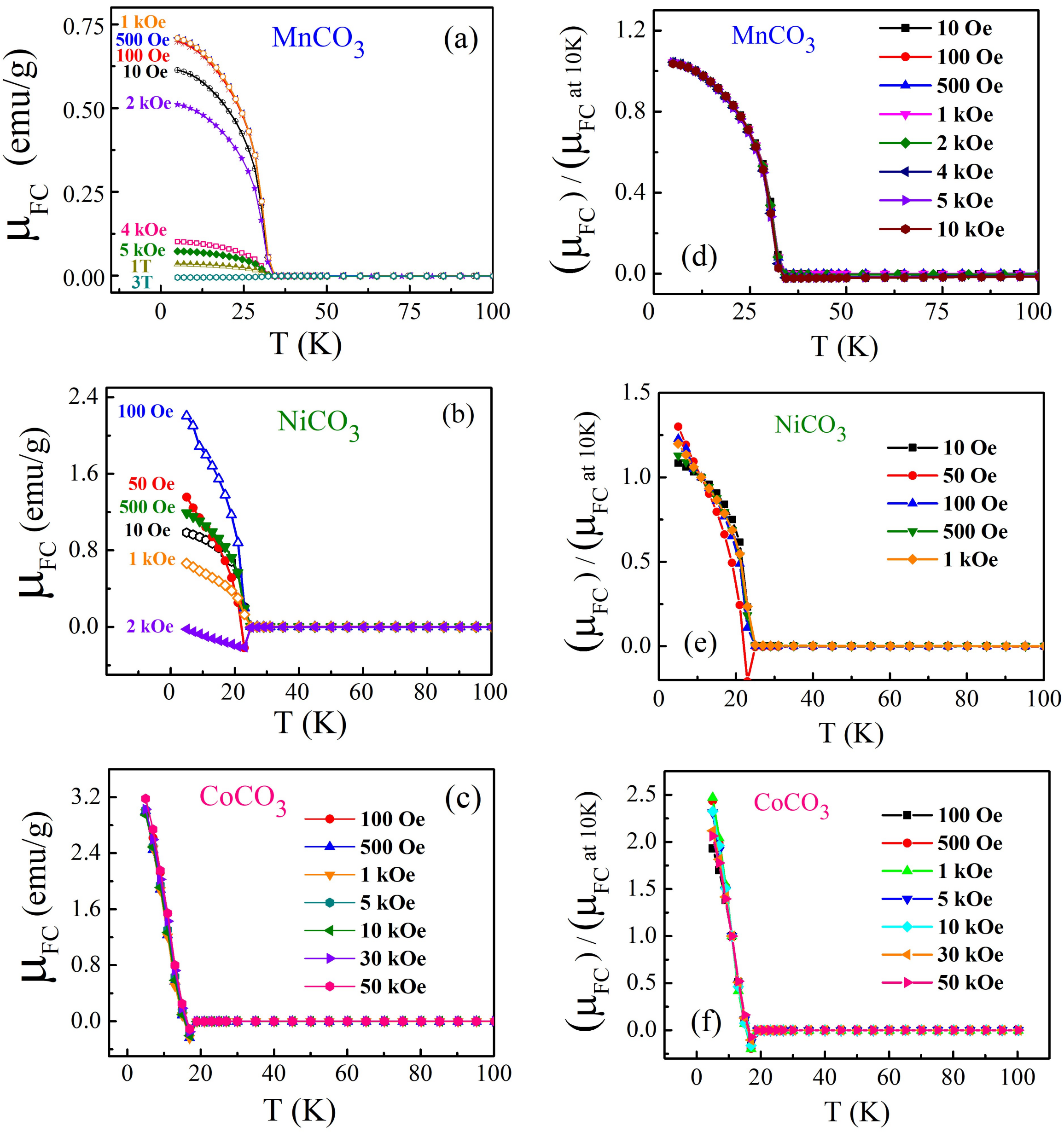

Figure 5.1 – M_{FC} versus T at different cooling H in (a) $MnCO_3$, (b) $NiCO_3$, (c) $CoCO_3$. (d)-(f) depicts the scaling behaviour of remanence for all samples obtained for a fixed T_r of 10 K.

$$\frac{\mu_{FC}(H,T)}{\mu_{FC}(H,T_r)} = \frac{f(H)g(T)}{f(H)g(T_r)} = \frac{g(T)}{g(T_r)} = G(T,T_r) \tag{5.1}$$

Thus normalization of each remanence curve at a fixed T_r removes the field dependency and, as a result, all the curves merge to give a single universal curve. These features were associated with foot prints of piezomagnetism, which although is not a symmetry allowed phenomenon for bulk Cr_2O_3 but understood to arise from strain effects [51].

Coming back to the carbonates presented in Fig. 5.1, which are symmetry allowed WFM/PzM we find perfect scaling in the entire temperature window below T_N. In case of $NiCO_3$, slight deviation from the perfect scaling is observed in the temperature window of 5-10 K (Fig. 5.1 (e)). $CoCO_3$, on the other hand exhibits a very different pattern. Here the data exhibit very mild variations with (cooling) H and appears to be self scaled (Fig. 5.1 (c)). Here again, dividing by a remanence at a fixed ref temperature leads to a master curve, with mild deviation. Overall we can say that all three carbonates do show the signatures of scaling behaviour, which were associated with the strain driven piezomagnetic traits [51, 52]. Thus we see another important characteristic of WFMs whose remanent magnetization can be factorizable once pinned through a field cooling process in a guiding H. This universal scaling behaviour could not be observed in α-Fe_2O_3. The reason could be related to the preparation of the remanence state in α-Fe_2O_3 where cooling of the sample from above its Néel temperature, $T_N \sim 950$ K, is practically not feasible for the fresh remanent state each time.

Interestingly, we found a clear correlation between the Néel temperature and the magnitude of remanence in all WFMs. To clearly bring out this fact, we have plotted the maximum magnitude of *time-stable* remanence obtained in all the samples in conjunction with their respective T_N values in Fig 5.2. We observe an inverse correlation between the maximum magnitude of remanence and the T_N of respective samples which tells that maximum pinning of remanent magnetization can be obtained for the samples with lower T_N. WFMs with low T_N are also known to be strong WFMs. For instance, $NiCO_3$ with $T_N \sim 24$ K is reported to be strong weak ferromagnet with larger spin canting angle than

$MnCO_3$ ($T_N \sim 32$ K) and α-Fe_2O_3 ($T_N \sim 950$ K). Therefore, comparing the magnitudes of the remanences in different systems gives an idea of the extent of spin canting angles present in the systems. The actual estimation, in general, is a nontrivial task. The case of $CoCO_3$ (denoted with the star mark), however, appears to be different. The maximum magnitude of remanence in $CoCO_3$ is larger than $NiCO_3$ and this is in contradiction with its spin canting angle which has been estimated (both experimentally and theoretically) to be less than that of $NiCO_3$. It is also to be noted that, in the same compound, the presence of single ion anisotropy is comparatively larger.

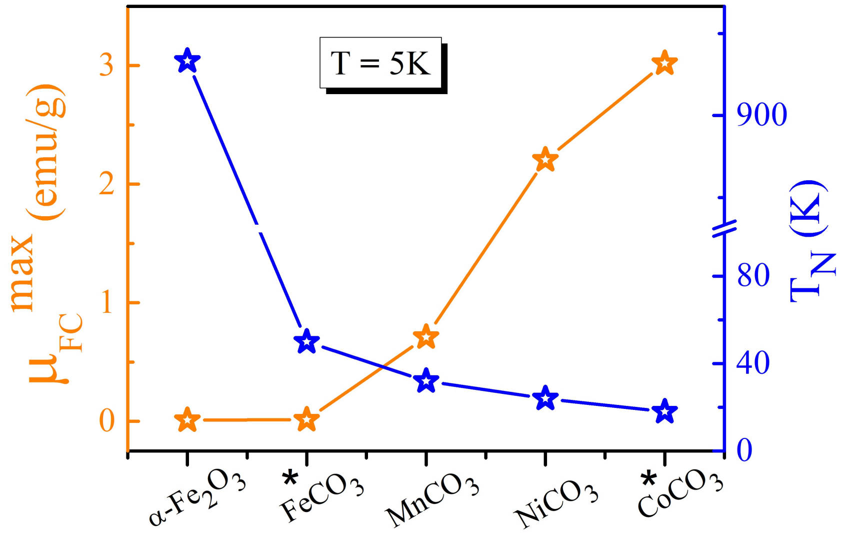

Figure 5.2 – The maximum magnitude of remanence showing inverse relation with the T_N of respective samples.

At this point, it is also interesting to compare the qualitative features of *time-stable* remanence in all the symmetry allowed WFM including carbonates and hematite. These data are shown in Fig. 5.3. The remanence data of all samples have been normalized here with their respective initial values at t=0. It is evident that the remanent magnetization in $MnCO_3$ and α-Fe_2O_3 is almost stable with time. The remanent magnetization in other samples are relatively less stable. Bulk $FeCO_3$ is reported not to be a symmetry allowed WFM. The weak ferromagnetism in $CoCO_3$, in addition to DMI, is also governed by SIA.

Remanent magnetization in such cases needs further investigation. Nevertheless, with all these subtleties, from our present study of remanent magnetization, we qualitatively see the presence of a *time-stable* remanence in all the WFMs. This *time-stable* remanence is associated with a robust magnetization pinning mechanism which appears to be larger in $MnCO_3$ and in α-Fe_2O_3. we finally present a plausible mechanism of the origin of this robust magnetization pinning process that leads to the observation of *time-stable* remanence in all the WFMs.

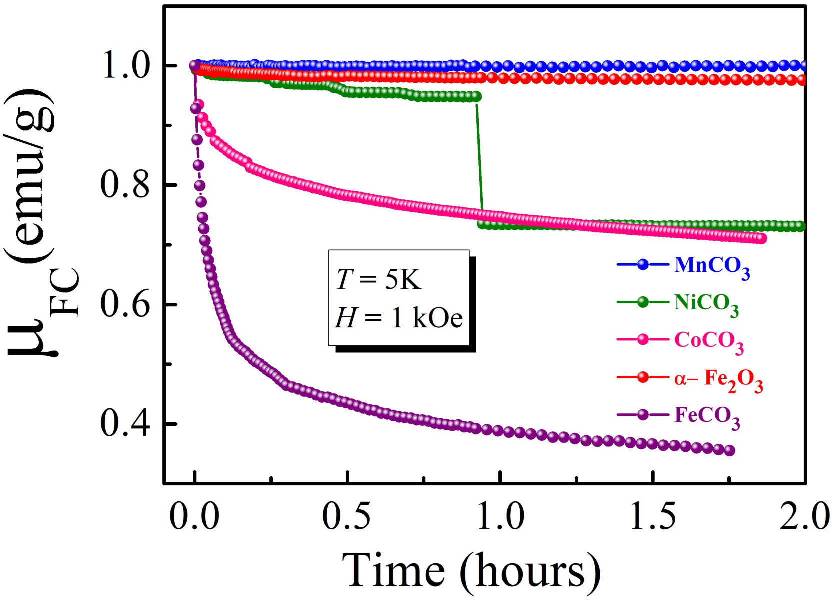

Figure 5.3 – Comparison of the variation of remanence as a function of time in all the WFMs. Remanence relaxation of the symmetry restricted weak ferromagnetic carbobnate sample $FeCO_3$ has also been included for consistency.

5.2.0.1 Robust magnetization pinning: connection with weak ferromagnetism

In order to understand the microscopic mechanism responsible for the ultraslow magnetization relaxation, we recall the detailed magnetic structure that governs the magnetization process in the WFMs under the study. The unit cell of WFMs, which we study, is hexagonal. The unit cell can also be represented in a rhombohedral primitive structure with the c-axis of the hexagon as the body diagonal of rhombohedron as shown

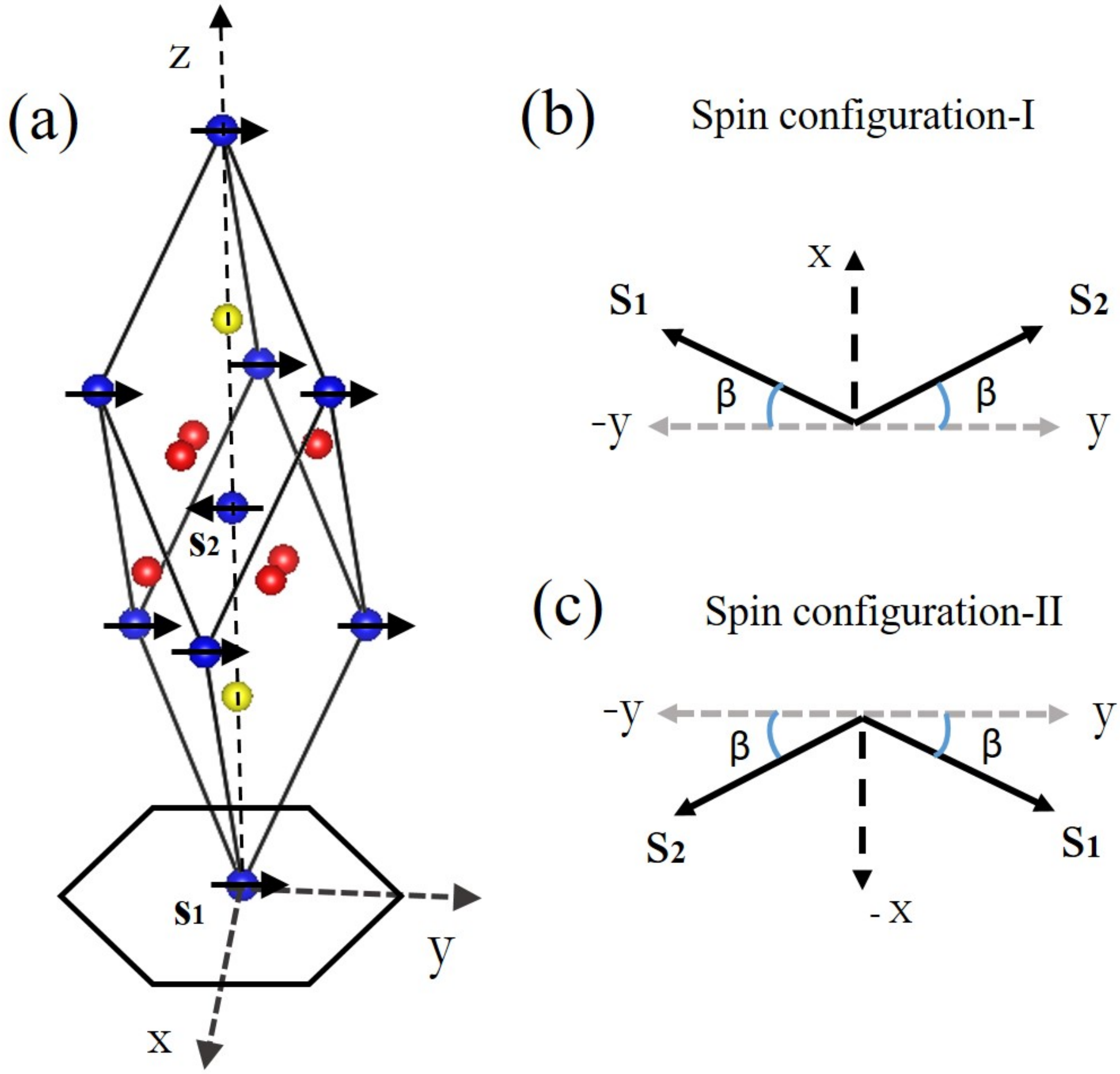

Figure 5.4 – (a) The rhombohedral unit cell of MCO_3 with 111 axis along the z-direction as the c-axis of the hexagon. The unit cell contains two magnetic atoms with spins S_1 and S_2 coupled antiferromafnetically as shown in the figure. The blue, red and yellow balls correspond to the transition metal, oxygen and carbon atoms. (b) and (c) schematic of the canted spin configurations within the basal plane in MCO_3. Canting of the spins towards z-axis is out of the plane of the paper.

in the Fig. 5.4 (a). For tha sake of simplicity we will focus on the primitive unit cell of MCO_3 which contains two magnetic atoms with spins coupled antiferromagnetically denoted as S_1 and S_2 in the Fig. 5.4 (a). Below T_N the antiferromagnetic spin arrangement is not perfect. Rather the antiferromagnetic spins lying almost in the (111) plane of the rhombohedron (equivalently basal plane in the hexagonal setting) are slightly canted towards the [111] axis (equivalently c-axis of hexagon). In addition, the spins are also canted towards each other within the (111) plane (hexagonal basal plane). Such a spin arrangement as pointed out by Dzyaloshinskii and Borovik-Romanov generates a weak ferromagnetic moment in these systems directed along a two-fold axis [18, 118–120]. If we assign the Cartesian coordinate x-axis along the two-fold axis and z-axis along the three-fold [111] axis (or c-axis) then the antiferromagnetic spin configuration that generates the weak ferromagnetic moment along the two-fold axis is depicted in Fig. 5.4 (b). Here the spins are canted through an angle β towards each other. The small canting of the spins towards the c-axis is out of the plane of the paper in the figure. Such a spin configuration should also control the possible ways of AFM domains that can exist in the WFM region. It is to note that, the phenomenological theory of Dzyaloshinskii for spin configuration also predicts a small weak ferromagnetic component along the c-axis of the unit cell (see Appendix-1, for the detail spin configuration and the direction of net moment). However, as observed experimentally by Flanders, the magnitude of this out of plane component (c-axis component) is very small compared to the large in-plane or basal plane component [121].

Now coming back to the spin configuration as shown in Fig. 5.4 (b), we note that the spins S_1 and S_2 are predominantly in an antiferromagnetic configuration (along y axis) produced by the strong superexchange interaction ($-J\ S_1.S_2$) and canted slightly (towards the x-axis) by the weak Dzyaloshinskii-Moriya interaction ($D.(S_1 \times S_2)$). However, the two interactions are invariant under $S_1 \rightarrow -S_1$ and $S_2 \rightarrow -S_2$ (spin reflection symmetry, see Appendix-1) and, therefore, a configuration such as depicted in Fig. 5.4 (c) is also thermodynamically (energetically) favourable. Here the second configuration can be thought of as being obtained from configuration depicted in Fig. 5.4 (b) by reversing S_1 and S_2 by π, anti-clockwise (or clock wise) around the z-axis. However, these two states are largely separated by an energy barrier. A simple way of visualizing this is through the double well potential (see Appendix-1 for technical details) with the two spin configurations identified as the ground states (minima) of the double well potential as shown in Fig. 5.5. The two ground states cannot classically convert into each other without climbing over the potential barrier between them. Therefore, mixing of these two states, which has to be accompanied by the reversal of antiferromagnetic sublattices, is energetically unfavourable. When we subject the system to a magnetic field H, the induced magnetization, in addition to the usual contributions from the Zeeman energy and magnetocrystalline anisotropy, will have contributions from the spontaneously canted spins as depicted in Figs. 5.4 (b) and (c). Upon cooling the system in presence of H, one of the two given types of weakly ferromagnetic domains, with spin configurations discussed earlier, will grow in number depending on the direction of the field. When the field is removed, a reversal of the weakly ferromagnetic domains is not energetically favourable as we have already argued (see Appendix-1 for a detailed mathematical derivation). This robust magnetization pinning leads to the observation of *quasi-static/time-stable* remanence as observed in the series of carbonate samples. However, this feature is only effective upto a critical field value H_c, as these systems are predominantly antiferromagnet with the strength of isotropic exchange interaction 'J' significantly higher than 'D' [18, 19]. Above the critical H_c value the magnetization dynamic is mainly governed by the dominating Zeeman energy and magnetocrystalline anisotropy. The mgnetization relaxation in this case is much faster similar to the case of a regular AFM. This leads to the unusual H dependence of the remanent magnetization as observed in $MnCO_3$ and $NiCO_3$. Depending on the strength of DMI and, consequently, on the spin canting angle the value of H_c can vary. For instance, the critical field H_c shifts to a lower value with the increase of strength of DMI as observed in case of $NiCO_3$, $MnCO_3$ and α-Fe_2O_3. This implies that for the samples with large spin canting, the maximum magnetization pinning can be achieved at lower field values.

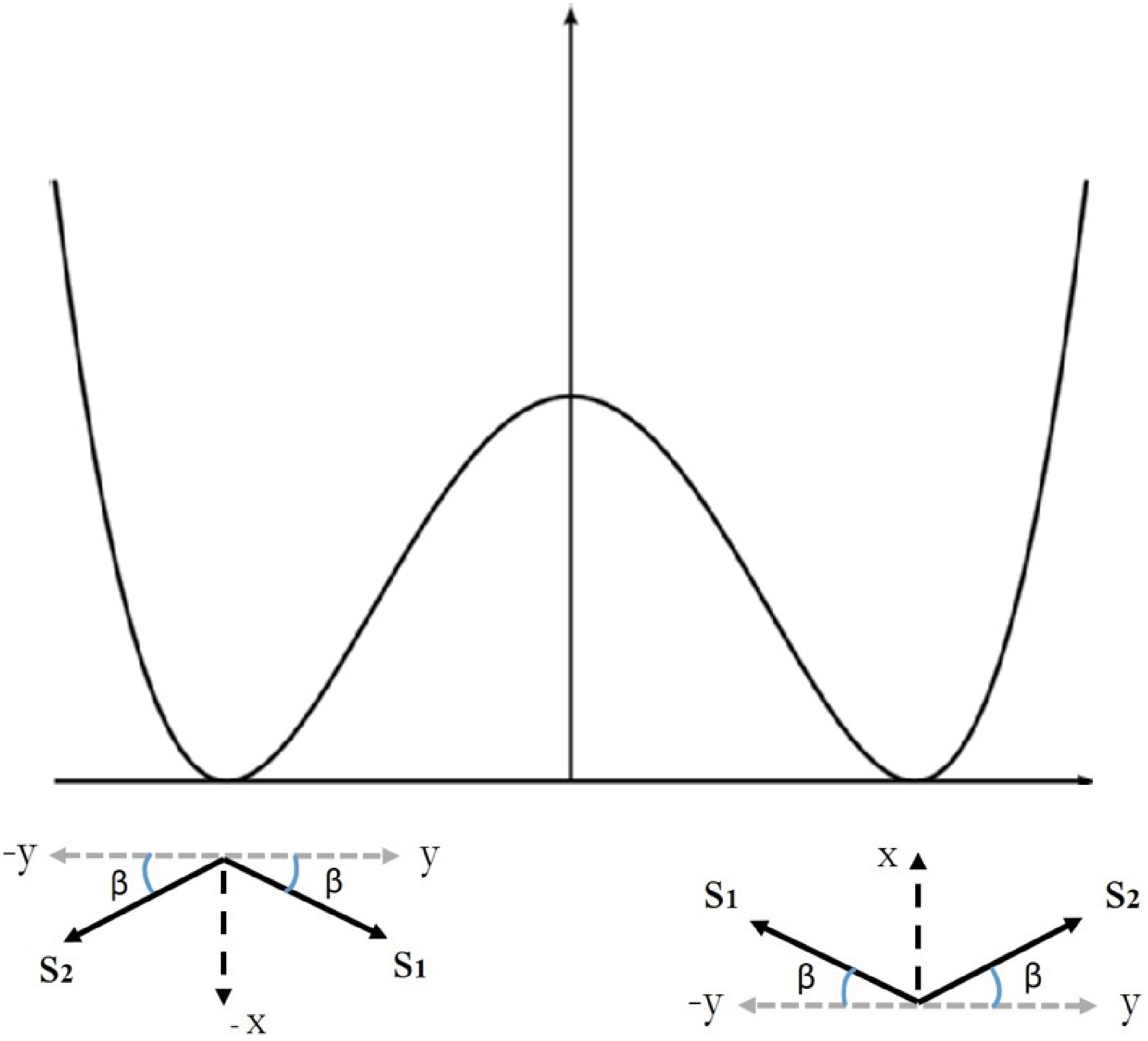

Figure 5.5 – Schematic of the possible ground state spin configuration in MCO_3 separated by the energy barrier.

We finally confirm the presence of *time-stable* remanence through the powder neutron diffraction (ND) measurements. We will discuss below results pertaining to the neutron diffraction performed in the remanent state on a representative carbonate sample that unravels the microscopic signature of *time-stable* remanence.

5.3 Microscopic evidence of time-stable μ: neutron diffraction study

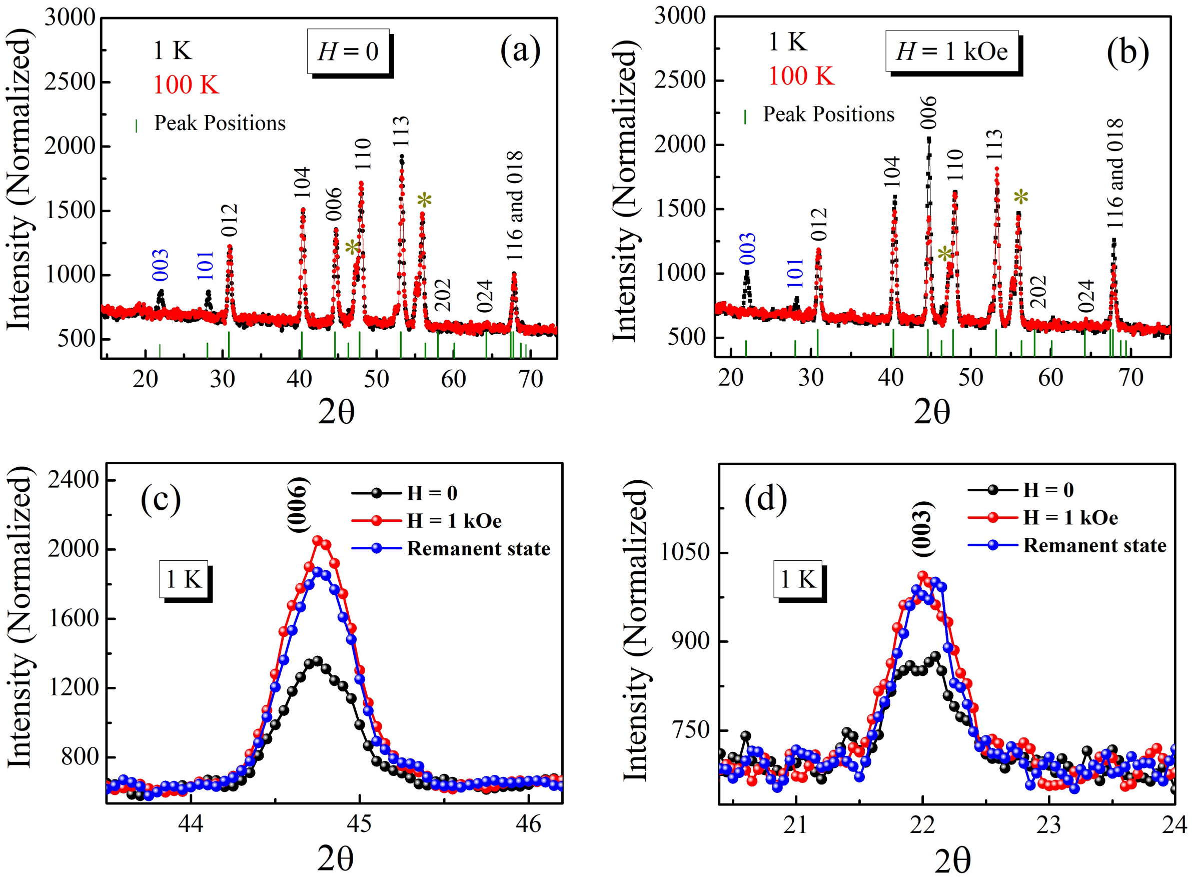

Figure 5.6 – (a)-(b) Neutron diffraction data recorded at 100 K (red dots) and 1 K (black dots) for $H = 0$ and 1 kOe respectively. The peak indexing is done in hex setting using Rietveld refinement. However complete data refinement could not be achieved due to the presence of two unknown peaks marked with stars in the Figs. (c) - (d) Depicts intensity comparison of the (006) and (003) diffraction peaks recorded for $H = 0$ (black dots), $H =$ 1 kOe (red dots) and remanent states (blue dots) respectively.

We have carried out the neutron diffraction measurement on a representative carbonate sample $CoCO_3$. Here our aim is to first perform ND in zero magnetic field as a function of temperature across the magnetic transition temperature. This would enable us to identify and isolate the Bragg peaks of magnetic origin. This is shown in Fig. 5.6 (a). The peak indexing is consistent with the Plumier's work on neutron diffraction study on the isostructural compound $NiCO_3$ [79, 81]. The difference between the two ND pattern recorded at 100 K and 1 K is the appearance of two new peaks (003) and (101) at 1 K implying these peaks are purely of magnetic origin. Next, we perform similar set of measurements but in presence of $H = 1$ kOe (5.6 (b)). The immediate observation is the significant enhancement in the intensity of (003) and (006) peaks at 1 K in presence of field as compared to the similar data recorded in zero H. (5.6 (a)). In the next step, we perform ND measurements in the remanent state with special attention to these (003) and (006) peaks. For this we first cool the sample from its paramagnetic region to 1 K in presence of 1 kOe field. At 1 K the applied field is removed and the diffraction pattern subsequently measured. These results plotted for the two selected peaks (003) and (006) is shown in Fig. 5.6 (c) and (d) respectively. The black, red and blue dots represent the diffraction data recorded at $H = 0$, $H = 1$ kOe and remanent state (applied H of 1 kOe has been removed) respectively. Here we see that intensity of both the peaks increases with the increase of H and after removal of H, in the remanent state, the intensity of both the peaks stays put with the intensity 1 kOe data. These data demonstrate microscopically that once the WFM domains have been guided during the field cooling process their rearrangement is energetically unfavourable. Thus in addition to our bulk magnetization measurements the ND data further brings out the presence of *time-stable* remanence and its connection with DMI. Though measurements on other samples are required, but these priliminary results of ND study in the remanent state in $CoCO_3$ holds promising information crucial to WFMs. Moreover, it is also to be noted that, even though the remanence in $CoCO_3$ is relatively less robust (stable) compared to that in $MnCO_3$ and $NiCO_3$, still we see that after the removal of (cooling) H, the intensity corresponding to the magnetic peaks does not decay over time scales of the order of several hours, in which ND data are collected. Thus the microscopic signature of *time-stable* remanence as evident from the ND data such as seen in $CoCO_3$ is likely to be present in other DMI driven WFM as well.

5.4 Conclusion

To summarize our results on remanences, we observe the presence of *time-stable* remanence with counter intuitive field dependence that are qualitatively similar in all prototype DMI driven compounds. These unique features of remanent magnetization are microscopically related to the spin canting mechanism present in the systems. The spin canting is associated with the well known Dzyaloshinskii-Moriya interaction, the manifestation of which can be realized through the remanent magnetization measurement. The remanent magnetization also follows a universal scaling behaviour observed in $MnCO_3$, $NiCO_3$ and $CoCO_3$. This scaling behaviour of remanence is due to the factorization of remanent magnetization, which also points towards its connection with concurrent phenomenon of piezomgnetism in these compounds. We notice an inverse correlation between the magnitude of remanence and the T_N of the respective WFMs. This observation provides crucial insights about the qualitative and quantitative determination of the extent of spin canting angle and the magnitude of remanence in WFMs which are associated with the lowering of T_N. Finally the presence of *time-stable* remanence has been confirmed through the neutron diffraction measurement performed on a representative carbonate sample.

Chapter 6

Dielectric and Raman Spectroscopy in α-Fe_2O_3 crystallites across the Morin transition

6.1 Introduction

Materials exhibiting an unusual entanglement between magnetic and electric order parameters have been the standpoint of investigation for its tremendous technological importance in futuristic memory storage and spintronic devices [122–124]. Often a strong coupling realized between these order parameters are the systems of particular magnetic symmetry with exotic spin structure that breaks the spatial inversion symmetry - an essential ingredient for the realization of nonzero polarization in a system. The classic example and the most well studied system of this kind is the magneto-electric (ME) compound Cr_2O_3, a rhombohedral antiferromagnet, in which the non-centrosymmetric magnetic order breaks the inversion symmetry and in consequence there appears an electrical polarization that changes linearly with the magnetic field [125, 126]. Other particular of this kind are the systems with non collinear spin structure for example, the spin driven ferroelectric compound $TbMnO_3$. In such systems a nonzero polarization develops due to the broken inversion symmetry caused by the well known Dzyaloshinskii-Moriya Interaction (DMI) [127–130]. DMI driven anomalies in the electrical character are therefore the subject matter of investigation in various magnetic insulators [4]. Regardless of the particular magnetic symmetry and the peculiar spin arrangement, there are also systems with strong spin-phonon interaction where a phenomenon of magneto-dielectric (MD) coupling has been realized with a great number in practice [131–134]. In such materials, a change in dielectric constant accompanies with the magnetic phase transitions or with magnetic field has also gained much attention for many practical applications [135–137].

α-Fe_2O_3 is a sister compound of the protypical magnetoelectric compound Cr_2O_3. Both these compounds belong to the same rhombohedral structure. The unit cell contains four magnetic atoms lying along the body diagonal of rhombohedron as shown in Fig. 1.5. Belonging to the same crystal structure both these compounds are different in terms of their magnetic symmetry. The AFM spin configuration in Cr_2O_3 is S_1 = -S_2 = S_3 = -S_4 where as in α-Fe_2O_3 it is S_1 = -S_2 = -S_3 = S_4. Thus in Cr_2O_3 the spin configuration itself breaks the spatial inversion symmetry whereas the particular magnetic symmetry of α-Fe_2O_3 forbids the observation of ME coupling but in turn allows the phenomenon of weak ferromagnetism driven by DMI [4, 18, 19]. The phenomenon of magnetoelectric effect and weak ferromagnetism are therefore mutually exclusive in these two rhombohedral compounds.

Although the coupling between magnetic and electrical order parameters is not normally expected in α-Fe_2O_3, a close inspection of the coupling phenomenon between these order parameters is still interesting owing to its non collinear spin structure that develops at the vicinity of Morin transition (T_M). To the best of our knowledge, no such studies have been made so far on α-Fe_2O_3 in great details. A most obvious and common way to examine the coupling between the magnetic and electric order parameters is to perform the dielectric spectroscopy in the proximity of magnetic transition in a magnetic material. In a recent study, a signature of magneto-dielectric coupling has been observed at the vicinity of the Morin transition in α-Fe_2O_3 [138]. The observed anomaly also seen to be enhanced with Ga doping in the system. However, in all these studies the temperature regime of the maxima of dielectric anomaly and the maxima of Morin transition are largely separated ($\sim$ 75 K). More importantly, though the anomaly is seen to be pronounced in doped α-Fe_2O_3 system, less attention has been paid in understanding the nature of coupling phenomena in the pristine α-Fe_2O_3 itself.

In the present work we therefore investigate dielectric characteristic in concern to the Morin transition in four different samples of α-Fe_2O_3 that are micro and nano plates, big and small cuboids. The as-prepared powder samples are first grinded properly by using a PVA (poly vinyl alcohol) binder. Using hydraulic KBr press, the samples were pelletized in the disc form of diameter $\sim$ 10 mm and thickness $\sim$ 2 mm. The pelletized samples were sintered at a temperature of 400 °C for 5 hours in a programmable furnace. In the next step, silver paste was used to prepare the electrodes on both sides of the sintered pellets. The applied paste was dried properly under a standard infra-red lamp and the conductivity on both sides of the pellet surface was checked using a digital multimeter before performing the dielectric measurements. We have ensured the pellet surface as flat as is possible in order to make a decent contact between the samples and electrodes. The dielectric measurements on the sintered pellets have been carried out at a drive of 1 V from room temperature down to 75 K in the frequency range of 100 Hz - 300 kHz using a Alpha-A High Performance Frequency analyzer from novocontol technology. In addition to dielectric spectroscopy, we have also performed Raman spectroscopy as a complimentary tool to probe the simultaneous excitations corresponding to the magnetic, lattice and electronic degrees of freedom, allowing one to understand the correlations existing between different order parameters in a given material [139–142]. Raman data acquired in the same temperature window brings forward the presence of spin-phonon coupling associated with the Morin transition and its influence on the dielectric properties of the samples investigated in this work.

6.2 Results and discussion

6.2.1 Temperature dependent Dielectric spectroscopy in hex-plates of α-Fe_2O_3

The dielectric constant or the complex permittivity of a material can be expressed as: $\epsilon = \epsilon'$ - iϵ'' where, ϵ' is the real part of the dielectric constant that accounts for the amount of energy storage and ϵ'' is the imaginary part corresponds to the dielectric losses in the material. In Fig. 6.1. we first present the temperature variation of the real and imaginary part of the dielectric constant measured across the Morin transition in the micro plates. The SEM image for the same is depicted in the inset of Fig. 6.1 (a). The left (Fig. 6.1 (a) and (b) and right (Fig. 6.1 (c) and (d)) panels correspond to the dielectric constant measured at low and high frequencies respectively. Here we observe that the dielectric constant monotonically increases with the increase of temperature and a clear anomaly is observed around the Morin transition. The anomaly in the dielectric constant is prominent at high frequencies and is quite subdued at low frequencies. To clearly bring out the anomalous change in the dielectric constant we have plotted the real part of the dielectric constant in conjunction with the magnetization (M) data as shown in Fig. 6.1 (e) and (f). Here both ϵ' and M are normalized with their respective values at 75 K. The inset shows the maxima of the temperature derivatives of ϵ' coinciding with the maxima of the temperature derivatives of magnetization data. The anomaly in ϵ' across the Morin transition is also concurrent with the simultaneous change in the slope of ϵ'' curves as shown in the inset of Fig. 6.1 (d). The occurrence of dielectric anomaly exactly across the Morin transition hints towards the phenomenon of MD coupling possibly present in this system.

The temperature and frequency dependent dielectric constant measured for nano plates

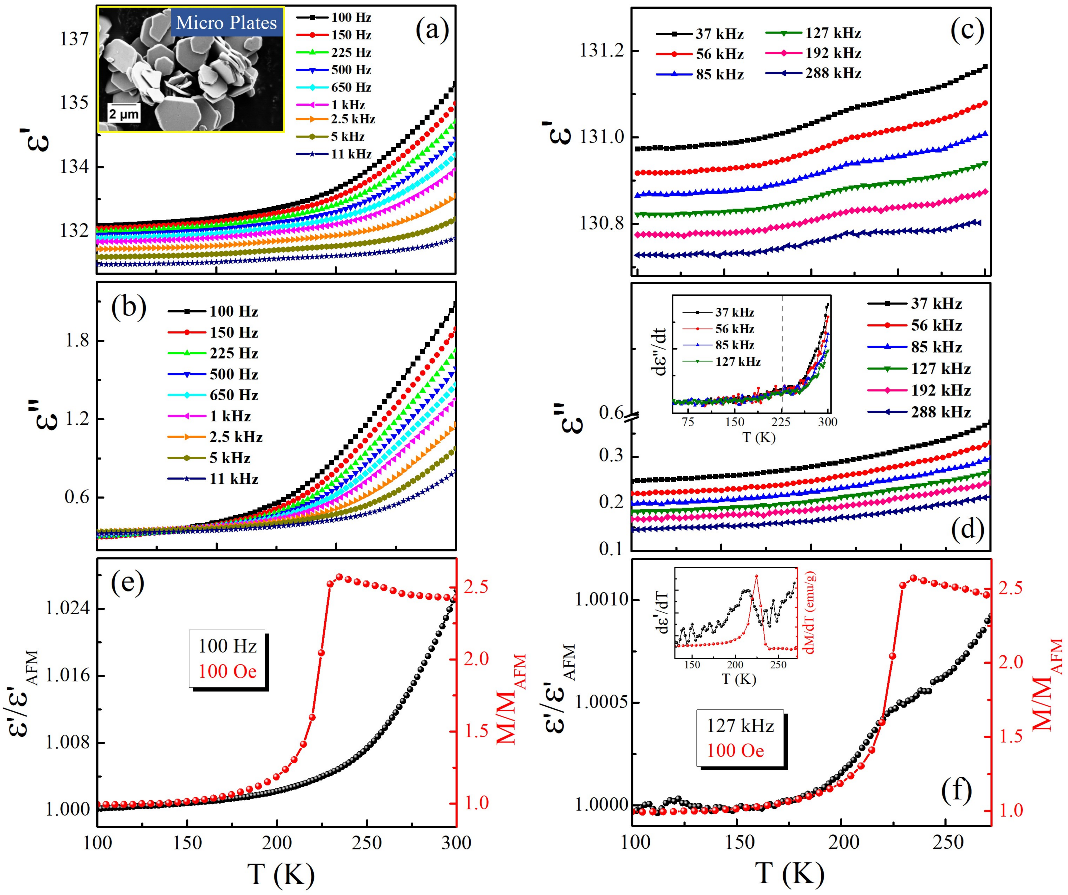

Figure 6.1 – (a) and (b) Temperature variation of ϵ' and ϵ'' respectively for micro plates at lower frequency regime. (c)and (d) depicts the same at higher frequency regime. (e) and (f) are normalized ϵ' plotted in conjunction with normalized magnetization data at lower and higher frequency respectively. The inset in (f) depicts the temperature derivatives of ϵ' and magnetization revealing the dielectric anomaly occurring in the vicinity of T_M of micro plates. The same anomaly is also reflected in the temperature derivative of ϵ'' curve shown in the inset of (d).

is presented in Fig. 6.2. The inset of Fig. 6.2 (a) depicts the SEM image for the same. Here we first note that the magnitude of ϵ' is nearly half ($\epsilon' \sim 60$) as compared to what is observed in micro plates ($\epsilon' \sim 130$, Figs. 6.1 (a) and (c)). It is also to be noted that S/V ratio of the same nano plates is nearly 20 times higher than the micro plates. Thus in plate shaped samples we observe a inverse relation of the ϵ' with the S/V ratio. The ϵ'' on the other hand for both the sample is of similar order of magnitude. However, unlike a clear anomaly in ϵ observed in micro plates, in case of nano plates, a mild anomaly (slope change feature in ϵ' as depicted in the inset of Fig. 6.2 (c)) is present around its

Morin transition. In addition, both ϵ' and more clearly ϵ'' of nano plates show relaxation behaviour with the maxima of dispersion shifting to higher temperature with the increase of frequency. On the other hand no relaxation mechanism is observed in the micro plates.

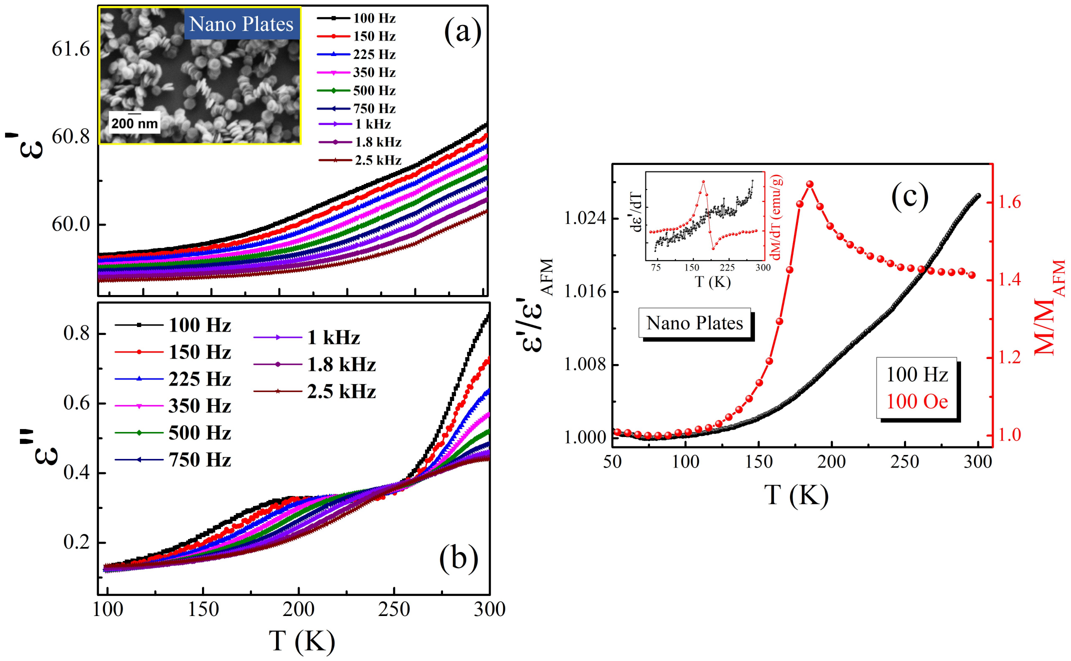

Figure 6.2 – (a) and (b) Temperature variation of ϵ' and ϵ'' respectively for the nano plates. Normalized ϵ' plotted in conjunction with normalized magnetization data is depicted in (c). The inset in (c) depicts the temperature derivatives of ϵ' and magnetization revealing the dielectric anomaly occurring in the vicinity of T_M of nano plates

6.2.2 Temperature dependent Dielectric spectroscopy in cuboids of α-Fe_2O_3

The temperature and frequency dependent dielectric constant measured for big and small cuboids is shown in Fig. 6.3. In cuboid shaped samples we notice the magnitude of ϵ' is rather similar irrespective of the S/V ratio which is 10 times larger in small cuboids as compared to that of big cuboids. Thus both morphology and S/V ratio seemingly play a part as far as the magnitude of ϵ' is concerned, whereas the magnitude of ϵ'' remains fairly in the similar order in all the four α-Fe_2O_3 samples of various sizes and morphology. A mild anomaly in the dielectric constant around the Morin transition is also evident in the big cuboids (Figs. 6.3 (e)) but is absent in the small cuboids. Similar trend of relaxation mechanism as observed in case of nano plates is also present in the big cuboids. On the other hand, the temperature dependence of both ϵ' and ϵ'' in small cuboids do not show any anomaly over the temperature and frequency range of investigation. The relaxation response in big cuboids and nano plates as depicted in Fig. 6.4 follows an Arrhenius law given by the relation

$$\tau = \tau_0 e^{\frac{E_a}{k_B T}} \tag{6.1}$$

Here k_B is the Boltzmann constant, T is the absolute temperature, τ_0 is the pre exponential factor representing the relaxation time at an infinite temperature (T_∞) and E_a is the activation energy of relaxation.

The linear behaviour observed between the log of relaxation time and temperature represents the thermally activated dipole population in the nano plates and big cuboids [143–146]. At low temperature these dipoles fail to align themselves with the sinusoidal variation of the electric field even at low frequency. With the increase of temperature, the dipolar motion becomes less constrained as a result the dipoles find little easy to align themselves with the sinusoidal field at low frequency but still find difficulties at higher frequencies. Thus with the increase of frequency, the maxima of the dispersion shifts to higher temperature due to smaller relaxation time required at high temperature. It is important to validate the observed anomalies are free from any extrinsic contributions such as space charge or Maxwell-Wagner effect. However, considering the extremely small values of ϵ' as well as ϵ'', we infer that the observed anomalies around the Morin transition are intrinsic in nature as any extrinsic contributions always tend to enhance both the dielectric constant and the losses [65, 147, 148]. It is known that in magnetic ferroelectrics, a strong polarization in the vicinity of the magnetic ordering results in the appearance of a dielectric anomaly across the magnetic transition. In such systems

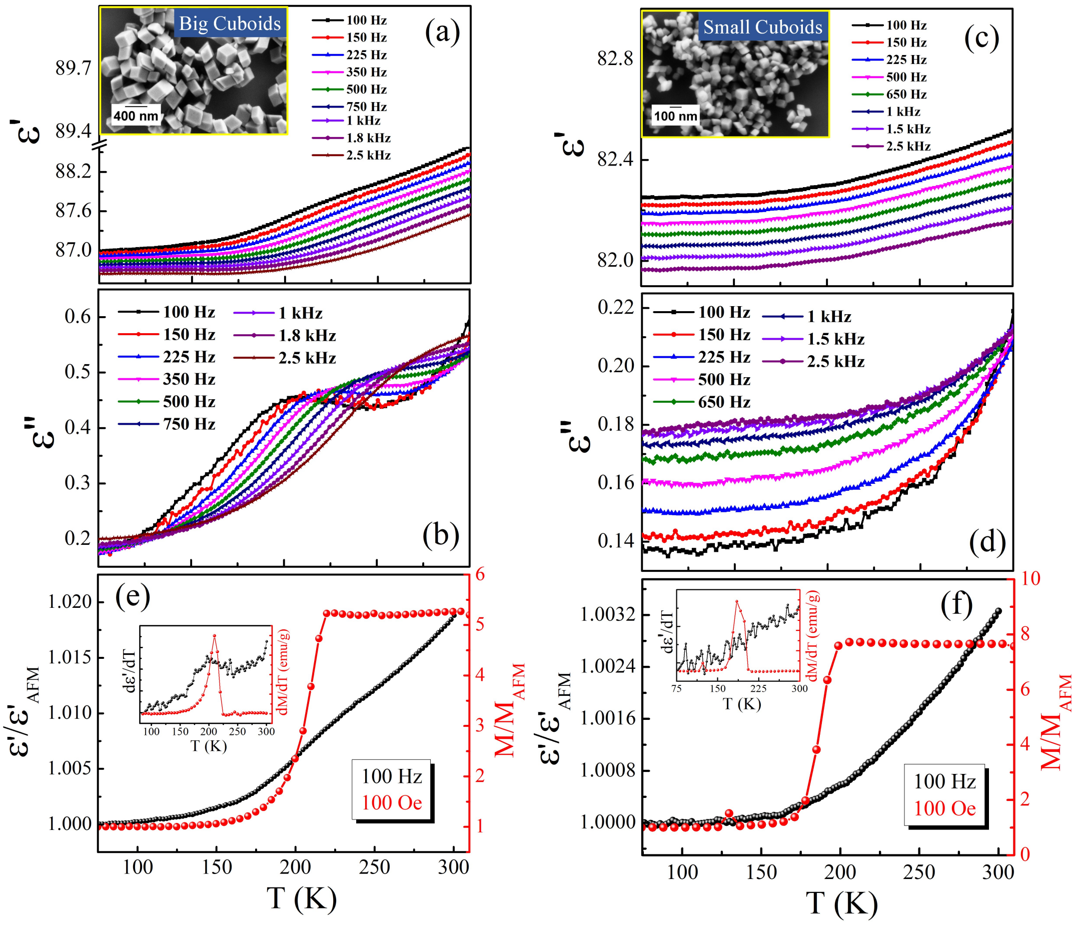

Figure 6.3 – (a) and (b) Temperature variation of ϵ' and ϵ'' respectively for big cuboids. (c) an (d) represents the same for small cuboids. (e) and (f) are normalized ϵ' plotted in conjunction with normalized magnetization for big and small cuboids respectively. The insets in (e) and (f) depicts the temperature derivatives of ϵ' and magnetization. The inset in (e) reveals dielectric anomaly occurring in the vicinity of T_M in big cuboids.

a particular non collinear spin structure is an essential ingredient for the appearance of electrical polarization [127–131]. Microscopically, the coupling between magnetic and electric order parameters in such systems is governed mainly by the DM interactions. In our case, the relaxation mechanism in the vicinity of Morin transition would suggest that the dipole formation is possibly due to the non-collinear spin arrangement that occurs due to DMI at the Morin transition. On the other hand, the activation energy, deduced from the Arrhenius fit of our results agrees with earlier results observed in the particular α-Fe_2O_3 systems, suggesting the role of polaron hopping in the relaxation mechanism [144, 145]. Thus, with the present set of data, it is non trivial to isolate the exact origin

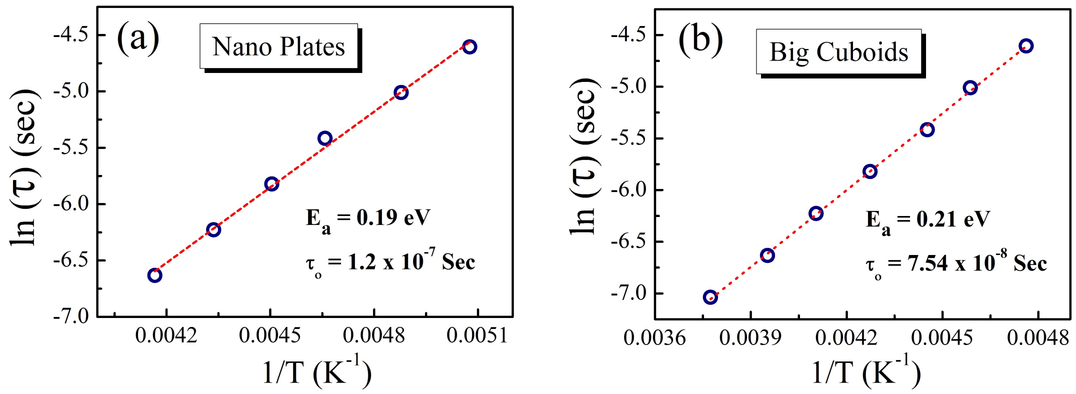

Figure 6.4 – Temperature variation of log of relaxation times obeying Arrhenius law in nano plates and big cuboids.

of the relaxation behaviour. Additional measurements would be required to understand clearly the origin of the relaxationlike feature in these two systems. A small upturn in ϵ'' curves observed in both the samples at higher temperature can be attributed to an extremely small change in electrical conductivity in that temperature region [149].

From the frquency and temperature dependent dielectric spectroscopy studied in four different samples of α-Fe_2O_3, we broadly observe a subtle but finite change in the dielectric constant around the Morin transition. This feature observed more clearly in thick plates indicates the phenomenon of MD coupling to be present in hematite. It is known that in magnetodielectric systems, the dielectric anomaly appears at the magnetic transition does not necessarily evolve with the appearance of spontaneous electrical polarization [127–131]. In such systems the change in dielectric constant at the vicinity of spin-spin correlations is generally mediated by spin-phonon coupling. Physically this means that we need to understand the effect of spin-spin correlation on the underlying lattice structure, across the magnetic transition, which changes the dielectric property of a material[131]. Raman spectroscopy in this regard is a powerful tool which can probe the simultaneous excitation corresponding to the magnetic, lattice and electronic degrees of freedom. Thus in order to shed light on the anomalous behaviour of the dielectric constant we investigate spin-phonon coupling at the vicinity of Morin transition through the temperature dependent Raman spectroscopy studies performed on a representative α-Fe_2O_3 sample.

.

6.2.3 Temperature dependent Raman spectroscopy

We have carried out temperature dependent Raman spectroscopy study from room temperature down to 80 K on big cuboids using a HeNe laser of $\lambda \sim 532$ nm. A characteristic Raman spectra acquired at 300 K fitted using Lorentzian peak profile fit is shown in Fig. 6.5 (a). The assignment of Raman active modes is consistent with the group theoretical prediction of the space group R3-c [150]. The modes located at 225 cm $^{-1}$ and 500 cm $^{-1}$ are the symmetric modes of A_{1g} symmetry and the modes located at 246 cm^{-1}, 290 cm^{-1}, 295 cm^{-1}, 408 cm^{-1}, 500 cm^{-1} and 610 cm^{-1} are the doubly degenerate modes of E_g symmetry. Here A_{1g} symmetry involves the movement of Fe atom along the c-axis of the unit cell and E_g symmetry involves the symmetric breathing mode of the O atoms relative to the Fe atoms in the plane perpendicular to the c axis of the unit cell [151, 152]. The mode E_u, assigned at 660 cm^{-1} in general is not Raman active and its appearance has been attributed to the disorder related to surface defects and grain sizes. The mode located at 1320 cm^{-1} is related by a factor of two with the E_u mode. A weak peak observed in the spectra range of 1500-1600 cm^{-1}, merged with the tail of $2E_u$ mode, is due to the two-magnon scattering in α-Fe_2O_3 [153, 154].

The temperature dependent Raman spectra acquired in the temperature range of 300 K - 80 K is shown in Fig. 6.5 (b). Raman spectra as a function of temperature for two selected modes $A_{1g}(1)$ and $E_g(5)$ is shown in Fig. 6.5 (c) and (d) respectively. These data depicts the anomalous shift in the Raman modes at the vicinity of Morin transition. The phonon frequency evolutions as a function of temperature, obtained after the Lorentzian peak profile fit for both the modes is shown in Fig. 6.6 (a) and (b) respectively. The

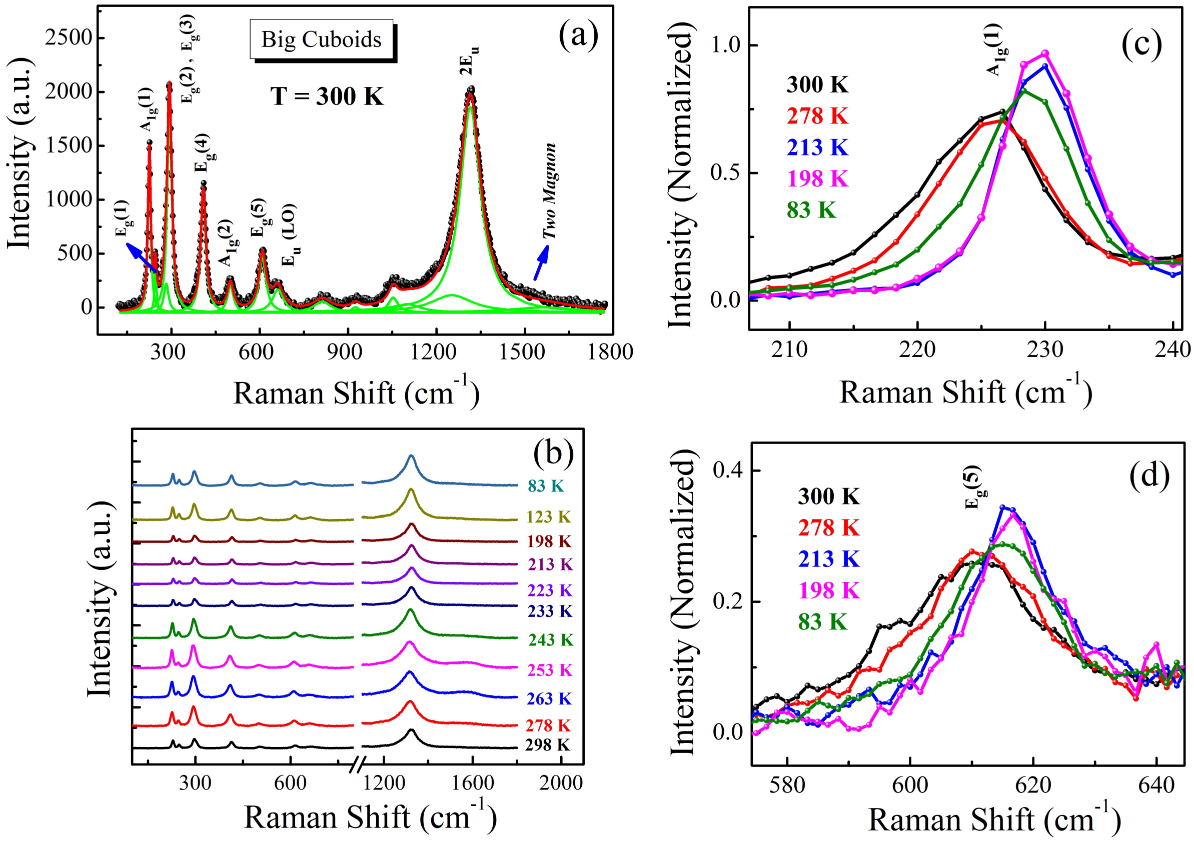

Figure 6.5 – (a) Characteristic Raman spectra acquired on big cuboids of α-Fe_2O_3. (b) Raman spectra of the same cuboids at different temperature of interest. (c) and (d) Raman spectra as a function of temperature for $A_{1g}(1)$ and $E_g(5)$ modes. These data depict anomalous Raman shift in the modes on the either side of the Morin transition.

variation of phonon frequency as a function of temperature in a magnetic material can be expressed as [155]

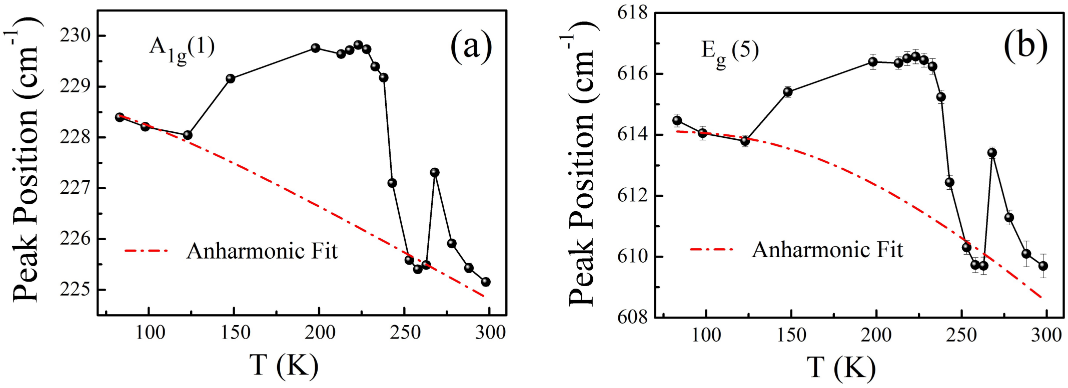

Figure 6.6 – Variation of peak positions with temperature for the selected Raman modes (a) $A_{1g}(1)$, (b) $E_g(5)$. The peak positions are extracted from the lorentzian peak profile fit.

$$\begin{aligned} \omega(T) - \omega(0) = \Delta\omega(T) &= \Delta\omega_{lattice} \\ &+\Delta\omega_{phonon-phonon} \\ &+\Delta\omega_{spin-phonon} \end{aligned} \tag{6.2}$$

Where ω(T) and ω(0) in L.H.S are the Raman frequency at T and 0 K respectively. The contribution from the first term in R.H.S is due to the lattice expansion/contraction, second term is due to phonon-phonon interaction and last term implies the contribution of spin-phonon coupling in the modulation of phonon frequency. Neglecting the contributions from the lattice and spin-phonon coupling, the variation of phonon frequency as a function of temperature can be simulated by the anharmonic decay of phonon frequency model expressed as [141, 142]

$$\omega(T) = \omega(0) - C\left(1 + \frac{2}{e^x - 1}\right) \tag{6.3}$$

Here C is an adjustable parameter, x = $\hbar\omega_0$/ k$_B$T, k$_B$ is the Boltzmann constant and T is the absolute temperature.

The simulated curves of the anharmonic phonon decay are shown in red lines in Figs. 6.6 (a) and (b). The phonon frequency evolutions as a function of temperature in both the modes follows the anharmonic behaviour (red lines) except a noticeable deviation observed around the Morin transition. Considering the subtle changes in lattice parameters around the Morin transition observed earlier in these samples, the deviations in the mode positions around the Morin transition can be attributed to arise due to the combined effect of spin-phonon and lattice contributions. We interpret that such a spin-phonon coupling is inherently responsible for the appearance of dielectric anomaly at the vicinity of AFM to WFM transition that occurs across the Morin transition. We also observe a small deviation in phonon frequency evolution around the temperature regime of ∼

250 K. We infer that this small deviation is more likely due to the presence of a double transition as evident from the remanent magnetization versus temperature data discussed in chapter-4 on this sample [156].

6.3 Conclusion

From the temperature and frequency dependent dielectric measurements conducted in α-Fe_2O_3 crystallites of various morphologies and sizes we broadly observe that nano scaling results in significant decrease in the dielectric constant in case of hexagonal shaped plates whereas in case of cuboids no significant changes were observed as far as the magnitude of dielctric constant is concerned. A subtle but finite change in the dielectric constant is observed around the Morin transitions of the respective samples. The presence of relaxationlike behaviour obeying Arrhenius law as observed in nano plates and big cuboids needs further exploration. The simultaneous observation of the anomalous hardening of Raman modes around the Morin transition brings forward the presence of spin-phonon coupling and magnetodielectricity in the α-Fe_2O_3 systems.

Chapter 7

Conclusion and future prospectives

7.1 Epilogue

In this thesis we have explored remanent magnetization in a varieties of rhombohedral AFMs that are $MnCO_3$, $CoCO_3$, $NiCO_3$ and α- Fe_3O_3. Such AFMs are symmetry allowed DMI driven WFMs and also exhibit the phenomenon of piezomagnetism under the external stress. All the samples we have studied in polycrystalline form, synthesized by the hydrothermal and precipitation methods. We have used dc magnetization measurement in the remanent state as a primary tool to explore the remanent magnetization in these systems.

We have explored remanent magnetization systematically in $MnCO_3$, $NiCO_3$ and $CoCO_3$. In all these system we have observed two distict time scale of magnetization relaxation one of which is ultraslow leading to the observation of *time-stable* remanence. Furthermore the magnitude of this *time-stable* remanence varies with the strength of cooling H in a very unusual way. The magnitude of *time-stable* remanence is small for low as well as higher H values used to prepare the remanent state. There is a particular H at which the magnitude of *time-stable* remanence attains the maximum value. These unique features of remanence observed in the series of carbonate samples are intrinsic in nature, connected intimately to the spin canting mechanism driven by DMI present in the systems. In all these carbonates we also observe a scaling behaviour of remanence which is due to the factorization of remanent magnetization resulted from the weak ferromagnetic domains. We also have explored remanent magnetization in the isostructural compound $FeCO_3$ which is not a WFM but is a symmetry allowed PzM. The qualitative features of remanent magnetization in $FeCO_3$ has similar grounds as that of other weak ferromagnetic carbonates as far as nano-scaling is concerned. Remanence measurement on bulk $FeCO_3$ will certainly be interesting. We are in the process of exploring remanent magnetization in bulk $FeCO_3$ particles to realize if the qualitative features of remanence are intrinsic to the system.

α- Fe_3O_3 is a unique compound which exists both in a low temperature AFM phase and a room temperature WFM phase marked by the Morin transition. Considering the practical applicability of room temperature weak ferromagnetism, we have explored remanent magnetization inα- Fe_3O_3 in different length scale systems starting from bulk single crystal (SC) to nano structures of various shapes, sizes and morphologies. The *time-stable* nature of remanence observed in different length scale systems of α- Fe_3O_3 including the bulk SC further reinforces its origin is solely connected to the DMI driven weak ferromagnetic phase intrinsic to the systems. We have also demonstrated that the magnitude of the *time-stable* remanence can significantly be tuned with nanoscaling. The temperature variation of remanence study corroborated by the extensive structural investigations using low temperature synchrotron XRD bring out the clear correlation between the strain effects, the Morin transition, extent of spin canting angle and the magnitude of remanence. In particular we observe that with the increase of S/V ratio, a reduction in the T_M to around 125 K leads to four times increment in the remanence. The AFM to WFM transition in α- Fe_3O_3 samples of various sizes and morphologies has also been investigated through the dielectric and Raman spectroscopy measuremets. The study has revealed the presence of spin-phonon and magneto-dielectric coupling around the AFM to WFM transition in α- Fe_3O_3.

We observe an inverse correlation between the magnitude of remanence and the T_N which tells that maximum pinning of remanent magnetization can be obtained in the WFMs of lower T_N. The maximum magnitude of remanence with the lowering of T_N gives the notion of the extent of spin canting angle the estimation of which, in general, is a non trivial task.

We finally performed neutron diffraction measurement in remanent state on a representative weak ferromagnetic sample $CoCO_3$. The study has provided microscopic evidence for the presence of *time-stable* remanence in weak ferromagnets.

7.2 Future scopes and aspects

In this thesis we have explored remanent magnetization in DMI driven rhombohedral structured WFMs. Remanent magnetization in a vast number of DMI driven WFMs remains yet to be explored. For example, the transition metal triflourides such as CoF_3 and FeF_3 are the potential DMI driven WFMs. It is also interesting to investigate remanent magnetization in compounds where weak ferromagnetism is not driven by DMI. The protypical examples are transition metal diflourides such as CoF_2, MnF_2 etc. The detail synthesis process and characterization of a protypical diflouride MnF_2 is given in Appendix-2.

The presence of *time-stable* remanence in the WFM/PzM compounds can be relevant for the upcoming areas of antiferromagnetic spintronics where such WFM/PzM can be employed as a pinning layer in order to pin a FM layer and more importantly the effect can be tunable by a mechanical stress alone. In this regard, the *time-stable* character of remanence at room temperature will particularly be useful. α- Fe_3O_3 is one of such kind where the presence of *time-stable* remanence at room temperature we have explored in this thesis . In the same compound we have also optimized the magnitude of *time-stable* remanence through nanoscaling. Another possible way to tune the magnitude of *time-stable* remanence in α- Fe_3O_3 is doping. Doping with a suitable element can modulate the strain effects and consequently the magnitude of remanence. However, the effect of magnetic and non-magnetic dopants on the acquisition of *time-stable* remanence has to be optimized. Ultrathin films and heterostructures are also important in this aspect. It is also important to investigate the *time-stable* nature of remanence in various other room temperature WFMs. The multifunctional perovskites orthoferrites such as $YFeO_3$, $GdFeO_3$, $BiFeO_3$ are the typical examples. Other particular of this kind are the triangular AFMs such as Mn_3Sn, Mn_3Ga etc. In addition to bulk measurements, neutron diffraction with topography measurements can provide better insights about the weak ferromagnetic domains and the *time-stable* remanence.

Appendices

Appendix-1

Analysis of Dzyaloshinskii

Let us denote the two spins in the unit lattice as s_1, s_2. Then, the magnetization vector $\mathbf{m}$ and the antiferromagnetic vector $\mathbf{l}$ are defined as

$$\mathbf{m} = s_1 + s_2, \quad \mathbf{l} = s_1 - s_2. \tag{1}$$

It follows from these definitions that

$$\mathbf{l}.\mathbf{m} = (s_1 - s_2).(s_1 + s_2) = s_1^2 - s_2^2 = 0 \tag{2}$$

if we assume the two spins to be of equal magnitude. Namely, the antiferromagnetic vector is always perpendicular to the magnetization vector for equal spin magnitudes. The two relations in (1) and (2) can be inverted to give

$$s_1 = \frac{1}{2}(\mathbf{m} + \mathbf{l}), \quad s_2 = \frac{1}{2}(\mathbf{m} - \mathbf{l}). \tag{3}$$

We note that, while (2) allows for $\mathbf{m} = 0, \mathbf{l} \neq 0$ and $\mathbf{l} = 0, \mathbf{m} \neq 0$, it does not allow both the vectors to vanish simultaneously (namely, $\mathbf{l} = \mathbf{m} = 0$), since from (3) that would imply $\mathbf{s}_1 = \mathbf{s}_2 = 0$ which is not true. This can happen as an average over the sample in a paramagnetic system, but not at the fundamental level of a unit cell.

Lowest order thermodynamic potential:

With these notations, let us next turn to the lowest order phenomenological thermodynamic potential considered by Dzialoshinskii [18]. It describes relativistic spin-spin interaction and has the form

$$\Phi_0 = \frac{A}{2}\mathbf{l}^2 + \frac{B}{2}\mathbf{m}^2 + \frac{a}{2}\ell_z^2 + \frac{b}{2}m_z^2 + \beta(\ell_x m_y - \ell_y m_x) + \frac{C}{4}(\mathbf{l}^2)^2, \tag{4}$$

where (ℓ_x, ℓ_y, ℓ_z) and (m_x, m_y, m_z) denote the Cartesian components of the vectors $\mathbf{l}$ and $\mathbf{m}$ respectively and

$$\mathbf{l}^2 = \ell_x^2 + \ell_y^2 + \ell_z^2, \quad \mathbf{m}^2 = m_x^2 + m_y^2 + m_z^2. \tag{5}$$

In (4), the constants A, B, C, a, b are phenomenological parameters determined experimentally for a given sample (the constant α in Dzialoshinskii's paper is written here as a for uniformity). We note, from (3), that (remember (2))

$$\mathbf{s}_1 \cdot \mathbf{s}_2 = \frac{1}{4}(\mathbf{m}+\mathbf{l}) \cdot (\mathbf{m}-\mathbf{l}) = \frac{1}{4}(\mathbf{m}^2 - \mathbf{l}^2), \tag{6}$$

so that the conventional exchange interaction between spins, $-J\mathbf{s}_1 \cdot \mathbf{s}_2$, is contained in the two isotropic terms $\frac{A}{2}\mathbf{l}^2$ and $\frac{B}{2}\mathbf{m}^2$. Similarly, (3) leads to

$$\mathbf{s}_1 \times \mathbf{s}_2 = \frac{1}{4}(\mathbf{m}+\mathbf{l}) \times (\mathbf{m}-\mathbf{l}) = \frac{1}{4}(-\mathbf{m} \times \mathbf{l} + \mathbf{l} \times \mathbf{m}) = \frac{1}{2}\mathbf{l} \times \mathbf{m}, \tag{7}$$

so that the Dzialoshinskii-Moriya interaction (DMI),

$$\mathbf{D} \cdot (\mathbf{s}_1 \times \mathbf{s}_2) = \frac{1}{2}\mathbf{D} \cdot (\mathbf{l} \times \mathbf{m}), \tag{8}$$

is contained in the anisotropic interaction term of Dzialoshinskii in (4), namely,

$$\beta(\ell_x m_y - \ell_y m_x) = \beta\hat{\mathbf{z}} \cdot (\mathbf{l} \times \mathbf{m}) = \frac{1}{2}\mathbf{D} \cdot (\mathbf{l} \times \mathbf{m}), \tag{9}$$

where the assumption is that the spins lie in the x-y plane and that $\mathbf{D} = 2\beta\hat{\mathbf{z}}$.

Symmetries of the lowest order potential:

There are a couple of things to note from the structure of the lowest order thermodynamic potential Φ_0 in (4). First, the fixed vector $\mathbf{D} = 2\beta\hat{\mathbf{z}}$ (see (9)) breaks the three dimensional rotational symmetry (isotropy) since it singles out a unique direction in space (z axis). However, it still leaves a two dimensional rotation in the x-y plane (or around the z-axis) as a symmetry of the system since a rotation around the z axis does not change the z component of a vector (namely, $D_z = 2\beta$). This rotational symmetry transformation (around the z-axis or in the x-y plane) can be written explicitly as

$$\begin{aligned}
&\ell_x \to \ell'_x(\alpha) = \ell_x \cos\alpha + \ell_y \sin\alpha, && m_x \to m'_x(\alpha) = m_x \cos\alpha + m_y \sin\alpha,\\
&\ell_y \to \ell'_y(\alpha) = -\ell_x \sin\alpha + \ell_y \cos\alpha, && m_y \to m'_y(\alpha) = -m_x \sin\alpha + m_y \cos\alpha,\\
&\ell_z \to \ell'_z(\alpha) = \ell_z, && m_z \to m'_z(\alpha) = m_z. \qquad (10)
\end{aligned}$$

Here $0 \leq \alpha < 2\pi$ denotes the angle of rotation around the z-axis. This rotational symmetry of the lowest order thermodynamic potential makes the choice of the ground state (minimum) nonunique, as we will see. However, the minima of the thermodynamic potential become unique when higher order interaction terms are added which break this symmetry. The second thing to note is that the thermodynamic potential Φ_0 in (4) is quadratic in the spin variables $\mathbf{s}_1, \mathbf{s}_2$ (or, equivalently in $\mathbf{l}, \mathbf{m}$), and, therefore, is also invariant under the discrete spin reflection symmetry

$$\mathbf{s}_1 \to -\mathbf{s}_1, \quad \mathbf{s}_2 \to -\mathbf{s}_2, \qquad (11)$$

or, equivalently, under

$$\mathbf{l} \to -\mathbf{l}, \quad \mathbf{m} \to -\mathbf{m}. \tag{12}$$

We note here that the parameters A, B, C in the thermodynamic potential (4) are assumed to satisfy $A < 0,\ B, C > 0$ and the interaction terms with parameters a, β are assumed to be nonrelativistic in the sense that $(|A| \sim B)$

$$|\frac{a}{A}| \sim |\frac{\beta}{B}| \sim O\left(\left(\frac{v}{c}\right)^2\right) \sim 10^{-2}. \tag{13}$$

Ground states of the thermodynamic potential:

The minima of the potential can now be calculated in a straightforward manner and are determined from

$$\frac{\partial \Phi_0}{\partial m_x} = Bm_x - \beta \ell_y = 0, \qquad \text{or,} \quad m_x = \frac{\beta}{B}\ell_y, \tag{14}$$

$$\frac{\partial \Phi_0}{\partial m_y} = Bm_y + \beta \ell_x = 0, \qquad \text{or,} \quad m_y = -\frac{\beta}{B}\ell_x, \tag{15}$$

$$\frac{\partial \Phi_0}{\partial m_z} = (B + b)m_z = 0, \qquad \text{or,} \quad m_z = 0, \tag{16}$$

$$\frac{\partial \Phi_0}{\partial \ell_x} = A\ell_x + \beta m_y + C\mathbf{l}^2 \ell_x = 0, \tag{17}$$

$$\frac{\partial \Phi_0}{\partial \ell_y} = A\ell_y - \beta m_x + C\mathbf{l}^2 \ell_y = 0, \tag{18}$$

$$\frac{\partial \Phi_0}{\partial \ell_z} = (A + a)\ell_z + C\mathbf{l}^2 \ell_z = 0. \tag{19}$$

From (16), we see that the z component of magnetization has to be always zero in this lowest order theory. The other five equations, however, lead to two different classes of solutions.

1. To understand the first class of the two solutions, we note from (14) and (15) that if $\mathbf{l} = 0$, these two equations would imply $m_x = m_y = 0$. Together with $m_z = 0$ (see (16)), this would imply $\mathbf{m} = 0$. However, as we have seen earlier (see the discussion after (3)), $\mathbf{l} = 0 = \mathbf{m}$ is not allowed. On the other hand, we can have $\mathbf{m} = 0$ which would lead from (14)-(15) that $\ell_x = \ell_y = 0$. This is compatible with (17)-(18), while (19) will yield

$$\begin{aligned} &\left((A+a) + C\mathbf{l}^2\right)\ell_z = 0, \\ \text{or,} \quad &\mathbf{l}^2 = \ell_z^2 = -\frac{A+a}{C}. \end{aligned} \tag{20}$$

Namely, the first class of solutions will have the form

$$\mathbf{m} = 0, \quad \ell_x = \ell_y = 0, \quad \ell_z^2 = \mathbf{l}^2 = -\frac{A+a}{C}, \tag{21}$$

and since a is a small parameter, consistency of the last relation (see also (20)) requires that $\frac{A}{C} < 0$ which is satisfied by our choice of parameters earlier (see the statement prior to (13)). Since magnetization vanishes in this case, such a state would correspond to an antiferromagnetic ground state. Note that, for such a solution, the contribution from the Dzialoshinskii-Moriya interaction (DMI) which is responsible for canting and, consequently, weak ferromagnetism vanishes. The value of the thermodynamic potential $\Phi_0^{(I)}$ (see (4)) at the minimum, in this case, is simply obtained to be (see (21))

$$\begin{aligned}\Phi_0^{(I)}(\text{min}) &= \frac{A}{2}\mathbf{l}^2 + \frac{a}{2}\ell_z^2 + \frac{C}{4}(\mathbf{l})^2 = \frac{(A+a)}{2}\mathbf{l}^2 + \frac{C}{4}(\mathbf{l})^2\\ &= \frac{(A+a)}{2}\left(-\frac{(A+a)}{C}\right) + \frac{C}{4}\left(-\frac{(A+a)}{C}\right)^2\\ &= -\frac{(A+a)^2}{4C} = -\frac{A^2}{4C}\left(1+\frac{a}{A}\right)^2 \simeq -\frac{A^2}{4C} - \frac{Aa}{2C}.\end{aligned}\tag{22}$$

where we have used the fact that $\frac{a}{A} \sim 10^{-2}$ is very small (see (13)).

2. Even though $m_z = 0$ (see (16)), the second class of solutions allows for a nonvanishing magnetization on the x-y plane. For example, for

$$m_z = 0 = \ell_z,\tag{23}$$

(19) is satisfied identically. On the other hand, (17) and (18) lead to

$$\begin{aligned}A\ell_x + \beta m_y + C\mathbf{l}^2\ell_x &= \left(A - \frac{\beta^2}{B} + C\mathbf{l}^2\right)\ell_x = 0,\\ A\ell_y - \beta m_x + C\mathbf{l}^2\ell_y &= \left(A - \frac{\beta^2}{B} + C\mathbf{l}^2\right)\ell_y = 0,\end{aligned}\tag{24}$$

where we have used the relations (14) and (15). Equation (24) shows that ℓ_x, ℓ_y do not have to be zero provided (remember $\ell_z = 0$)

$$\mathbf{l}^2 = \ell_x^2 + \ell_y^2 = -\frac{A - \frac{\beta^2}{B}}{C},\tag{25}$$

which once again emphasizes that $\frac{A}{C} < 0$ consistent with our choice of parameters. Therefore, we see that if ℓ_x, ℓ_y do not vanish, from (14) and (15), we see that m_x, m_y also do not vanish and there is a small magnetization ($|\frac{\beta}{B}| \sim 10^{-2}$) in the

x-y plane. However, the problem is that the equations (14), (15) and (25) do not determine the direction of $\mathbf{l}$ and, therefore, the direction of the magnetization on the x-y plane. This has to do with the rotational symmetry of Φ_0 around the z-axis discussed earlier (around (10)). For example, if $(m_x, m_y, \ell_x, \ell_y)$ satisfy (14) and (15), then the transformed components (under rotation, see (10)), namely, $(m'_x(\alpha), m'_y(\alpha), \ell'_x(\alpha), \ell'_y(\alpha))$ will also be a solution, namely, they will also satisfy (14), (15) and (24)

$$m'_x(\alpha) = \frac{\beta}{B}\ell'_y(\alpha), \quad m'_y(\alpha) = -\frac{\beta}{B}\ell'_x(\alpha), \quad \mathbf{l}'^2(\alpha) = \mathbf{l}^2(\alpha) = -\frac{A - \frac{\beta^2}{B}}{C}, \tag{26}$$

for any $0 \leq \alpha < 2\pi$. As we will see, this nonuniqueness in the solution (magnetization) is lifted when higher order terms are added to the interaction. Even if we choose a ground state, there is still the spin reflection symmetry (11) or, equivalently (12) in the system which leads to a double degeneracy in the minima.

True ground state:

Let us next calculate the value of the thermodynamic potential at any such degenerate minimum. Equations (14) and (15) lead to

$$\mathbf{m}^2 = m_x^2 + m_y^2 = \frac{\beta^2}{B^2}(\ell_y^2 + \ell_x^2) = \frac{\beta^2}{B^2}\mathbf{l}^2 = -\frac{\beta^2}{B^2}\left(\frac{A - \frac{\beta^2}{B}}{C}\right), \tag{27}$$

where we have used (25). Similarly, using (14), (15) and (25), we obtain

$$\ell_x m_y - \ell_y m_x = -\frac{\beta}{B}(\ell_x^2 + \ell_y^2) = -\frac{\beta}{B}\mathbf{l}^2 = \frac{\beta}{B}\left(\frac{A - \frac{\beta^2}{B}}{C}\right). \tag{28}$$

Using these, we can calculate the value of the thermodynamic potential at the minimum as (see (4))

$$\begin{aligned}\Phi_0^{(II)}(\text{min}) &= \frac{A}{2}\left(-\frac{A-\frac{\beta^2}{B}}{C}\right)+\frac{B}{2}\left(-\frac{\beta^2}{B^2}\frac{A-\frac{\beta^2}{B}}{C}\right)+\frac{\beta^2}{B}\left(\frac{A-\frac{\beta^2}{B}}{C}\right)+\frac{C}{4}\left(-\frac{A-\frac{\beta^2}{B}}{C}\right)^2\\ &= -\frac{1}{2C}\left(A-\frac{\beta^2}{B}\right)^2+\frac{1}{4C}\left(A-\frac{\beta^2}{B}\right)^2=-\frac{1}{4C}\left(A-\frac{\beta^2}{B}\right)^2. \qquad (29)\end{aligned}$$

Using the fact that $|A| \sim B$ and $|\frac{\beta}{B}| \sim 10^{-2}$ is small (see (13)), this simplifies to

$$\Phi_0^{(II)} \simeq -\frac{A^2}{4C}\left(1-\frac{\beta^2}{AB}\right)^2 \simeq -\frac{A^2}{4C}, \qquad (30)$$

where we have discarded terms of order 10^{-4} in order to be consistent with (22).

Thus, we see that the lowest order thermodynamic potential Φ_0 in (4) has two minima and the value of the potential at the two minima are given by (see (22) and (30))

$$\Phi_0^{(I)}(\text{min}) \simeq -\frac{A^2}{4C}-\frac{Aa}{2C}, \qquad \Phi_0^{(II)}(\text{min}) \simeq -\frac{A^2}{4C}. \qquad (31)$$

Which of the two would correspond to the true ground state depends on which of the two values in (31) is lower. Since the leading term in the two values is the same, we see that this question comes down to what is the value of the nonrelativistic parameter a. If $a < 0$, since we know that $A < 0,\ C > 0$, it follows from (31) that $\Phi_0^{(I)}(\text{min})$ would be the lower of the two and, therefore, would correspond to the true ground state. On the other hand, $\Phi_0^{(II)}(\text{min})$ would have a lower value and correspond to the true ground state if $a > 0$. As we have seen, the ground state described by $\Phi_0^{(I)}(\text{min})$ corresponds to an antiferromagnetic state ($\mathbf{m} = 0$) while the ground state represented by $\Phi_0^{(II)}(\text{min})$ describes a weak ferromagnetic state ($|\mathbf{m}| \sim O(|\frac{\beta}{B}|) \sim 10^{-2}$, see (14),(15) and (23)). Experimentally, these two states have been observed (below and above the Morin temperature) which leads us to conclude that $a(T < 250K) < 0$, while $a(250K < T < 950K) > 0$ where

$T = 250K$ denotes the Morin transition temperature. We recall here that the parameters in a statistical mechanical theory can be temperature dependent.

Double well potential:

Before we go on to include higher order corrections, let us quickly point out the double well structure of the potential which arises because of the spin reflection symmetry in (11) or equivalently in (12). For example, let us consider the second class of the minimum solutions given by (14),(15),(23) and (25). The thermodynamic potential (4), in this case, can be rewritten as

$$\begin{aligned}
\Phi_0 &= \frac{A}{2}(\ell_x^2+\ell_y^2+\ell_z^2) + \frac{B}{2}(m_x^2+m_y^2+m_z^2) + \frac{a}{2}\ell_z^2 + \frac{b}{2}m_z^2 \\
&\quad + \beta(\ell_x m_y - \ell_y m_x) + \frac{C}{4}(\ell_x^2+\ell_y^2+\ell_z^2)^2 \\
&= \frac{A}{2}\left(\ell_x^2+\ell_y^2+\frac{1}{C}(A-\frac{\beta^2}{B})+\ell_z^2-\frac{1}{C}(A-\frac{\beta^2}{B})\right) \\
&\quad + \frac{B}{2}\left((m_x-\frac{\beta}{B}\ell_y)^2+(m_y+\frac{\beta}{B}\ell_x)^2-\frac{2\beta}{B}(\ell_x m_y-\ell_y m_x)\right. \\
&\qquad\qquad \left. -\frac{\beta^2}{B^2}\left(\ell_x^2+\ell_y^2+\frac{1}{C}(A-\frac{\beta^2}{B})-\frac{1}{C}(A-\frac{\beta^2}{B})+m_z^2\right)\right) \\
&\quad + \frac{a}{2}\ell_z^2+\frac{b}{2}m_z^2+\frac{C}{4}\left(\ell_x^2+\ell_y^2+\frac{1}{C}(A-\frac{\beta^2}{B})+\ell_z^2-\frac{1}{C}(A-\frac{\beta^2}{B})\right)^2 . \qquad (32)
\end{aligned}$$

The terms can now be rearranged to write the thermodynamic potential in the form

$$\begin{aligned}\Phi_0 = \Phi_0^{(II)}(\min) - \frac{1}{2}(A - \frac{\beta^2}{B})\left(\ell_x^2 + \ell_y^2 + \frac{1}{C}(A - \frac{\beta^2}{B})\right) + \frac{(B+b)}{2}m_z^2 \\ + \frac{B}{2}\left((m_x - \frac{\beta}{B}\ell_y)^2 + (m_y + \frac{\beta}{B}\ell_x)^2\right) + \frac{a + \frac{\beta^2}{B}}{2}\ell_z^2 \\ + \frac{C}{2}\left(\ell_x^2 + \ell_y^2 + \frac{1}{C}(A - \frac{\beta^2}{B})\right)\ell_z^2 + \frac{C}{4}\ell_z^4 \\ + \frac{C}{4}\left(\ell_x^2 + \ell_y^2 + \frac{1}{C}(A - \frac{\beta^2}{B})\right)^2, \qquad (33)\end{aligned}$$

where $\Phi_0^{(II)}(\min)$ is given in (30). When $(\mathbf{m}, \mathbf{l})$ or $(-\mathbf{m}, -\mathbf{l})$ satisfy (14), (15), (23) and (25), all the terms in (33) vanish except for $\Phi_0^{(II)}(\min)$ which is the minimum thermodynamic potential for the second class of solutions. However, if $(\mathbf{m}, \mathbf{l})$ or $(-\mathbf{m}, -\mathbf{l})$ deviate from their minimum values, the additional contributions give a positive contribution leading to

$$\Phi_0 \geq \Phi_0^{(II)}(\min), \qquad (34)$$

which is the structure of a double well potential (double well because there are two ground states corresponding to the two spin reflected solutions).

Higher order corrections:

The basic problem that we find in the lowest order thermodynamic potential is that the rotational symmetry in the x-y plane does not allow us to determine the directions of the spins (or magnetization) uniquely. For this we need to go to higher order corrections [18, 98]. Since the magnitude of $\mathbf{l}$ can become large away from the transition points, a meanigful expansion is in terms of $\mathbf{m}$ and the unit vectors describing the antiferromagnetic vector, namely,

$$\hat{\mathbf{l}} = (\hat{\ell}_x, \hat{\ell}_y, \hat{\ell}_z) = (\sin\theta\cos\phi, \sin\theta\sin\phi, \cos\theta). \tag{35}$$

Here Φ is the angle l vector makes with the x axis and θ is the angle l vector makes with the z axis. With these variables, the thermodynamic potential including the next order interaction can be written as (note that $(\hat{\mathbf{l}})^2 = 1$ so that these terms do not arise in Φ)

$$\begin{aligned}\Phi = {} & \frac{a}{2}\hat{\ell}_z^2 + \frac{B}{2}\mathbf{m}^2 + q(\hat{\ell}_x m_y - \hat{\ell}_y m_x) + \frac{b}{2}m_z^2 + \frac{D}{2}(\hat{\mathbf{l}}\cdot\mathbf{m})^2 \\ & + \frac{d}{2i}[(\hat{\ell}_x + i\hat{\ell}_y)^3 - (\hat{\ell}_x - i\hat{\ell}_y)^3]\hat{\ell}_z + \frac{f}{2}[(\hat{\ell}_x + i\hat{\ell}_y)^3 + (\hat{\ell}_x - i\hat{\ell}_y)^3]m_z \\ & + \frac{e}{2}[(\hat{\ell}_x + i\hat{\ell}_y)^6 + (\hat{\ell}_x - i\hat{\ell}_y)^6] + \frac{g}{4}\hat{\ell}_z^4. \end{aligned} \tag{36}$$

Away from the points of transition, $a > d, e, f \,\text{and}\, g$ and, in particular, $\frac{d}{a} \sim \frac{f}{a} \sim \frac{g}{a} \sim O(\frac{v^2}{c^2}) \sim 10^{-2}$. On the other hand, e is even smaller, $\frac{e}{a} \sim O(\frac{v^4}{c^4}) \sim 10^{-4}$.

Symmetries:

The first thing to note about the thermodynamic potential with leading higher order terms in (36) is that, under a rotation in the x-y plane (see (10)),

$$\hat{\ell}_x \pm i\hat{\ell}_y \to \hat{\ell}'_x(\alpha) \pm i\hat{\ell}'_y(\alpha) = (\hat{\ell}_x \pm \hat{\ell}_y)e^{\mp i\alpha}, \qquad \hat{\ell}_z \to \hat{\ell}'_z(\alpha) = \hat{\ell}_z. \tag{37}$$

As a result, higher order terms involving combinations $(\hat{\ell}_x \pm \hat{\ell}_y)$ violate the rotational symmetry in the x-y plane which was there in the lowest order potential. (In other words, the terms with coefficients $d, e \,\text{and}\, f$ introduce anisotropy to the thermodynamic potential.) This suggests that, with the higher order terms, we may have unique ground state configurations (without rotational degeneracy). On the other hand, since the higher order interactions involve only even (power) combinations of $\hat{\mathbf{l}}, \mathbf{m}$, the spin reflection symmetry (12) is a good symmetry as in the lowest order. As a result, the ground state will continue to be doubly degenerate.

Ground states:

Minimizing Φ in (36) with respect to m_x, m_y, m_z (see (14)-(16)) and using the fact that the terms with coefficients b, D contribute negligibly to the equations, we obtain

$$\begin{aligned}
m_x: &\quad Bm_x - q\sin\theta\sin\phi = 0, \\
m_y: &\quad Bm_y + q\sin\theta\cos\phi = 0, \\
m_z: &\quad Bm_z + f\sin^3\theta\cos 3\phi = 0,
\end{aligned} \tag{38}$$

where we have used the spherical coordinate forms of the unit vector $\hat{\mathbf{l}}$ given in (35). Similarly, we can minimize the thermodynamic potential with respect to the spherical polar angles θ, ϕ and the set of equations has to be solved in a combined manner. However, to avoid technical details we will only summarize the characteristic features of the solutions using only (38). (We note that the determination of the angles essentially involve the minimization equations with respect to θ, ϕ.) There are three possible classes of solutions when we introduce the higher order corrections.

1. The first class of solutions corresponds to $\theta = 0$, implying that the antiferromagnetic vector ($\mathbf{l}$) lies along the z-axis ([111] axis). Furthermore, with $\theta = 0$, (38) leads to $m_x = m_y = m_z = 0$. Namely, it is an antiferromagnetic state with spins lying along the z-axis.

2. For the second class of solutions, we have the angles given by $\theta = \frac{\pi}{2} - \frac{d}{a}, \phi = \frac{\pi}{2}$.

With these, (38) leads to

$$
\begin{aligned}
m_x &= \frac{q}{B}\sin\left(\frac{\pi}{2}-\frac{d}{a}\right)\sin\frac{\pi}{2} = \frac{q}{B}\cos\frac{d}{a} \approx \frac{q}{B},\\
m_y &= -\frac{q}{B}\sin\left(\frac{\pi}{2}-\frac{d}{a}\right)\cos\frac{\pi}{2} = 0,\\
m_z &= -\frac{f}{B}\sin^3\left(\frac{\pi}{2}-\frac{d}{a}\right)\cos\frac{3\pi}{2} = 0,
\end{aligned} \tag{39}
$$

where, in the first equation, we have used the fact that $\frac{d}{a} \sim 10^{-2}$ is a small number. This solution says that the antiferromagnetic vector ($\mathbf{l}$) lies on a plane at a small angle $\frac{d}{a}$ ($\sim 10^{-2}$) to the basal plane (111) plane with a small magnetization ($|\frac{q}{B}| \sim 10^{-2}$) along a two fold axis (x-axis) perpendicular to the antiferromagnetic vector.

3. For the third class of solutions, the angles are determined to be $\theta = \frac{\pi}{2}, \phi = 0$ which leads to the magnetization vectors

$$
\begin{aligned}
m_x &= \frac{q}{B}\sin\frac{\pi}{2}\sin(0) = 0,\\
m_y &= -\frac{q}{B}\sin\frac{\pi}{2}\cos(0) = -\frac{q}{B},\\
m_z &= -\frac{f}{B}\sin^3\frac{\pi}{2}\cos(0) = -\frac{f}{B}.
\end{aligned} \tag{40}
$$

In this case, we see that the antiferromagnetic vector lies in the basal plane ((111) plane) along the two fold axis (x-axis). There is a small magnetization in the y-z plane (perpendicular to $\mathbf{l}$) with magnitude (recall that $|\frac{q}{B}| \sim 10^{-2}, |\frac{f}{B}| = |\frac{q}{B}||\frac{f}{q}| \sim 10^{-4}, a \sim q$)

$$\sqrt{\left(-\frac{q}{B}\right)^2 + \left(-\frac{f}{B}\right)^2} \approx \left|\frac{q}{B}\right| \sim 10^{-2}, \tag{41}$$

which is the same magnitude of magnetization as in the second class of solutions. The magnetization vector makes a small angle

$$\tan\delta = \frac{m_z}{m_y} = \frac{f}{q}, \quad \text{or,} \quad |\delta| \approx |\frac{f}{q}| \sim 10^{-2}, \tag{42}$$

to the basal plane. The solution, (40), shows that there can be a very small z-component ($|\frac{f}{B}| \sim 10^{-4}$) of the magnetization in the third class of ground state solutions.

This analysis of the ground states shows that, since there is no rotational invariance on the x-y plane, the solutions (for example, magnetization) are unique, unlike the analysis in the case of the lowest order potential. As in the lowest order, we can now calculate the value of the thermodynamic potential at the different minima which we only give here to avoid technical derivations:

$$\Phi^{(I)}(\min) = \frac{a}{2}, \quad \Phi^{(II)}(\min) = -\frac{q^2}{2B} - \frac{d^2}{4a} - e, \quad \Phi^{(III)}(\min) = -\frac{q^2}{2B} + e. \tag{43}$$

We recall that $|a| \sim |q|$ and $B > 0$, so that $\frac{q^2}{2B} = |q|\frac{|q|}{2B} \sim 10^{-2}|q| \ll |a|$ and $\frac{d^2}{4|a|} = |a|\frac{d^2}{4a^2} \sim 10^{-4}|a| \ll |a|$. As a result, for $a < 0$, we see that the true ground state will be given by the first class of solutions which describes an antiferromagnetic state and experimentally exists when $T < 250K$. For $a > 0$, $\Phi^{(I)}(\min)$ would have a higher value than the other two whose ordering will depend on the values of the parameters a, d, e. For $e > -\frac{d^2}{8a}$, we have

$$\Phi^{(II)}(\min) < \Phi^{(III)}(\min) < \Phi^{(I)}(\min), \tag{44}$$

so that the second class of solutions will correspond to the true ground state. As we have seen, this state is weak ferromagnetic and such a state is known experimentally to exist for $250K < T < 950K$. This state will have magnetization along the x-axis. On the other hand if $e < -\frac{d^2}{8a}$, the ordering of the minima takes the form

$$\Phi^{(III)}(\text{min}) < \Phi^{(II)}(\text{min}) < \Phi^{(I)}(\text{min}), \tag{45}$$

so that the third class of solutions will correspond to the true ground state. This is also a weak ferromagnetic state which experimentally is known to exist for $250K < T < 950K$. However, in this ground state the magnetization vector lies in the y-z plane with a very small ($|\frac{f}{B}| \sim 10^{-4}$, see (40)) component along the z-axis.

Appendix-2

Micron size $FeCO_3$ sample was synthesized by optimizing the procedure employed for the synthesis of $FeCO_3$ nano particles. In addition, two more samples that are rutile structure MnF_2 and the perovskite $BiFeO_3$ were synthesized by following the methods described in references [157] and [158] respectively.

Synthesis of $FeCO_3$ micro particles

In the typical synthesis of micron size $FeCO_3$ particle, $FeSO_4.7H_2O$, ascorbic acid and urea with the molar ratio of 1:3:9 were mixed in 5 ml of DDW. The solution was stirred properly for about 10-15 mins and then transferred into a Teflon lined stainless steel autoclave of 45 ml capacity. The reaction was carried out for 3 hours at a temperature of 160. The black colour precipitate deposited at the bottom of the Teflon container was collected through centrifugation, washed repeatedly with DDW and ethanol and then air dried before characterization.

Synthesis of MnF_2

For the synthesis of MnF_2, 0.98 g of manganese acetate and 7 ml of hydrofluoric acid (40% conc.) were dissolved in 30 ml of ethylene glycol. The whole mixture was stirred properly and transferred into a Teflon lined stainless steel autoclave of 45 ml capacity. The reaction was carried out at 180 °C for 12 hours. The white precipitate, deposited at the bottom of the Teflon cup, was collected through centrifugation, washed extensively with distilled water and ethanol and finally was air dried before characterization. The other samples of this family such as NiF_2 and CoF_2 can also be synthesized following this procedure.

Synthesis of $BiFeO_3$

Stoichiometric amounts of $Bi(NO_3)_3.5H_2O$ and $FeCl_3.6H_2O$ were first dissolved in 26 ml of deionized distilled water. To this solution, 10 ml of 7 M KOH solution was added. The solution was stirred properly using glass rod and sonication and then was transferred to a Teflon lined stainless steel autoclave of 45 ml capacity. The reaction was carried out for 4 hours at a temperature of 200 °C. The precipitate, deposited at the bottom of the Teflon cup, was collected through centrifugation, washed with ample amounts of distilled water and ethanol and was finally dried at 70 °C for 3-4 hours.

The XRD patterns recorded using Cu Kα radiation are shown in Figures. 1 (a) - (c) for $FeCO_3$, MnF_2 and $BiFeO_3$ respectively. The diffraction patterns show that the samples are pure and free from any impurity as well as secondary phases. The SEM images of the corresponding samples are given in Figures. 1 (d) - (f) respectively.

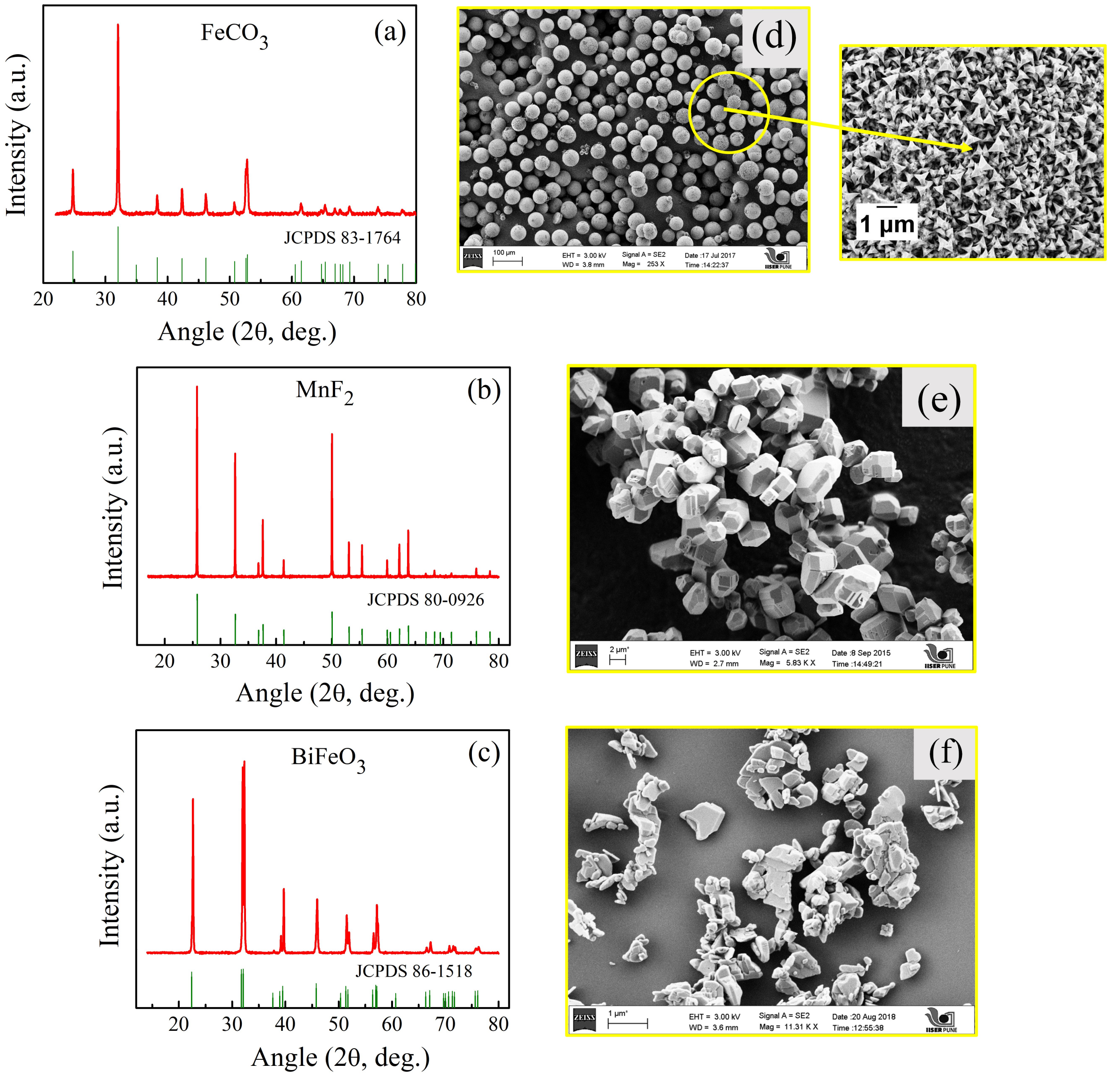

Figure 1 – Laboratory source based XRD pattern of (a) $FeCO_3$, (b) MnF_2, (c) $BiFeO_3$. The diffraction patterns are well matched with the JCPDS numbers. (d)-(f) are the SEM images showing particle morphology and size in $FeCO_3$, MnF_2 and $BiFeO_3$ respectively.

References

[1] C. Kittel, *Introduction to solid state physics*, John Wiley and sons, Inc., 2003.

[2] G. D. Mahan, *Condensed Matter in a Nutshell*, Princeton University Press, 2011.

[3] J. Stöhr and H. C. Siegmann, *Magnetism: From Fundamentals to Nanoscale Dynamics*, Springer, 2006.

[4] D. I. Khomskii, *Transition metal compounds*, United Kingdom: Cambridge University Press, 2014.

[5] R. Skomski, *Simple Models of Magnetism*, Oxford University Press, 2008.

[6] P. W. Anderson, *Phys. Rev.*, 1950, **79**, 350–356.

[7] K.-I. Gondaira and Y. Tanabe, *Journal of the Physical Society of Japan*, 1966, **21**, 1527–1548.

[8] J. Kanamori, *Journal of Physics and Chemistry of Solids*, 1959, **10**, 87 – 98.

[9] A. H. Morrish, *Canted Antiferromagnetism: Hematite*, World Scientific Publishing. Co. Pte. Ltd, 1963.

[10] K. Yosida, *Theory of magnetism*, Springer, 1996.

[11] M. A. Ruderman and C. Kittel, *Phys. Rev.*, 1954, **96**, 99–102.

[12] J. M. D. Coey, *Magnetism and magnetic materials*, Cambridge University Press, 2009.

[13] W. E. Evenson and S. H. Liu, *Phys. Rev.*, 1969, **178**, 783–794.

[14] T. Nagamiya, in *T. Nagamiya*, ed. F. Seitz, D. Turnbull and H. Ehrenreich, Academic Press, 1968, vol. 20 of Solid State Physics, pp. 305 – 411.

[15] F. Duan and J. Guojun, *Introduction to Condensed Matter Physics, Volume 1*, Academic Press, Inc., 1963.

[16] A. Ramirez, *Annual Review of Materials Science*, 1994, **24**, 453–480.

[17] H. Diep *et al.*, *Frustrated spin systems*, World Scientific, 2013.

[18] I. E. Dzyaloshinskii, *JETP*, 1957, **32**, 1259.

[19] T. Moriya, *Phys. Rev.*, 1960, **120**, 91–98.

[20] T. T. Smith, *Phys. Rev.*, 1916, **8**, 721–737.

[21] A. Borovik-Romanov and M. Orlova, *Soviet Physics JETP*, 1957, **4**, 531.

[22] G. Rollmann, A. Rohrbach, P. Entel and J. Hafner, *Physical Review B*, 2004, **69**, 165107.

[23] C. G. Shull, W. A. Strauser and E. O. Wollan, *Phys. Rev.*, 1951, **83**, 333–345.

[24] G. T. Rado and H. Suhl, *Magnetic Ions in Insulators Their Interactions Resonances and Optical Properties*, Academic Press, INC (London), 1963.

[25] J. SandonÃs, J. Baruchel, B. Tanner, G. Fillion, V. Kvardakov and K. Podurets, *Journal of Magnetism and Magnetic Materials*, 1992, **104-107**, 350 – 352.

[26] A. N. Bazhan and C. Bazan, *Soviet Physics JETP*, 1975, **42**, 898.

[27] A. B. Romanov, *Soviet Physics JETP*, 1960, **11**, 786.

[28] I. E. Dzyaloshinskii, *JETP*, 1957, **33**, 807.

[29] A. S. Borovik-Romanov, *Zh. Eksp. Teor. Fiz.*, 1960, **38**, 1088.

[30] V. Andratskii and A. S. Borovik-Romanov, *JETP*, 1966, **687**, 1036.

[31] T. G. Phillips, R. L. Townsend and R. L. White, *Phys. Rev. Lett.*, 1967, **18**, 646–647.

[32] T. G. Phillips, R. L. Townsend and R. L. White, *Phys. Rev.*, 1967, **162**, 382–388.

[33] S. A. J. Kimber and J. P. Attfield, *J. Mater. Chem.*, 2007, **17**, 4885–4888.

[34] Binek, Ch., Borisov, P., Chen, Xi, Hochstrat, A., Sahoo, S. and Kleemann, W., *Eur. Phys. J. B*, 2005, **45**, 197–201.

[35] L. D. Landau, J. Bell, M. Kearsley, L. Pitaevskii, E. Lifshitz and J. Sykes, *Electrodynamics of continuous media*, elsevier, 2013, vol. 8.

[36] A. S. Borovik-Romanov, *Ferroelectrics*, 1994, **162**, 153.

[37] S. K. Banerjee, *Earth and Planetary Science Letters*, 1970, **8**, 197–201.

[38] D. J. Dunlop, F. D. Stacey and D. E. Gillingham, *Earth and Planetary Science Letters*, 1974, **21**, 288–294.

[39] J. Liu, X. Cheng, F. Tong and X. Miao, *Journal of Applied Physics*, 2014, **116**, 043901.

[40] S. Mitra, O. Mondal, S. Banerjee and D. Chakravorty, *Journal of Applied Physics*, 2013, **113**, 024307.

[41] M. Mukadam, S. Yusuf, P. Sharma, S. Kulshreshtha and G. Dey, *Physical Review B*, 2005, **72**, 174408.

[42] U. Nowak and K. D. Usadel, *Phys. Rev. B*, 1991, **43**, 851–853.

[43] U. Nowak and K.-D. Usadel, *Phys. Rev. B*, 1989, **39**, 2516.

[44] C. Ro, G. S. Grest, C. Soukoulis and K. Levin, *Physical Review B*, 1985, **31**, 1682.

[45] V. Markovich, R. Puzniak, Y. Skourski, A. Wisniewski, D. Mogilyanski, G. Jung and G. Gorodetsky, *Journal of Physics: Condensed Matter*, 2012, **24**, 266001.

[46] M. J. Benitez, O. Petracic, H. Tüysüz, F. Schüth and H. Zabel, *Phys. Rev. B*, 2011, **83**, 134424.

[47] M. J. Benitez, O. Petracic, E. L. Salabas, F. Radu, H. Tüysüz, F. Schüth and H. Zabel, *Phys. Rev. Lett.*, 2008, **101**, 097206.

[48] J. Kushauer, C. Binek and W. Kleemann, *Journal of Applied Physics*, 1994, **75**, 5856–5858.

[49] J. Kushauer, W. Kleemann, J. Mattsson and P. Nordblad, *Phys. Rev. B*, 1994, **49**, 6346–6349.

[50] T. Fries, Y. Shapira, A. Paduan-Filho, C. Becerra and F. Palacio, *Journal of Physics: Condensed Matter*, 1993, **5**, 8083.

[51] S. Sahoo and C. Binek, *Philosophical Magazine Letters*, 2007, **87**, 259–268.

[52] A. Bajpai, R. Klingeler, N. Wizent, A. K. Nigam, S.-W. Cheong and B. BÃŒchner, *Journal of Physics: Condensed Matter*, 2010, **22**, 096005.

[53] A. Bajpai, Z. Aslam, S. Hampel, R. Klingeler and N. Grobert, *Carbon*, 2017, **114**, 291 – 300.

[54] N. T. K. Thanh and M. S. Maclean, N, *Chem. Rev.*, 2014, **114**, 7610–7630.

[55] G. Cao, *Nanostructures and Nanomaterials: Synthesis, Properties and Applications*, Imperial College Press, 2004.

[56] S. K. Kulkarni, *Nanotechnology: Principles and Practices*, Springer International Publishing, 2007.

[57] K. Byrappa and M. Yoshimura, *Handbook of Hydrothermal Technology*, Noyes Publications, 2001.

[58] Q. H. Ruren Xu, Wenqin Pang, *Modern Inorganic Synthetic Chemistry*, Elsevier, 2011.

[59] M. Shandilya, R. Rai and J. Singh, *Advances in Applied Ceramics*, 2016, **115**, 354–376.

[60] A. B. Djurisic, X. Y. Chen and Y. H. Leung., *Chem. Rev.*, 2012, **6**, 124 – 134.

[61] X. Liu, J. Zhang, S. Wu, D. Yang, P. Liu, H. Zhang, S. Wang, X. Yao, G. Zhu and H. Zhao, *RSC Adv.*, 2012, **2**, 6178–6184.

[62] L. Chen, X. Yang, J. Chen, J. Liu, H. Wu, H. Zhan, C. Liang and M. Wu, *Inorganic chemistry*, 2010, **49**, 8411–8420.

[63] M. Nassar and I. Ahmed, *Polyhedron*, 2011, **30**, 2431 – 2437.

[64] M. Kurmoo, *Molecular Crystals and Liquid Crystals*, 2002, **379**, 271–278.

[65] X. Liu, H. Wang, C. Su, P. Zhang and J. Bai, *Journal of Colloid and Interface Science*, 2010, **351**, 427 – 432.

[66] M. Lisunova, N. Holland, O. Shchepelina and V. V. Tsukruk, *Langmuir*, 2012, **28**, 13345–13353.

[67] B. D. Cullity and S. R. Stock, *Elements of X-ray Diffraction*, Prentice Hall, 2001.

[68] R. Young, *The Rietveld Method*, International Union of Crystallography. Oxford University Press, 1995.

[69] L. B. McCusker, R. B. V. Dreele, D. E. Cox, D. LouÃ■rd and P. Scardie, *J. Appl. Cryst.*, 1999, **32**, 36–50.

[70] B. H. Toby, *Powder Diffraction*, 2006, **21**, 67–70.

[71] G. E. Bacon, *Neutron diffraction*, Clarendon Press, 1975.

[72] L. Reimer, *Scanning Electron Microscopy: Physics of Image Formation and Microanalysis*, Springer-Verlag Berlin Heidelberg, 1998.

[73] J. Clarke and A. I. Braginski, *The SQUID Handbook*, Wiley-VCH verlag, 2004.

[74] J. C. Gallop and B. W. Petley, *Journal of Physics E: Scientific Instruments*, 1976, **9**, 417–429.

[75] K. C. Kao, *Dielectric Phenomena in Solids*, Elsevier Academic Press, 2004.

[76] J. R. Ferraro, K. Nakamoto and C. W. Brown, *Introductory Raman Spectroscopy*, Academic Press, 2003.

[77] A. Borovik-Romanov and V. Ozhogin, *Soviet Physics JETP*, 1961, **12**, year.

[78] N. Kreines and T. Shal'Nikova, *Soviet Physics JETP*, 1970, **31**, year.

[79] R. Plumier, M. Sougi, M. Lecomte and R. Saint-James, *Journal of Applied Physics*, 1985, **57**, 3261–3263.

[80] T. Lancaster, S. Blundell, F. Pratt and M. Kurmoo, *Physica B: Condensed Matter*, 2003, **326**, 522–526.

[81] R. Plumier, M. Sougi and R. Saint-James, *Phys. Rev. B*, 1983, **28**, 4016–4020.

[82] G. Beutier, S. Collins, O. Dimitrova, V. Dmitrienko, M. Katsnelson, Y. Kvashnin, A. Lichtenstein, V. Mazurenko, A. Nisbet, E. Ovchinnikova *et al.*, *Physical review letters*, 2017, **119**, 167201.

[83] V. Meshcheryakov, *Journal of Magnetism and Magnetic Materials*, 2006, **300**, e395–e398.

[84] V. Eremenko, N. Kharchenko, L. Beliy and O. Tutakina, *Journal of Magnetism and Magnetic Materials*, 1980, **15**, 791–792.

[85] D. Pincini, F. Fabrizi, G. Beutier, G. Nisbet, H. Elnaggar, V. Dmitrienko, M. Katsnelson, Y. Kvashnin, A. Lichtenstein, V. Mazurenko *et al.*, *Physical Review B*, 2018, **98**, 104424.

[86] R. Diehl, *Solid State Communications*, 1975, **17**, 743 – 745.

[87] E. Maslen, V. Streltsov, N. Streltsova and N. Ishizawa, *Acta Crystallographica Section B: Structural Science*, 1995, **51**, 929–939.

[88] H. Meijer, L. Pimmelaar, S. Brouwer and J. Van den Handel, *Physica*, 1970, **46**, 279–290.

[89] J. B. Lee, W. G. Hong, H. J. Kim, Z. Jagličić, S. Jazbec, M. Wencka, A. Jelen and J. Dolinšek, *Physical Review B*, 2012, **86**, 224407.

[90] A. McDannald, L. Kuna, M. S. Seehra and M. Jain, *Phys. Rev. B*, 2015, **91**, 224415.

[91] S. Mørup and C. Frandsen, *Phys. Rev. Lett.*, 2004, **92**, 217201.

[92] L. Néel, *Rev. Mod. Phys.*, 1953, **25**, 58–63.

[93] K. Binder and A. P. Young, *Rev. Mod. Phys.*, 1986, **58**, 801–976.

[94] J. Mattsson, C. Djurberg and P. Nordblad, *Phys. Rev. B*, 2000, **61**, 11274–11277.

[95] M. Alba, M. Ocio and J. Hammann, *EPL (Europhysics Letters)*, 1986, **2**, 45.

[96] R. V. Chamberlin, *Journal of Applied Physics*, 1985, **57**, 3377–3381.

[97] S. N. Martynov, *JETP Letters*, 2018, **108**, 196–200.

[98] P. Radhakrishna, *Le Journal de Physique Colloques*, 1982, **43**, C7–221.

[99] A. Borovik-Romanov, A. Bazhan and N. Kreines, *Soviet Journal of Experimental and Theoretical Physics*, 1973, **37**, 695.

[100] V. Loktev, *Physics Letters A*, 1981, **81**, 187–188.

[101] N. Golosova, D. Kozlenko, L. Dubrovinsky, V. Cerantola, M. Bykov, E. Bykova, S. Kichanov, E. Lukin, B. Savenko, A. Ponomareva *et al.*, *Physical Review B*, 2017, **96**, 134405.

[102] I. Jacobs, *Journal of Applied Physics*, 1963, **34**, 1106–1107.

[103] N. Pattanayak, A. Bhattacharyya, A. K. Nigam, S.-W. Cheong and A. Bajpai, *Phys. Rev. B*, 2017, **96**, 104422.

[104] F. Morin, *Physical Review*, 1950, **78**, 819.

[105] J. Sandonis, J. Baruchel, B. Tanner, G. Fillion, V. Kvardakov and K. Podurets, *Journal of Magnetism and Magnetic Materials*, 1992, **104**, 350 – 352.

[106] Ö. Özdemir and D. J. Dunlop, *Journal of Geophysical Research: Solid Earth*, 2014, **119**, 2582–2594.

[107] R. D. Zysler, D. Fiorani, A. M. Testa, L. Suber, E. Agostinelli and M. Godinho, *Phys. Rev. B*, 2003, **68**, 212408.

[108] S. Mitra, S. Das, S. Basu, P. Sahu and K. Mandal, *Journal of Magnetism and Magnetic Materials*, 2009, **321**, 2925 – 2931.

[109] G. Ouyang, W. Zhu, C. Sun, Z. Zhu and S. Liao, *Physical Chemistry Chemical Physics*, 2010, **12**, 1543–1549.

[110] O. Lemine, M. Sajieddine, M. Bououdina, R. Msalam, S. Mufti and A. Alyamani, *Journal of alloys and compounds*, 2010, **502**, 279–282.

[111] D. Schroeer and R. Nininger Jr, *Physical Review Letters*, 1967, **19**, 632.

[112] M. Jagodič, Z. Jagličić, A. Jelen, J. B. Lee, Y.-M. Kim, H. J. Kim and J. Dolinšek, *Journal of Physics: Condensed Matter*, 2009, **21**, 215302.

[113] R. Bhowmik and R. Ranganathan, *Solid State Communications*, 2007, **141**, 365 – 368.

[114] D. Sands, *Introduction to Crystallography*, Dover Publications, New York, 1993.

[115] A. H. Hill, F. Jiao, P. G. Bruce, A. Harrison, W. Kockelmann and C. Ritter, *Chemistry of Materials*, 2008, **20**, 4891–4899.

[116] J. Ma and K. Chen, *EPL (Europhysics Letters)*, 2014, **108**, 37005.

[117] J. Wang, V. Aguilar, L. Li, F.-g. Li, W.-z. Wang and G.-m. Zhao, *Nano Research*, 2015, **8**, 1906–1916.

[118] A. S. Borovik-Romanov and M. Orlova, *Soviet Physics JETP-USSR*, 1957, **4**, 531–534.

[119] L. M. Sandratskii and J. Kubler, *Europhysics Letters (EPL)*, 1996, **33**, 447–452.

[120] S. Di Matteo, Y. Joly, A. Bombardi, L. Paolasini, F. de Bergevin and C. Natoli, *Physical review letters*, 2003, **91**, 257402.

[121] P. Flanders, *Journal of Applied Physics*, 1972, **43**, 2430–2435.

[122] N. Ortega, A. Kumar, J. Scott and R. S. Katiyar, *Journal of Physics: Condensed Matter*, 2015, **27**, 504002.

[123] R. Ramesh and N. A. Spaldin, *Nature materials*, 2007, **6**, 21.

[124] N. A. Hill, *The Journal of Physical Chemistry B*, 2000, **104**, 6694–6709.

[125] I. E. Dzyaloshinskii, *Soviet Physics JETP*, 1960, **10**, 628–629.

[126] D. Astrov, *Sov. Phys. JETP*, 1961, **13**, 729–733.

[127] T. Aoyama, K. Yamauchi, A. Iyama, S. Picozzi, K. Shimizu and T. Kimura, *Nature communications*, 2014, **5**, 4927.

[128] T. Kimura, T. Goto, H. Shintani, K. Ishizaka, T.-h. Arima and Y. Tokura, *nature*, 2003, **426**, 55.

[129] N. Hur, S. Park, P. Sharma, S. Guha and S. Cheong, *Physical review letters*, 2004, **93**, 107207.

[130] H. Katsura, A. V. Balatsky and N. Nagaosa, *Physical review letters*, 2007, **98**, 027203.

[131] G. Lawes, T. Kimura, C. Varma, M. Subramanian, N. Rogado, R. Cava and A. Ramirez, *Progress in Solid State Chemistry*, 2009, **37**, 40–54.

[132] R. Tackett, G. Lawes, B. C. Melot, M. Grossman, E. S. Toberer and R. Seshadri, *Physical Review B*, 2007, **76**, 024409.

[133] T. Kimura, S. Kawamoto, I. Yamada, M. Azuma, M. Takano and Y. Tokura, *Physical Review B*, 2003, **67**, 180401.

[134] R. E. Newnham, *Properties of Materials: Anisotropy, Symmetry, Structure*, New York: Oxford University Press, 2005.

[135] Y. S. Shin and S.-O. Park, *Microwave and Optical Technology Letters*, 2010, **52**, 2364–2367.

[136] S. Tiwari and S. Vitta, *Scientific reports*, 2018, **8**, year.

[137] H. Singh, H. Ghosh, T. Chandrasekhar Rao, G. Sharma, J. Saha and S. Patnaik, *Journal of Applied Physics*, 2016, **119**, 044104.

[138] A. G. Lone and R. Bhowmik, *AIP Advances*, 2015, **5**, 047117.

[139] C. Kadlec, V. Goian, K. Rushchanskii, P. Kužel, M. Ležaić, K. Kohn, R. Pisarev and S. Kamba, *Physical Review B*, 2011, **84**, 174120.

[140] S. Kamba, V. Goian, V. Skoromets, J. Hejtmánek, V. Bovtun, M. Kempa, F. Borodavka, P. Vaněk, A. Belik, J. Lee *et al.*, *Physical Review B*, 2014, **89**, 064308.

[141] J. Vermette, S. Jandl and M. Gospodinov, *Journal of Physics Condensed Matter*, 2008, **20**, year.

[142] M. Balkanski, R. Wallis and E. Haro, *Physical Review B*, 1983, **28**, 1928.

[143] P. Thongbai, S. Tangwancharoen, T. Yamwong and S. Maensiri, *Journal of Physics: Condensed Matter*, 2008, **20**, 395227.

[144] L. Zhang and Z.-J. Tang, *Physical Review B*, 2004, **70**, 174306.

[145] T. J. Smart and Y. Ping, *Journal of Physics: Condensed Matter*, 2017, **29**, 394006.

[146] M. Sharma, S. Murugavel, D. K. Shukla and F. M. De Groot, *The Journal of Physical Chemistry C*, 2018, **122**, 9292–9301.

[147] P. Lunkenheimer, V. Bobnar, A. V. Pronin, A. Ritus, A. Volkov and A. Loidl, *Physical Review B*, 2002, **66**, 052105.

[148] G. Catalan, *Applied Physics Letters*, 2006, **88**, 102902.

[149] J. C. Papaioannou, G. S. Patermarakis and H. S. Karayianni, *Journal of Physics and Chemistry of Solids*, 2005, **66**, 839–844.

[150] S.-H. Shim and T. S. Duffy, *American Mineralogist*, 2002, **87**, 318–326.

[151] I. Beattie and T. Gilson, *Journal of the Chemical Society A: Inorganic, Physical, Theoretical*, 1970, 980–986.

[152] I. Chernyshova, M. Hochella Jr and A. Madden, *Physical Chemistry Chemical Physics*, 2007, **9**, 1736–1750.

[153] R. D. Rodriguez, E. Sheremet, T. Deckert-Gaudig, C. Chaneac, M. Hietschold, V. Deckert and D. R. Zahn, *Nanoscale*, 2015, **7**, 9545–9551.

[154] M. Massey, U. Baier, R. Merlin and W. Weber, *Physical Review B*, 1990, **41**, 7822.

[155] E. Granado, A. García, J. A. Sanjurjo, C. Rettori, I. Torriani, F. Prado, R. D. Sánchez, A. Caneiro and S. B. Oseroff, *Phys. Rev. B*, 1999, **60**, 11879–11882.

[156] N. Pattanayak, A. Bhattacharyya, S. Chakravarty and A. Bajpai, *Journal of Physics: Condensed Matter*, 2019, **31**, 365802.

[157] X. Li, J. Lu, G. Peng, L. Jin and S. Wei, *Journal of Physics and Chemistry of Solids*, 2009, **70**, 609–615.

[158] J.-P. Zhou, R.-L. Yang, R.-J. Xiao, X.-M. Chen and C.-Y. Deng, *Materials Research Bulletin*, 2012, **47**, 3630–3636.